Atomistic Simulations of Deformation and Fracture Mechanisms in Nanotwinned Nanowires and Biomaterials

by

Sheng Yin

B. S. Solid Mechanics, University of Science and Technology of China, 2011

A dissertation submitted in partial fulfillment of the

requirements for the Degree of Doctor of Philosophy

in the School of Engineering at Brown University

Providence, Rhode Island

May 2017

This dissertation by Sheng Yin is accepted in its present form by

the School of Engineering as satisfying the dissertation requirement

for the degree of Doctor of Philosophy.

Date_____ _____

Prof. Huajian Gao, Advisor

Recommended to the Graduate Council

Date_____ _____

Prof. Kyung-Suk Kim, Reader

Date_____ _____

Prof. Sharvan Kumar, Reader

Approved by the Graduate Council

Date_____ _____

Prof. Andrew G. Campbell

Dean of the Graduate School

Vita

Sheng Yin was born on Feb 27, 1989 in Yancheng, Jiangsu Province, China. He attended The University of Science and Technology of China in 2007, and received the B.Sci. in Solid Mechanics in 2011. Upon graduation, he entered the Solid Mechanics program at Brown University. His research focused on modeling and simulations of mechanical properties of nanotwinned metal, ceramics and nanowires.

Acknowledgments

First of all, I would like to thank my advisor, Prof. Huajian Gao, for his mentoring and guidance during the past years. His passion and vision in research, his patience and encouragement while mentoring me have led me from an undergraduate student to a researcher and I'll continue to benefit from it in the future both in my career and my life. It is really a great honor for me to have been a member of Prof. Gao's group.

I would also like to thank my dissertation committee members, Prof. Kyung-Suk Kim and Prof. Sharvan Kumar for taking the time to read my thesis and for providing me with valuable suggestions. Thanks also to the entire Solid Mechanics faculty for the excellent education and research collaborations.

During my research, I had significant help and many suggestions from group members, collaborators and friends. I'm really grateful to Prof. Xiaoyan Li for his help and great guidance on my research. All my research works were motivated and collaborated with experimentalists. I greatly appreciate Prof. Yong Zhu, Dr. Guangminig Chen and Prof. Sang Ho Oh for invaluable discussions and enjoyable collaborations. Special thanks to Teng, Xin, Hongyan, Ill, Wengpeng, Haofei and all the group members for all the inspiration discussions.

Finally, I would like to thanks my parents and my wife for their support and love. Without their support and understanding, I would have never completed this thesis.

To my beloved family and my dear wife

Contents

List of Tables

List of Fig.s

Chapter 1 Introduction

1.1. Nanotwinned materials

A coherent twin boundary is a special type of grain boundary with low interface energy. By introducing nanoscale coherent twin boundaries (CTBs) into polycrystalline Cu, high strength and ductility can be simultaneously achieved as compared to conventional coarse-grained polycrystalline Cu along with high electrical conductivity (1-3) (Fig. 1.1a-c). Many atomistic models (4-9) have attempted to explain the enhancement in ductility without detriment to strength that is observed in nanotwinned metals with CTBs (Fig. 1.1d-e). Interactions between dislocations and CTBs have been intensively studied (10-14). CTBs can effectively impede dislocation motion but still allow a high density of mobile dislocations to operate in a highly organized lamella structure (1, 2, 15-18).

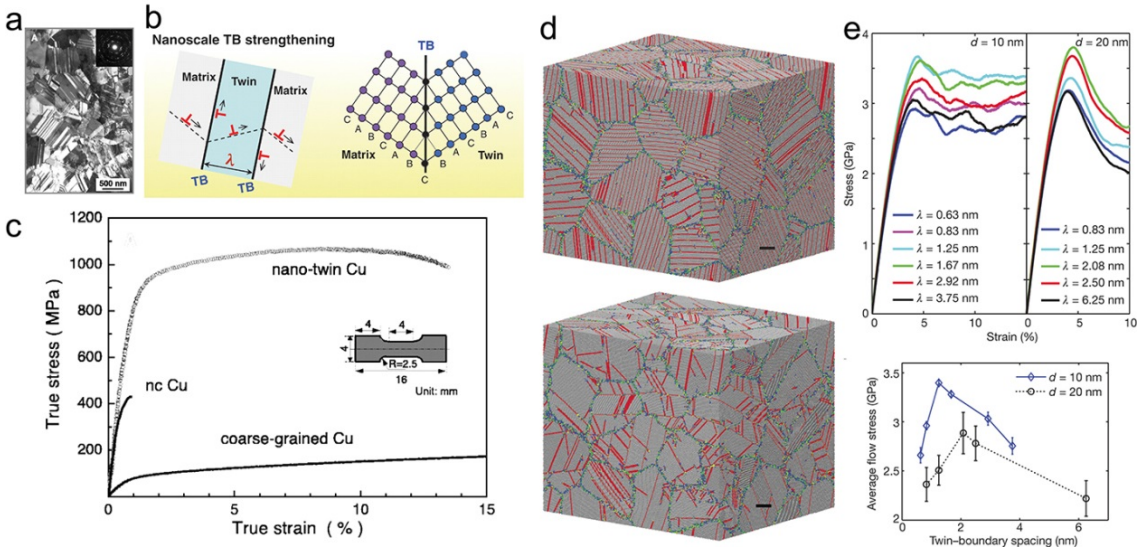

Figure 1.1 | Nanotwinned metals a, Microstructures of NT metals(2). **b,** Nanoscale TB strengthening mechanism(3). **c,** A typical tensile stress-strain curve for as-deposited NT Cu (with average grain size *d* of 500 nm and TB spacing λ of 15nm) in comparison with that for a CG polycrystalline Cu (*d*>100 μm) and NC Cu (*d*~30 nm)(2). **d,** Molecular dynamics simulation of nano-twinned Cu. **e,** Stress–strain relations and flow stress from molecular dynamics simulations of nano-twinned Cu(4).

Besides nanotwinned metals, nanoscale twins have also been incorporated into polycrystalline ceramics such as cubic boron-nitride (cBN), diamond, boron-carbide (B_4C) and boron-suboxide (B_6O) during the last few years (19-27). These synthetic nanotwinned ceramics exhibit ultra-high hardness, enhanced fracture toughness, and improved thermal stability (19-27). In addition in nature, some aragonitic mollusk shells are found that contain a high density of nanoscale growth twins in their lowest-level mineral platelets (28). The role of nanotwins in biomaterial will be investigated in Chapter 2.

One-dimensional (1D) nanostructures are widely regarded as among the most important building blocks for a broad range of applications including nanoelectronics, optoelectronics, energy harvesting and storage, ultrasensitive sensing, and nanoelectromechanical devices (29, 30). Nanowires commonly exhibit ultrahigh mechanical strength, which make them also ideal candidates for studying fundamental deformation mechanisms at the nanoscale (31-33). In recent years, nanowires or nanopillars with twin boundary or other complex twinned structures inside them have drawn much attention. CTBs in nanowires may play a different role from that in the bulk system. A brittle-to-ductile transition in nanopillars with orthogonally oriented twin boundaries was observed as the twin boundary spacing decreased below a critical value

(34) (Fig. 1.2a). Near-ideal theoretical strength was observed in gold nanowires containing angstrom scale twins (35) (Fig. 1.2b). Distinguishing size effects were found in Ag nanowires with penta-twinned structure (36) (Fig. 1.2c). These recent studies call for more systematic investigations of deformation mechanisms in nanowires with internal structures. In Chapter 3-5, I will study different deformation mechanisms in penta-twinned NWs, bi-twinned NWs and single crystalline NWs.

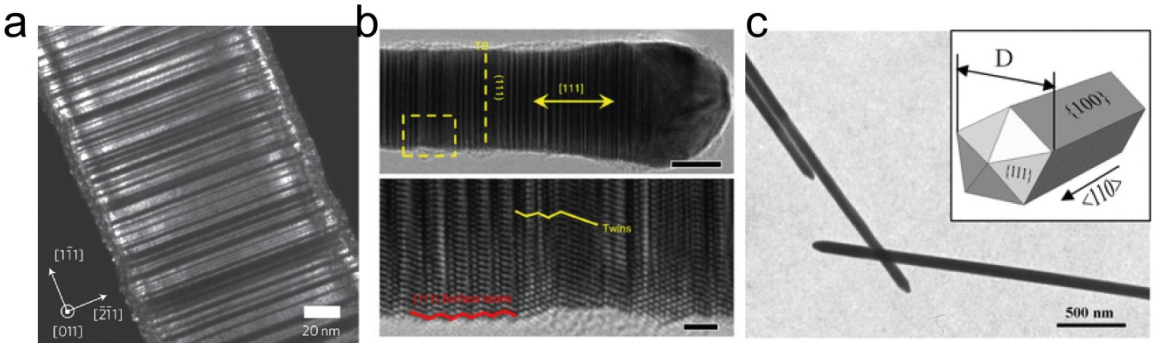

Figure 1.2 | Nanowires with internal structures. a, Copper pillar with orthogonal twin boundary inside (34). **b,** Morphology of as-synthesized Au NW (35). Scale bar, 10 nm. **c,** Low-magnification TEM image of Ag NWs with a diameter ~80 nm (36).

1.2. Methodology of molecular dynamics

Most of the simulations in this thesis will be carried out with molecular dynamics (MD). Therefore a brief introduction of MD simulation, interatomic potential and common ensembles used in the simulations will be introduced.

Molecular dynamics is a computational method for studying the physical movements of atoms and molecules, a technique that has been widely used to study the fundamental mechanisms of mechanical deformation in nanostructures. To simplify the

system from a fully quantum description to a classical molecular dynamics description, two main approximations are applied. The first one is the Born–Oppenheimer approximation, which states that the dynamics of electrons are so fast that they can be considered to react instantaneously to the motion of their nuclei. As a result, electrons and nuclei can be treated separately. The second approximation is that the nuclei are much heavier than electrons, and follow classical Newtonian dynamics. Based on the above approximations, the trajectories of atoms and molecules are determined by numerically solving Newton's equations of motion for a system,

$$m_i \ddot{\mathbf{r}}_i = \mathbf{f}_i, \tag{1.1}$$

where m_i is the mass of the ith atom, $\mathbf{r}_i$ is the Cartsian coordinates, and $\mathbf{f}_i$ is the interaction force applied on the ith atom by other atoms, and "•"denotes the time derivative.

The force between the particles is determined by

$$\mathbf{f}_i = -\frac{\partial U}{\partial \mathbf{r}_i}, \tag{1.2}$$

where U is the potential energy. The empirical potentials usually contain free parameters to fit the MD measurements with quantum simulations or experimental properties such as elastic constant, stacking fault energy and equilibrium lattice constant. The time step in simulations should match the kinetics of the natural process, such as vibration frequency of atoms. Thus, the typical time step of classical molecular dynamic simulation is around 1 femtosecond and the total simulation time usually spans from nanoseconds (10^{-9} s) to microseconds (10^{-6} s).

Interatomic potential plays a key role in classical MD simulations, since its accuracy directly determines the physical properties of the structures. For the FCC metallic system

studied in this thesis, embedded-atom-method (EAM) potential is an accurate and widely used many-body potential. A well fitted EAM potential can accurately reproduces many basic properties of the FCC metal, such as elastic constants, vacancy formation and migration energies, stacking fault energy, unstable stacking fault energy, twining energy and specific surface energy. This offers us a reliable way to study new deformation mechanism(s) by MD simulations.

Three different ensembles are commonly used in classical molecular dynamics: (1) microcanonical ensemble (NVE), (2) canonical ensemble (NVT), and (3) isothermal-isobaric ensemble (NPT).

If the total energy E, total number of atoms N and the volume V of the system are kept constant, then it is microcanonical (NVE) ensemble for MD simulation. In canonical (NVT) ensemble, the atom number N, the volume V and the temperature T of the system are conserved. The system energy is exchanged within a thermostat bath. Popular techniques to control temperature in NVT ensemble include velocity rescaling, Berendsen thermostat (37), Nose-Hoover thermostat (38), and Langevin dynamics (39). Isothermal-isobaric (NPT) ensemble represents a system with conserved atom number N, volume V and pressure P. The pressure is controlled by a barostat bath, a similar concept with the thermostat bath. The widely used barostat baths are Berendsen barostat (37), Andersen barostat (40) and Parrinello-Rahman barostat (41).

Large-scale Atomic/Molecular Massively Parallel Simulator (LAMMPS) (42) is a molecular dynamics program from Sandia National Laboratories. All the MD simulations in this thesis were performed using this package.

1.3. Outline of the thesis

In this thesis, I will investigate the toughening mechanism in nanotwinned biomaterials and deformation mechanisms in nanowires with different twin structures using atomistic simulations and continuum models. This thesis consists of six chapters and is organized as follows.

Chapter 1 is an overview introduction about the nanotwinned metals, ceramics and biomaterials and deformation mechanisms in nanowires with internal structures. The methodology of molecular dynamics simulation is introduced. The research motivation and goal are also presented.

In Chapter 2, I first introduce *in-situ* nanoindentation-based fracture experiments on twinned conch shell and single crystalline aragonite. Subsequently, CTOD FEM modeling was used to quantify the fracture toughness. MD simulations of crack propagation in twinned aragonite were performed. Observations from simulations and HRTEM characterization from experiments were linked. Finally, a self-similar hierarchical model was constructed to show the importance of toughness in the lowest-level of hierarchical structure. In this chapter, I focus on the toughening mechanisms induced by nanotwinned structures.

In Chapter 3, I first introduce *in-situ* stress relaxation test and the fully recoverable unloading deformation. Subsequently, MD simulations were performed to reveal the detail mechanism in stress relaxation under an applied strain and complete plastic strain recovery upon unloading. In this chapter, I focus on the detailed explanation of the mechanism in this recoverable plastic deformation and the unique role of the penta-twinned structure.

In Chapter 4, results of *in-situ* tensile tests of bi-twinned Ag NWs and single crystalline Ag NW are first introduced. Then MD simulations are applied to study the detailed deformation mechanisms in bi-twinned NWs and single crystalline NWs. Criterion for deformation modes transition is presented. In this chapter, I focus on the atomistic insights of the novel detwinning mechanism in the bi-twinned Ag NWs and the critical condition for the deformation mechanisms transition.

In Chapter 5, I first introduce results of *in-situ* tensile tests of penta-twinned Ag NWs with different hydrogen concentration. *In-situ* stress relaxation tests that are similar to Chapter 3 were also conducted in the presence of hydrogen. Hydrogen was thought to suppress surface dislocation nucleation in NWs and MD simulations were performed to complement the experiments and verify our hypothesis. In this chapter, I focus on the hydrogen effect on the surface dislocation nucleation in the nanostructures.

Chapter 6 concludes the entire thesis with major scientific findings and future directions.

Chapter 2 Nanotwin-governed toughening mechanism in hierarchically structured biological materials

The work described below is in collaboration with the experimental group of Prof. Sang Ho Oh, who performed all the *in-situ* experiments (28).

2.1. Introduction

Over the past decade, nanotwinned metals have attracted considerable attention due to their exceptional mechanical properties, such as ultra-high strength, good tensile ductility, high fracture toughness and remarkable fatigue resistance (1, 2, 4, 10). Besides metals, in biological materials, some aragonitic mollusk shells, such as *Strombus gigas* conch shell, are found to contain a high density of {110} growth twins in its third order aragonite lamellae, the basic building block of the material. Although the existence of nanotwinned aragonite has been known for decades (43, 44), its roles and functions in mechanical behaviors and properties of biological materials have received little attention. As an important class of natural biocomposite materials, mollusk shells possess remarkable mechanical strength and toughness as a consequence of their hierarchical structuring of soft organic and hard mineral constituents through biomineralization (45-51). And there exist worldwide interests in biomimetic materials and numerous studies in recent years aimed to investigate the relationship between mechanical properties (e.g.,

moduli, strength and toughness) and the elegant nano- and hierarchical structures of biological materials (45-52). Various toughening mechanisms in biological materials have been proposed, including microcracking and crack bridging (47, 53), flaw tolerance of nanostructure (46), viscoelastic deformation of organic layers (51, 54), and frictional sliding of mineral platelets (45).

In this chapter, I investigate the contribution of the inherent nanoscale twins in the conch shell to its fracture toughness at the basic building block level. To reveal the roles of the nanoscale growth twins, large-scale atomistic simulations and finite element modeling (FEM) were performed to explore the underlying interactions between the nanotwinned microstructure and a propagating crack tip. When the computational results are combined with *in situ* fracture experiments and HRTEM characterization, the fracture toughness can be quantitatively assessed and toughening mechanism can be revealed.

2.2. Experimental studies

2.2.1. Microstructural characterization

As illustrated in Fig. 2.1a, the basic building block of *Strombus gigas* is its third-order lamellae made of nanotwinned aragonite platelets 100~400 nm long, ~75 nm thick, and ~200 nm wide. Parallel stacking of the third-order lamellae forms a second-order lamella with width of 5-60 μm and thickness of 5-30 μm, and many second-order lamellae aggregate into a first-order lamella which is several micrometers wide and 5-60 μm thick. Fig. 2.1b shows two TEM images of third-order lamellae seen from their large-faces and end-faces, which are surrounded by a proteinaceous matrix and tightly interlocked.

Figure 2.1c shows two TEM dark-field images of a third-order lamella taken with the $(0\bar{1}1)_M$ and $(0\bar{1}1)_T$ reflections which are related by twinning on the $(1\bar{1}0)$ plane, and its selected area electron diffraction pattern (SAED) along the [111] zone axis. Quantitative analysis of HRTEM images confirms that the twin thickness varies from 2 nm to 20 nm, with a mean value of about 8 nm. A high resolution TEM (HRTEM) image in Fig. 2.1.d indicates that the $(1\bar{1}0)_{TB}$ twin boundaries (TBs) are coherent and free of defects. Figure 2.1e illustrates the orthorhombic unit cell of aragonite and corresponding atomic configuration of a TB. The microstructural and crystallographic characterizations summarized in Fig. 2.1 reveal that the *Strombus gigas* conch shell is constructed with nanotwinned aragonite platelets as the basic building block and as such can be regarded as a nanotwinned material synthesized by nature.

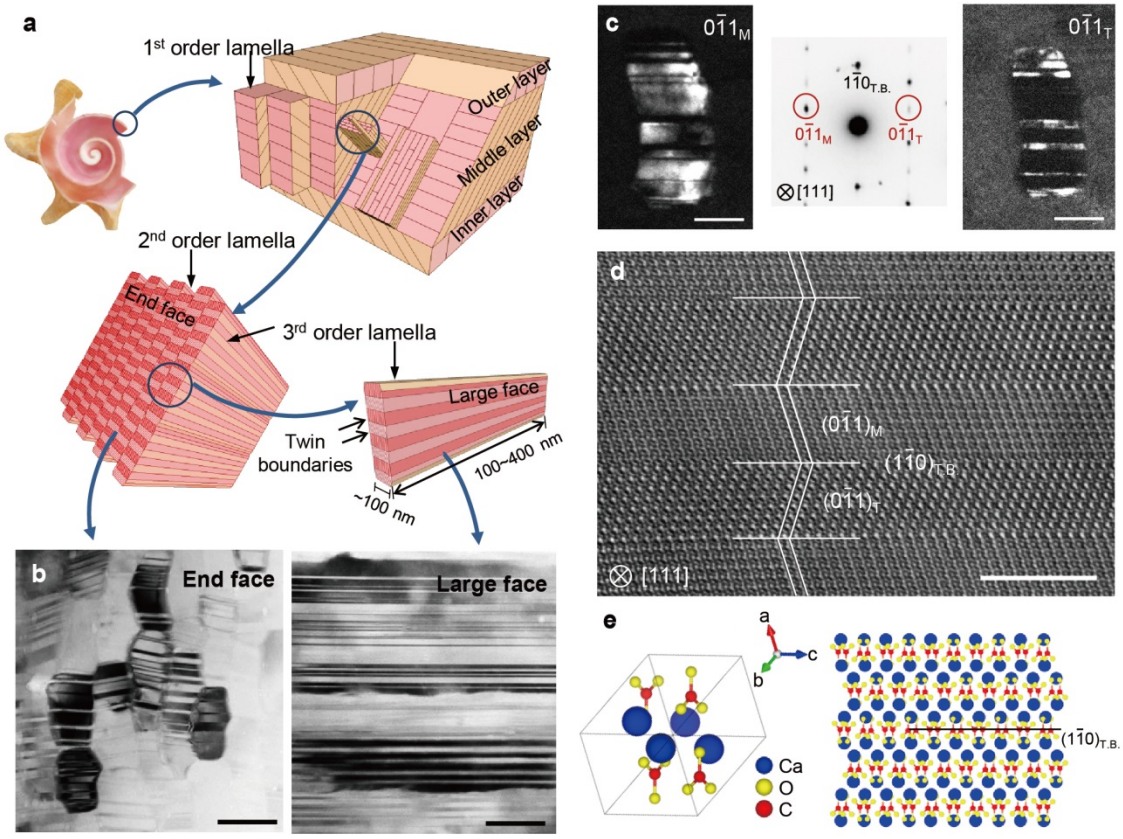

Figure 2.1 | Multi-level hierarchy and nanotwinned microstructure of *Strombus gigas* conch shell. a, A schematic illustration of multi-level hierarchy. **b,** TEM images showing the high density of nanotwins in the third-order lamellae. The nanotwins are seen from the end-face of third-order lamellae (left-hand side) and the large-face (right-hand side). Scale bar, 100 nm. **c,** Dark-field TEM images of a third-order lamella taken with the $(0\bar{1}1)_M$ matrix (left-hand side) and $(0\bar{1}1)_T$ twin (right-hand side) reflection, and electron diffraction pattern along [111] zone axis (middle). TBs are parallel to the $(1\bar{1}0)$ plane. Scale bar, 50 nm. **d,** HRTEM image of nanoscale twins in a third-order lamella aligned into the [111] zone axis. Scale bar, 5 nm. **e,** Orthorhombic unit cell of aragonite (left-hand side), and an atomic configuration of nanotwinned aragonite with $(1\bar{1}0)_{TB}$ TB (right-hand side). (Courtesy of Prof. Sang Ho Oh)

2.2.2. *In-situ* TEM fracture testing

In-situ real-time TEM fracture experiments based on a nanoindentation were used to investigate crack propagation in the nanotwinned aragonite (extracted from the conch shell) and its single-crystalline (twin-free) counterpart, and to quantitatively determine the fracture toughness by measuring crack tip opening displacement (CTOD).

In the current experiment, CTOD can be directly measured in TEM, which enables us applying standard CTOD approaches in the mechanical testing without calibration functions. To enable measurement of CTOD at nanoscale, a unique TEM specimen was designed which can be used in a nanoindentation TEM holder. Fig. 2.2 shows sample design and how the specimens used for *in situ* TEM CTOD measurement were prepared using focused ion beam (FIB, Helios Nano-Lab, FEI) machining techniques.

The CTOD was measured and traced directly from the *in situ* TEM movies. Based on the definition of δ_5 type CTOD (55), the CTOD in this study is defined as the opening displacement at a site which is about 100 nm away from the initial notch tip. This convention was adopted to prevent vagueness in image contrast at the notch tip and vacuum.

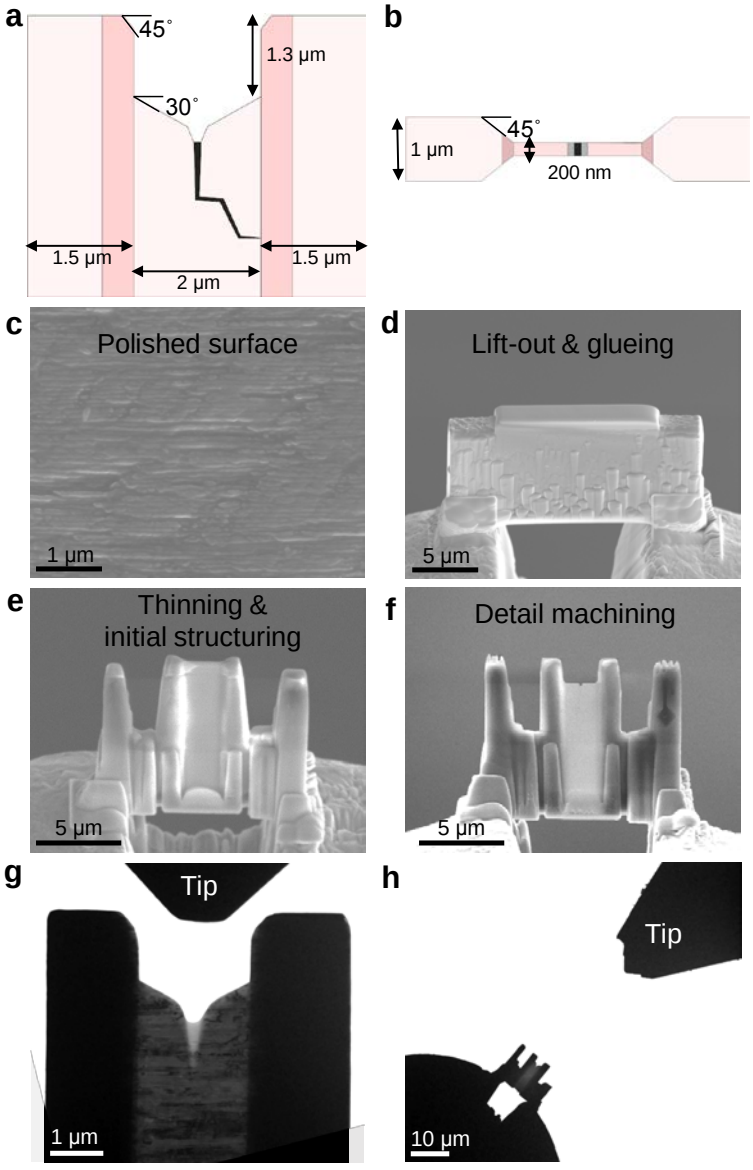

Figure 2.2 | Design and fabrication of *in situ* TEM Specimen for nanoscale CTOD measurement. Schematic illustrations of TEM specimen design for CTOD measurement in (**a**) side view and (**b**) top view. **c**, SEM micrograph of a mechanically polished surface of conch shell. **d**, Fixing of the lift-out sample on a Cu support grid. **e**, Initial structuring. **f**, Detailed machining. **g**, Experimental setup for CTOD measurement in TEM with a flat-ended nanoindentation tip. **h**, TEM image showing the alignment between a diamond tip and the specimen. (Courtesy of Prof. Sang Ho Oh)

Figure 2.3a-b shows the TEM specimen of nanotwinned and single-crystalline aragonites. Figure 2.3c and 2.3d present a sequence of TEM images of crack propagation in the nanotwinned and single-crystalline aragonites, respectively. For the single-crystalline aragonite, it is observed from Fig. 2.3d that the main crack propagates rapidly along a cleavage plane, and a few deformation twins form near the crack tip or some other stress-concentration sites. However, for the nanotwinned aragonite, the main crack propagates nearly perpendicular to the TBs and is then highly deflected by the TBs, as shown in Fig. 2.3c. More detailed TEM images of the advancing crack tip showed that the main crack can be temporarily arrested by multiple TBs, accompanied by the nucleation of a number of nanocracks ahead of its tip. In contrast to the single-crystalline aragonite, the fracture path in nanotwinned aragonite is substantially rough and curved due to the blocking and deflection by the TBs.

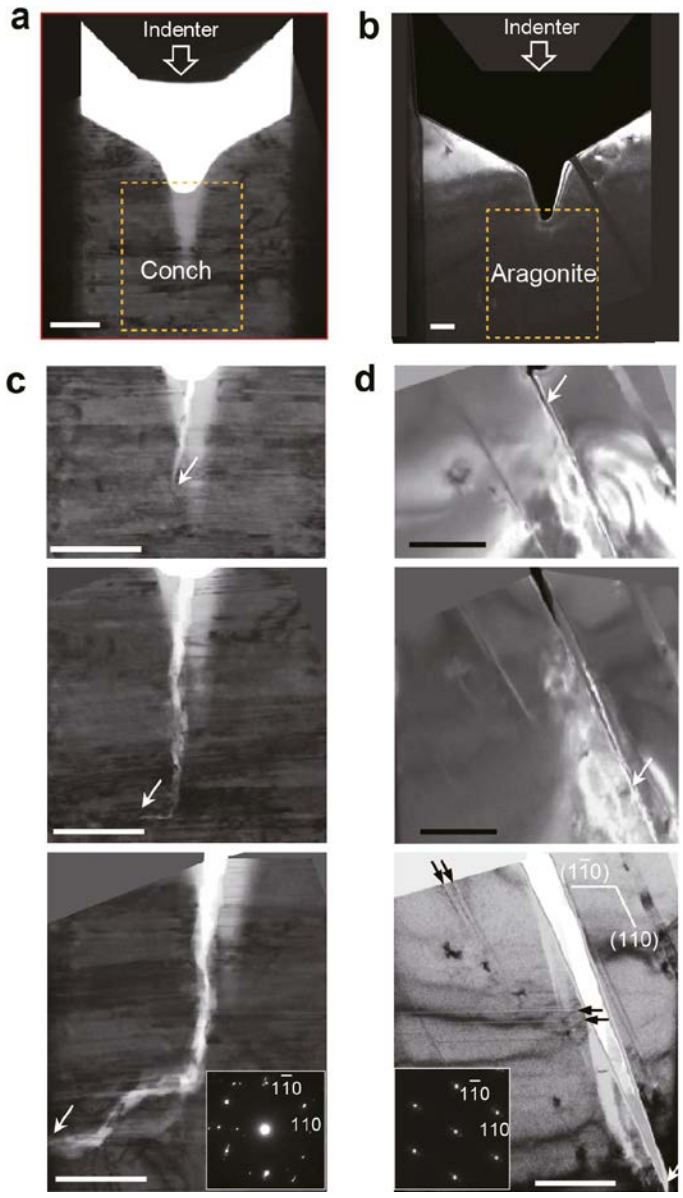

Figure 2.3 | Nanoscale toughness measurement by *in situ* TEM. **a-b,** TEM samples of conch shell and aragonite single crystal prepared using FIB for nanoscale toughness measurement. Scale bar, 500 nm. **c-d,** A sequence of TEM snapshots showing the crack propagation in the conch shell and aragonite single crystal. The crack tip is marked by white arrow in each image. The black arrows indicate the deformation twins formed along the $(1\bar{1}0)$ and (110) cleavage planes during the crack propagation in aragonite. The inset shows a [111] zone axis SAED pattern for each sample, indicating that the loading

direction was parallel to the $[1\bar{1}0]$ direction in both sample. Scale bar, 500 nm. (Courtesy of Prof. Sang Ho Oh)

2.3. Theoretical modeling: Finite Element Simulation

2.3.1. FEM calculation of J-integral according to CTOD.

To quantify the fracture resistance in the two specimens in Fig. 2.3, we measured the CTOD based on the δ_5 definition (55). In Fig. 2.5a, the measured CTOD is plotted against the crack extension distance. The crack in nanotwinned specimen exhibits a much larger CTOD than that in the single-crystalline specimen during extension. This suggests that the crack tip in nanotwinned aragonite becomes relatively blunt due to local phase transformation, whereas the crack tip in single-crystalline aragonite remains sharp, as typical for brittle fracture. To determine the fracture toughness of the material, I performed finite element modeling (FEM) to calculate the crack-tip J-integral (representing energy released per unit fracture surface area) following the same loading and geometrical conditions as in the experiments. Two-dimensional samples (Fig. 2.4) were constructed in ABAQUS following the same loading and geometrical condition as in the *in situ* TEM experiments. Aragonite was modeled as a homogeneous elastic material with Young's modulus of 120 GPa and Poisson's ratio of 0.3. The pre-existing crack was set to different lengths according the CTOD measurements. The J-integral value was calculated after loading until the CTOD in FEM matched with the experiment data.

The J-integral versus crack extension curve in Fig. 2.5b indicates that the fracture energy of the biogenic nanotwinned aragonite is about one order of magnitude larger than that of the twin-free aragonite single crystal. These results demonstrate that the pre-existing growth twins play an essential role in enhancing the fracture toughness of the conch shell.

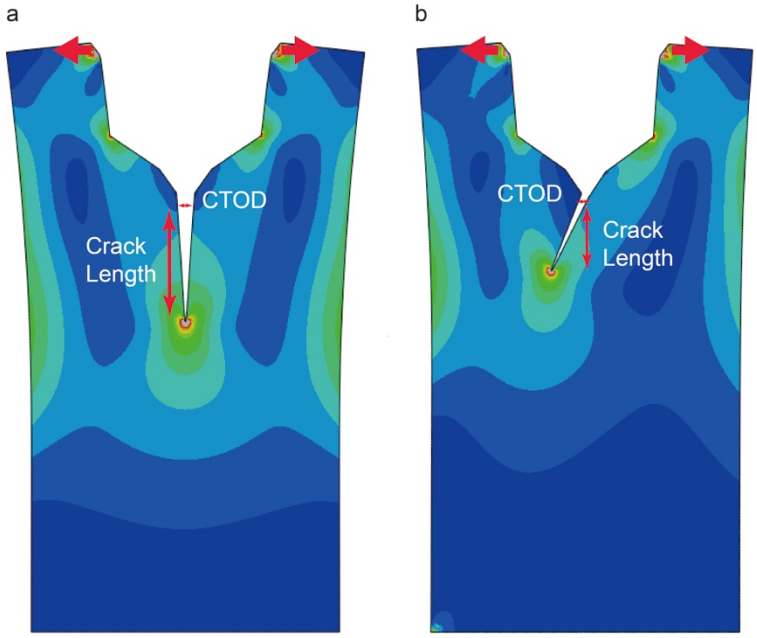

Figure 2.4 | FEM modeling of CTOD experiments. a-b, FEM models of the notched nanotwinned aragonite sample and single-crystalline aragonite sample. The sample geometries are the same as those in the experiment, and the red arrows indicate loading direction.

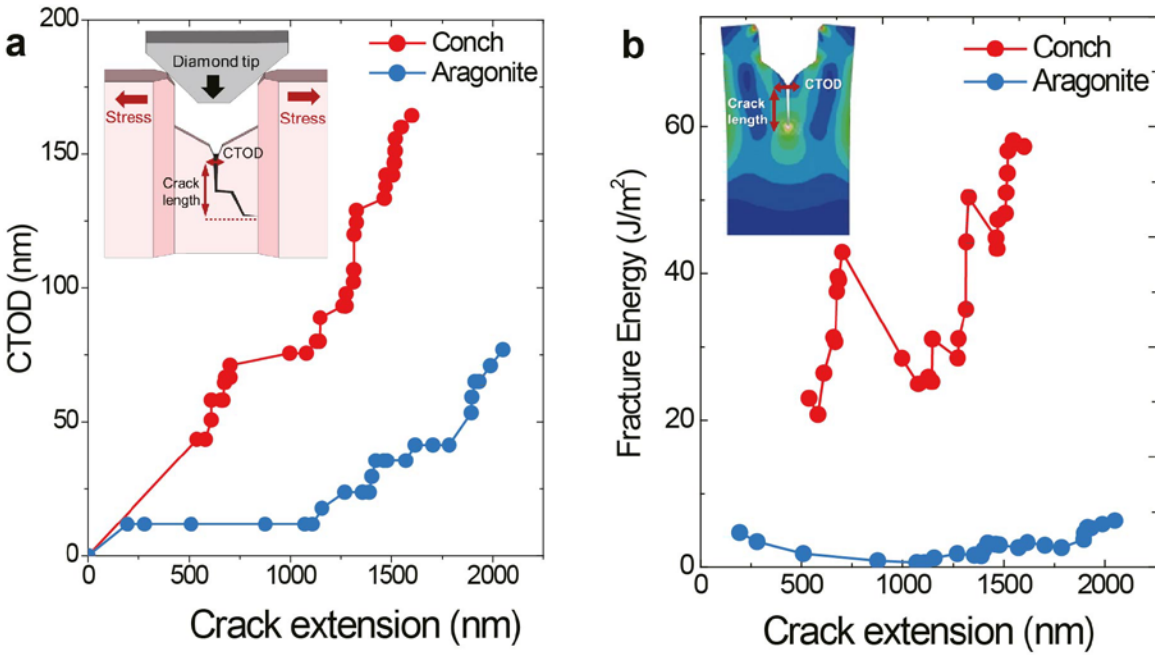

Figure 2.5 | Toughness measurement through CTOD by *in situ* TEM and FEM. a, CTOD as a function of the crack extension measured from *in situ* TEM. The inset is a conceptual representation about the measurement of CTOD and crack extension. **b,** Fracture energy versus crack extension from FE modeling.

2.4. Theoretical modeling: Molecular dynamics simulations

2.4.1. Molecular dynamics methodology

In aragonite sample, the out of plane direction is [001], the initial crack is created on the (010) plane along the [100] direction, when mode-I loading is applied on this crack, the material orientation is noted as *T*-orientation, and its mirror orientation by $(1\bar{1}0)_{TB}$ is noted as *M*-orientation. Three aragonite samples with controlled twin orientations were used for the simulations: a twin-free single-crystalline aragonite in *T*-orientation, a twin-free aragonite in *M*-orientation, and a nanotwinned aragonite with alternating *T*- and *M*-

orientations (referred to as nanotwinned aragonite) in which TBs are slanted with respect to an advancing crack along a cleavage plane (Fig. 2.6a-c). Each sample is about 50 nm wide, 100 nm long and 1.1 nm thick and contains about 0.5 million atoms. All the MD simulations were performed using software package LAMMPS (42). Interatomic forces in aragonite are described by an empirical potential (56), which includes Coulomb, LJ, harmonic angular and dihedral interactions. All simulated samples were initially relaxed and equilibrated at 5 K for 50 ps using Nosé-Hoover thermostat and barostat. Periodic boundary condition is imposed along the thickness direction of the samples. After relaxation, mode I loading is applied at a constant strain rate of about 2×10^{8} s^{-1}. During loading, an NVT ensemble with Nosé-Hoover thermostat is used to maintain a constant temperature. Visualization is processed via the software package, Ovito (57).

Based on linear elastic fracture mechanics, the critical energy release rate, referred to as the fracture energy, of a crack moving in a plane stress strip can be calculated from the following expression (58),

$$G = 2H\int_0^{\varepsilon_0}\sigma d\varepsilon$$

where H is the half width of the strip, and ε_0 is the critical strain at which the crack starts to propagate in the simulated sample, leading to a rapid drop in nominal stress (defined as the total force imposed on the sample divided by the initial cross-section of the sample in the crack plane). In atomistic simulations, almost all samples failed in a brittle manner, and the above equation was used to compute the fracture energy by integrating the stress vs. strain curve. For the nanotwinned aragonite sample, the crack blocking effect of TBs

induces a plateau in the stress vs. strain curve (Fig. 2.6e), giving rise to a higher fracture energy. In this case, the fracture energy was calculated by integrating the stress vs. strain curve from zero to the critical strain at the end of the stress plateau.

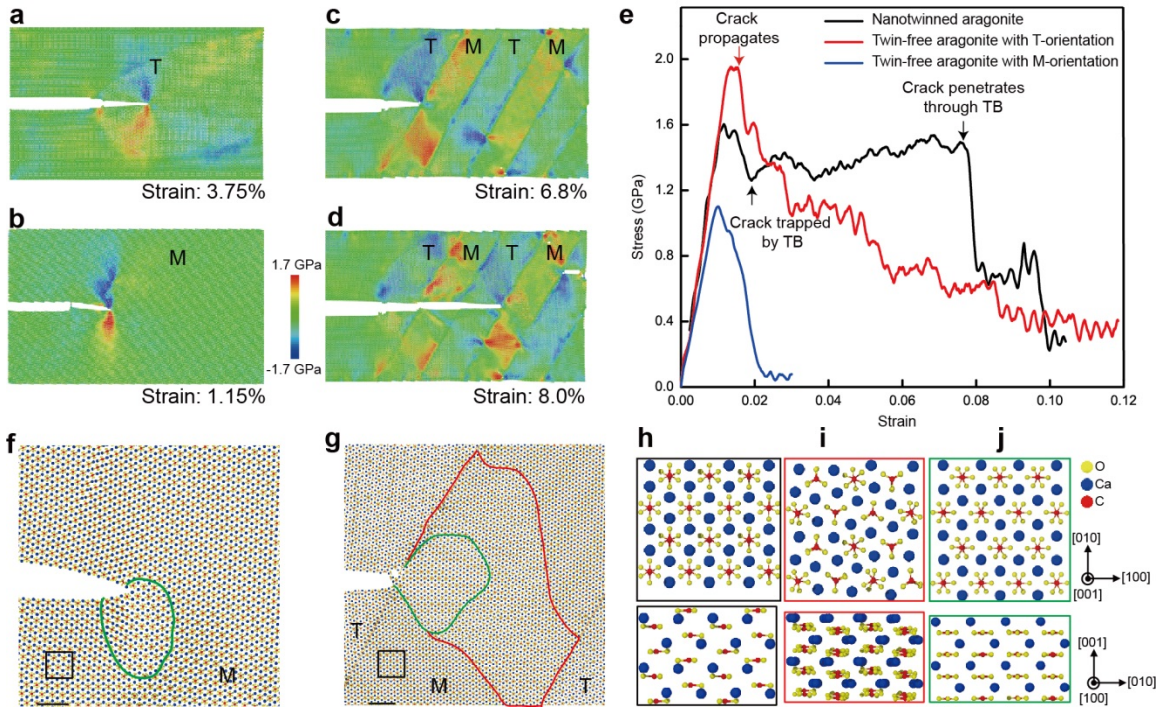

Figure 2.6 | Crack propagation in nanotwinned and twin-free aragonites. a-b, Snapshots of crack propagation in twin-free aragonite single crystals with different orientations under strains of 3.75% and 1.15%, respectively. The two orientations, denoted by 'M' and 'T', are related by $(1\bar{1}0)$ twin relationship. **c-d,** A sequence of snapshots of crack propagation in a nanotwinned aragonite. **e,** Stress-strain curves of nanotwinned and twin-free aragonites with the edge crack. **f-g,** Structural transformation at the crack tip in single-crystalline and twinned aragonite. The perfect matrix regions are outline by black lines, while the transformed regions are outlined by green and/or red lines. Scale bar, 2 nm. **h-j,** Typical atomic configurations of aragonite near crack tip before and after structural transformation. The pictures in **h**, **i** and **j** illustrate the lattice structures of the regions outlined by black, red and green lines in **f** and **g**, respectively.

2.4.2. Atomic simulation of crack interaction with TBs

To gain further insights into the atomistic mechanisms of how the nanotwinned microstructure enhances fracture resistance, I have performed large-scale molecular dynamics (MD) simulations of crack propagation in both nanotwinned and twin-free aragonites. The nanotwinned sample used in our simulations has TB spacing of 10 nm as in the conch shell. A sample with TB spacing of 20 nm was also tested to check the twin size effect on fracture toughness. In these nanotwinned samples, a crack is created on the (010) plane along the [100] direction, a cleavage crack plane of aragonite which is inclined with respect to the $(1\bar{1}0)_{TB}$. For the twin-free single-crystalline aragonite, I constructed two typical samples: one has the same crystallographic orientation as the twin domain (Fig. 2.6a), and the other has the orientation of the matrix (Fig. 2.6b), which are conveniently referred to as samples with T- and M-orientations, respectively.

In the twin-free aragonite with T- and M-orientations, deformation is localized in the vicinity of the crack tip, and the crack propagates smoothly, as evidenced by Fig. 2.6a-b. In contrast, the nanotwinned aragonite exhibits a very distinct fracture behavior. The crack is always trapped at TBs for some periods of time and the crack tip becomes blunted, due to sliding along the TB (Fig. 2.6c, d and g), which are very similar to the experimental observations (Fig. 2.3c, Fig. 2.8b-d). The in-plane stress contours in Fig. 2.6c-d further reveal substantial stress/strain delocalization (alternating stresses with opposite signs) around the crack tip. These phenomena are also revealed by the FEM simulations in part 2.4.4 (Fig. 2.9). The results from both atomistic and FEM simulations demonstrate that TBs can act as effective obstacles to crack propagation, the phase transformation will occur in front of the crack tip and lead to crack blunting and

delocalization of deformation, which facilitates energy dissipation and delays catastrophic crack propagation.

Our atomistic simulations not only showed phase transformation near the crack tip (Fig. 2.6f-g), but also revealed the detailed mechanism involving a coordinated rotation of some carbonate groups (CO_3) over the transformed region driven by the crack-tip stress field, as can be seen from the typical atomic configurations of aragonite before and after the transformation (Fig. 2.6h-j). Such phase transformation is irreversible, i.e. the transformed regions cannot spontaneously recover upon unloading. Similar stress-driven phase transformation was also observed at the crack tip of nanotwinned aragonite under the nanoindenter (Fig. 2.8c-d) in the following part and in previous MD simulations of calcite deformation under high pressure (59). It is noted that in the single-crystalline aragonite, the phase transformation occurs before crack initiation, and the transformed region is highly limited (Fig. 2.6f). In contrast, for the nanotwinned aragonite, large-scale phase transformation is activated once the crack is trapped by a TB and spreads through the nanoscale twins (Fig. 2.6.g), resulting in delocalization of phase.

Figure 2.6e shows the stress-strain curves from our present simulations of nanotwinned and twin-free aragonites. The plateaus in the stress-strain curve of nanotwinned aragonite correspond to the crack being trapped by TBs. Based on the method in 2.4.1, the fracture energies of twin-free aragonites with T- and M-orientations are 0.55 J/m^2 and 0.28 J/m^2, respectively. Remarkably, the fracture energy of the nanotwinned aragonite with alternating T- and M-orientations is found to be around 5.13 J/m^2, which is approximately an order of magnitude higher than that of the twin-free aragonite. This dramatic enhancement in fracture toughness of nanotwinned aragonite is consistent with

our CTOD experimental measurements, and the simulation results provide strong evidence that the toughening effect originates from TBs impeding crack propagation and inducing delocalized phase transformation. In addition, I have also conducted MD simulations of crack propagation in nanotwinned samples with TBs parallel to the initial crack (Fig. 2.7). The results indicate that the presence of TBs cannot increases the fracture toughness of aragonite significantly if the TBs are parallel to the initial crack. This suggests that the relative orientation between the TBs and crack is a factor that affects the fracture resistance, and points to the importance of crossed lamellar stacking in upper level hierarchy (i.e. first and second order lamellae) in hindering crack propagation from different directions.

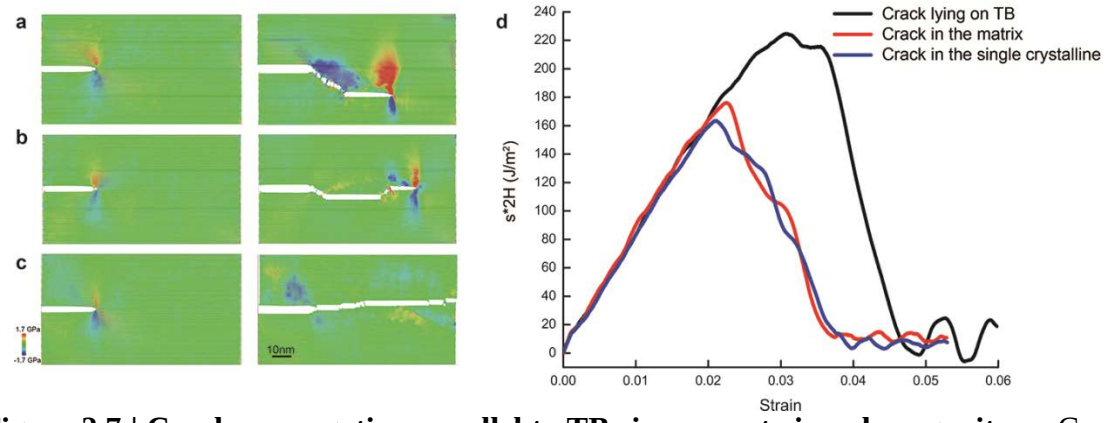

Figure 2.7 | Crack propagation parallel to TBs in a nanotwinned aragonite. a, Crack propagation in nanotwinned aragonite with a crack initially lying on a TB. **b,** Crack propagation in nanotwinned aragonite with a crack initially parallel to TB in the matrix domain. **c,** Crack propagation in single-crystalline aragonite. Here the initial crack is parallel to [110]. Crack deflection is clearly observed in **a-c**, where color represents the in-plane shear stress. **d,** Stress-strain curves of samples in (**a-c**).

2.4.3. Experiment verification of crack interaction with TBs

Our atomistic simulations revealed that there exists a significant phase transformation region near the crack tip in the twinned aragonite sample while the transformation in single crystalline aragonite is very limited. To identify this mechanism, the microstructural changes near the crack tip were investigated carefully by using HRTEM after the *in situ* TEM fracture experiments. Fig. 2.8b shows a representative TEM image of an advancing crack tip in nanotwinned aragonite, which is temporarily arrested by a pre-existing TB, indicating that TBs can effectively block the crack propagation. The HRTEM images in Fig. 2.8c-d further reveal that there exists a mixture of amorphous and nanocrystalline phases around the crack tip. Such amorphization and formation/re-orientation of nanograins are induced by the elevated stress field in the vicinity of the crack tip. It indicates that when a crack is trapped by a TB, the region around the crack tip can undergo severe plastic deformation. This is further demonstrated by apparent crack blunting in Fig. 2.8d. For the single-crystalline aragonite, deformation twinning is found to be operative near the crack, as revealed by Fig. 2.8e-f. Some deformation twins are captured in Fig. 2.8f, and the corresponding twin-matrix crystallographic relation is shown in the HRTEM image (Fig. 2.8g). The TEM diffraction patterns show that {110}-type deformation twinning is a dominant mode in single-crystalline aragonite. Although deformation twinning can dissipate energy to some extent, it cannot effectively hinder crack propagation, as evidenced by the sharp crack tip in Fig. 2.8h and the catastrophic cleavage fracture shown in Fig. 2.3d. The HRTEM examination shows no phase transformation occurs near the crack tip in the single-crystalline aragonite (Fig. 2.8h). The differences in crack-tip deformation modes between nanotwinned and single-

crystalline aragonite is consistent with our MD simulations and indicate that the pre-existing growth twins in nanotwinned biogenic aragonite are uniquely effective in blocking crack advance and enhancing energy dissipation via phase transformations in the vicinity of the crack tip, leading to higher fracture toughness shown in Fig. 2.5a-b.

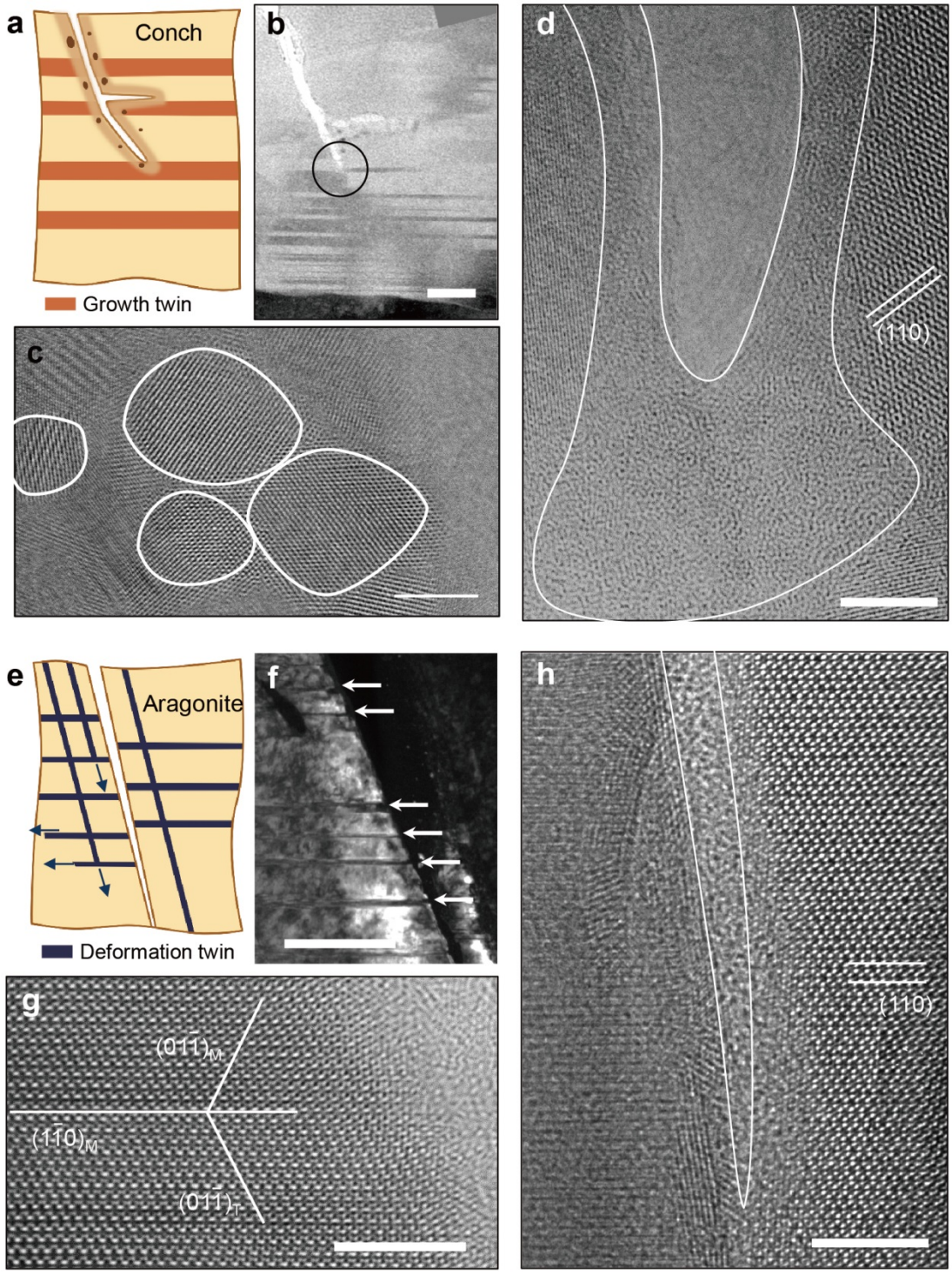

Figure 2.8 | Nanotwin governed toughening mechanisms in experiments. **a**, Schematic illustration of toughening mechanisms in the nanotwinned aragonite of conch shell, including crack-tip branching, blunting and phase transformation. The formation of amorphous and nano-grains are highlighted as different color along the periphery of

crack. **b,** TEM image showing a crack tip arrested by nanoscale growth twins in the conch shell. Scale bar, 50 nm. **c-d,** HRTEM images of the edge of fractured surface of the conch shell. Some of nano-grain and amorphous phases are outlined by white dotted lines in **c** and **d**, respectively. Scale bar, 5 nm. **e,** Schematic illustration of crack tip plasticity (deformation twinning) in single-crystalline aragonite. The deformation twins are formed along the $(1\bar{1}0)$ and (110) planes. **f,** TEM image of a typical crack in single crystal aragonite. Some deformation twins nucleated from crack tip are indicated by white arrows. Scale bar, 50 nm. **g,** HRTEM image of a deformation twin formed along the $(1\bar{1}0)$ plane. Scale bar, 5 nm. **h,** HRTEM image of crack tip in single-crystalline aragonite. No phase transformation is observed along the atomically cleaved fracture surfaces. Scale bar, 5 nm. (Courtesy of Prof. Sang Ho Oh)

2.4.4. Cohesive modeling of crack propagation in twinned aragonite

From MD simulation and *in-situ* TEM observation, the fracture properties and related phase transformation shows significantly difference depending on the material orientation (Fig. 2.6e-g). The crack tends to propagate in a brittle manner in single crystalline phase, however, when growth twinning exists, phase transformation and delocalization will be activated due to the anisotropy. Inspired by the results from MD simulation, crack propagation in the twinned aragonite was simulated using a finite element method (FEM) with cohesive elements (Fig. 2.9). Different cohesive properties in T-phase and M-phase were assumed and phase transformation was simulated through simplified plastic deformation. In addition, the elastic anisotropy of twin/matrix phases and the boundary sliding effect were also considered.

The FEM simulations were performed with ABAQUS/Explicit on notched samples consisting of alternating twin and matrix phases. Both phases were modeled using 4-node

CPS4R elements with anisotropic elasticity and isotropic hardening plasticity with different crystallographic orientations. The crack is modeled by cohesive elements with different parameters in the twin and matrix phases. To model crack blunting effects due to TB sliding, the TBs are also modeled by cohesive elements. Both crack and TBs are modeled by COH2D4 cohesive elements in ABAQUS, for which typical linear triangular traction-separation law and maximum nominal stress criterion are adopted. To model TB sliding, the critical cohesive stress in the normal direction are set high enough to ensure no softening in nominal direction and the cohesive stress in the tangential direction corresponds to the critical sliding stress for TBs. Cohesive energy is set very high to ensure a negligible softening in shear stress during sliding. A constant velocity loading is applied on the top surface of the sample and the strain rate is set low enough to ensure a quasi-static process.

Figure 2.9a-f shows some representative snapshots from the FEM simulations for different samples under different sliding conditions. In the cases of single-crystalline twin and matrix phases, the crack rapidly runs through the overall sample along the given cleavage surface (Fig. 2.9a-b), showing a brittle fracture mode with very limited phase transformation (plasticity). The fracture toughness of the two phases is 0.8 and 14 J/m^2, respectively (Fig. 2.9h). However, in the twinned sample, the crack will be trapped at the TBs for a while due to the significant difference in fracture properties in twin/matrix phases. During the period of crack trapped by a TB, plastic deformation delocalizes to the next weak phase far from crack tip, resulting in additional plastic dissipation, as shown in Fig. 2.9c-d. By introduce the alternately strong and weak phases through twinning, the

phase transformation will be activated and delocalized which is consistent with our MD simulation observation, and the toughness of the system increases significantly to 49 J/m^2.

Once the TB sliding effect is also considered by controlling the cohesive stress in the tangential direction of TB, I can observe apparent crack tip blunting and TB sliding (Fig. 2.9e-f). Figure 2.9g and 2.9h show the stress-strain curves and associated fracture energies from different modeling cases, respectively. It indicates that the introduction of TB sliding can significantly enhance the facture toughness.

Some main parameters used in FEM modeling are given as follows:

(a) Twin phase: cohesive stress 3 GPa, yielding stress 1.2 GPa, and fracture energy 1 J/m^2;

(b) Matrix phase: cohesive stress 9 GPa, yielding stress 4 GPa, and fracture energy 1 J/m^2;

(c) Sliding boundary: cohesive stresses in the normal and tangential directions are set to 500 and 1.6-4 GPa, respectively;

(d) Anisotropic elastic constants(60) for aragonite: C_{11}=164.4 GPa, C_{22}=112.0 GPa, C_{33}=59.2 GPa, C_{12}=65.3 GPa, C_{13}=39.0 GPa, C_{23}=48.2 GPa, C_{44}=40.5 GPa, C_{55}=33.9 GPa, and C_{66}=49.0 GPa.

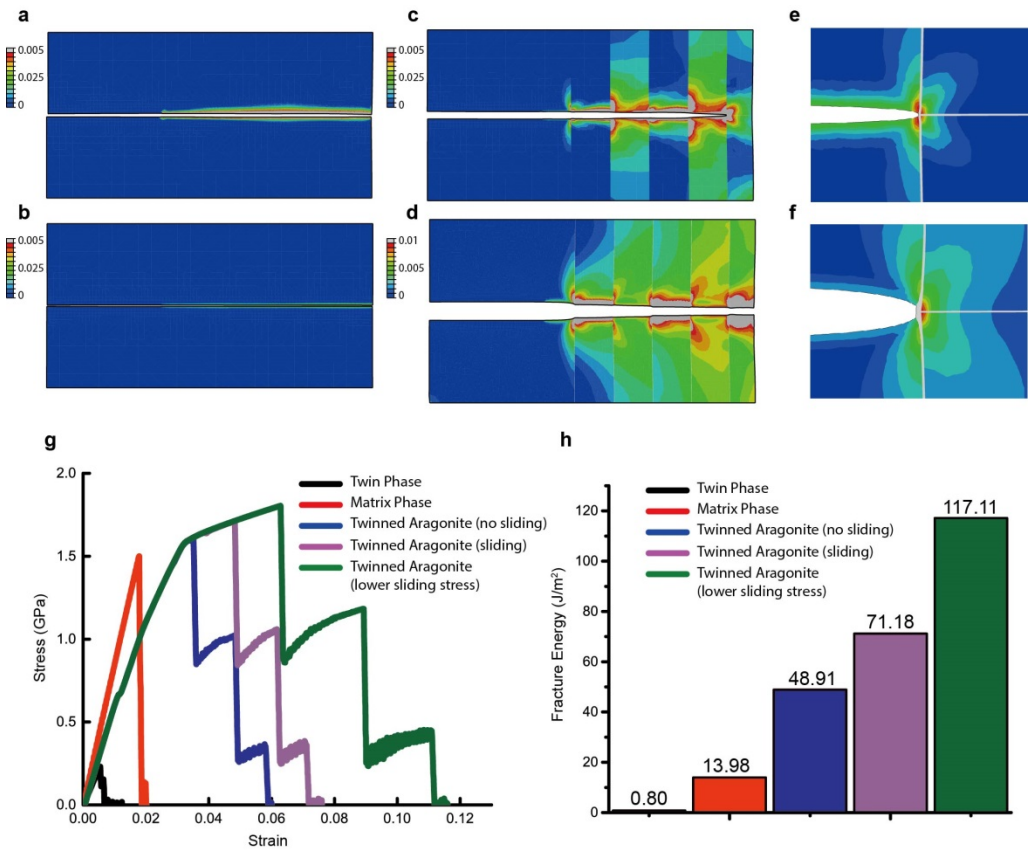

Figure 2.9 | FEM modeling of crack propagation in twinned aragonite with TB. a-b, Crack propagation in single twin and matrix phases. Very limited plastic strain observed in these two single-crystalline samples. **c-d,** Crack propagation in twinned aragonite without and with boundary sliding. **e-f,** Configurations of the crack tip without and with boundary sliding. **g,** Stress-strain curves of different modeling cases. **h,** Fracture energy of different modeling cases. Colors in **a-f** represent the effective plastic strain.

2.5. Theoretical modeling: Self-similar model for optimized hierarchy of conch shell

Previous theoretical models (61-63) have predicted that the fracture toughness of self-similar hierarchical materials increases exponentially with the number of hierarchical levels, and this has also been demonstrated by experimental and computational studies

(64, 65). To further validate/complement the results from both experiments and simulations, I have extended a theoretical model of the self-similar hierarchical materials (63). According to a bottom-up design route of the self-similar model (63), an optimal 3-level hierarchical structure, referred to as a conch-like material, is built by determining the geometry and mechanical properties (including the stiffness, strength and toughness) of all levels. I evaluated the contribution of nanoscale twins in the third-order lamellae to the overall fracture toughness of the conch shell.

2.5.1. Self-similar model

In this model, each hierarchical level has a similar structure of staggered hard plates embedded in a soft organic matrix, and the structure of each level serves as hard plates at the next level, as illustrated by Fig. 2.10a. Under uniaxial tensile stress, the hard plates primarily carry load by tension while the protein matrix transfers load to neighboring plates by shear (46) (Fig. 2.10b). Under the assumption that such hierarchical structure has evolved into optimized stiffness and toughness, a flaw-tolerance criterion is used to determine the characteristic width h_n of hard inclusion at the *n*-th level as,

$$h_n \le \frac{E_n \Gamma_n}{S_n^2},\ n = 0, 1, 2, ..., N \tag{2.1}$$

where E_n, S_n, Γ_n denote the Young's modulus, strength and fracture energy at the *n*-th level, respectively. At the lowest level (i.e. n=0), the basic properties of the mineral are defined as,

$$E_0 = E_m,\ S_0 = \sigma_m,\ \Gamma_0 = 2\gamma_m \tag{2.2}$$

where E_m is the Young's modulus, σ_m the theoretical strength and γ_m the fracture surface energy of mineral.

In the optimized hierarchical structure, the hard inclusion and soft matrix simultaneously reach their failure strengths. Accordingly, the aspect ratio $\rho_n=l_n/h_n$ of hard inclusion at the n-th level can be determined as (46, 61, 63),

$$\rho_n = \frac{S_n}{\tau_n^p}, n = 0, 1, 2, ..., N-1 \tag{2.3}$$

where S_n is the tensile strength of the inclusion and τ_n^p represents the failure stress of the protein matrix. The Young's modulus at the n-th level is expressed as (46, 61, 63),

$$E_n = \left[\frac{4(1-\varphi_{n-1})}{G_{n-1}^p \varphi_{n-1}^2 \rho_{n-1}^2} + \frac{1}{\varphi_{n-1} E_{n-1}} \right]^{-1} \tag{2.4}$$

The strength at the *n*-th level is,

$$S_n = \min\left(\frac{1}{2}\varphi_{n-1}\rho_{n-1}\tau_{n-1}^p, \frac{1}{2}\varphi_{n-1}S_{n-1}\right) \tag{2.5}$$

where φ_{n-1} and ρ_{n-1} denote the volume fraction and aspect ratio of the hard inclusions, while G_{n-1}^p and τ_{n-1}^p represent the shear modulus and strength of the soft matrix, respectively. The fracture energy at the n-th level is estimated as (63),

$$\Gamma_n = (1-\varphi_{n-1})h_{n-1}\rho_{n-1}\int \tau d\varepsilon + \varphi_{n-1} 2\gamma_m, \ n = 1, 2, ..., N-1 \tag{2.6}$$

Here I assume that the dissipation of protein matrix obeys a power-law constitutive equation,

$$\varepsilon = K\tau^M, \text{ where } M > 1 \tag{2.7}$$

Thus, the fracture energy can be re-written as,

$$\Gamma_n = (1-\varphi_{n-1})h_{n-1}\rho_{n-1}\frac{M}{1+M}K\tau^{M+1} + \varphi_{n-1}2\gamma_m, \text{ where } \tau = \min(\tau_{n-1}^p, \frac{S_{n-1}}{\rho_{n-1}}) \quad (2.8)$$

For the strain hardening index *M*, I fit the stress-strain curves from the literature(51) and find it to be 1.6~3.2. Moreover, I assume that the soft matrix at every level have the same mechanical properties, i.e.,

$$\tau_n^p = \tau^p, G_n^p = G^p, \Theta_n^p = \Theta^p \text{ and } \Theta^p = K(\tau^p)^M \quad (2.9)$$

where τ^p, G^p, Θ^p represent the shear strength, shear modulus and failure shear strain of the proteinacious matrix, respectively. For the present quasi-self-similar model, Φ is taken to be about 95%, and the volume fraction of hard inclusions at each level is assumed to be identical, i.e.,

$$\varphi_n = \Phi^{1/N}, n = 0, 1, 2, ..., N-1 \quad (2.10)$$

Following the above equations, I can construct a quasi-self-similar hierarchical material with optimized properties. For a 3-level hierarchy like conch shell, if I substitute the following parameters into the above equations,

E_m=100 GPa, σ_m=E_m/75, γ_m=1 J/m^2, τ^p=σ_m/25, G^p= E_m/1000,

Θ^p=1, Φ=0.95, M=1.6~3.2,

I can obtain the optimized material properties at each level of the hierarchy. The relevant results are shown in Fig. 2.10c-d.

2.5.2. Results and Discussion

As shown in Fig. 2.10c, the overall toughness of the conch-like hierarchical material increases dramatically as the lowest-level mineral fracture energy is enhanced. Figure 2.10d provides a direct prediction that if the fracture toughness and strength of the

lowest-level structure are increased only 2-3 times, the overall toughness of the hierarchical material will increase by one order of magnitude. These results indicate that the lowest-level structure plays a crucial role in increasing the overall toughness of the conch-like material by driving energy dissipation in the organic matrix at all upper levels.

Our experiments and simulations have shown that nanoscale twins enhance the fracture energy of the lowest-level structure in the aragonitic shell of *Strombus gigas* by about one order of magnitude. In comparison, the overall fracture energy of the conch shell is known to be about 3 orders of magnitude higher than that of the single-crystalline aragonite. Together with the above theoretical analysis, we conclude that the nanotwin-toughened-third-order-lamellae are able to drive larger scale energy dissipation in the second- and first-order lamellae structures, leading to an exponential increase in the overall fracture energy of the material as we move up in hierarchy, in agreement with the existing theoretical models on self-similar hierarchical materials.

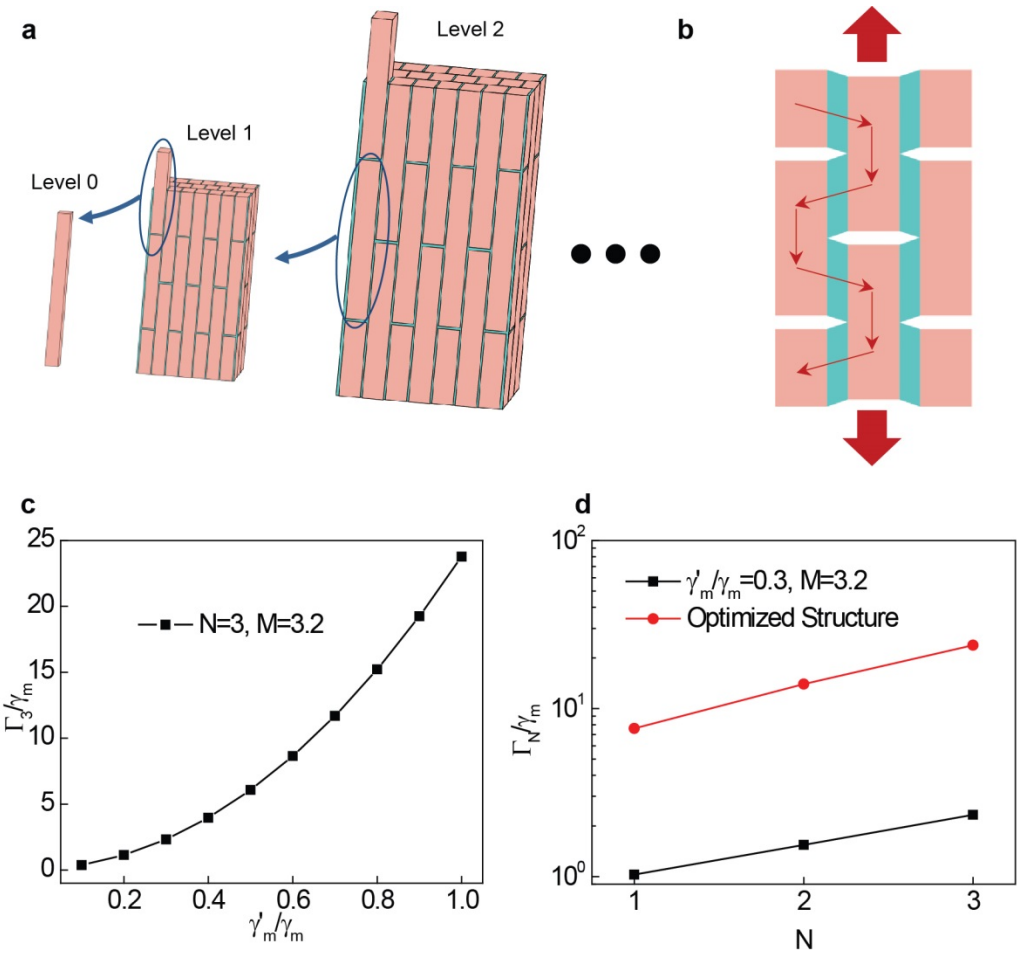

Figure 2.10 | Model of quasi-self-similar hierarchical structure. a, Schematic illustration of the quasi-self-similar hierarchical model. Each level consists of staggered hard mineral inclusions (pink) embedded in a soft organic matrix (green). **b,** A tension-shear chain model showing mineral inclusions carry load primarily by tension and the organic matrix by shear. **c,** Toughness of the 3-level hierarchical structure as a function of the lowest-level mineral fracture energy $2\gamma'_m$. **d**, Variations of toughness with number of hierarchical levels *N*. Here γ_m denotes the intrinsic fracture energy of mineral, which is about 1 J/m^2. *M* represents the strain hardening index of the soft matrix.

2.6. Summary

Our present work has demonstrated the crucial role of biogenic growth twins in the mechanical properties of biological materials. Although the nanotwinned structure seems beneficial for both engineering and biological systems, the toughening mechanisms in biogenic nanotiwnned aragonite are distinct from those observed in man-made nanotwinned metals. For example, a recent *in situ* TEM study (18) revealed that, in nanotwinned metal foils, dislocations are emitted from a moving crack-tip and impinge on TBs ahead of the crack, leading to the formation of dislocation walls on the TBs which become impenetrable to further dislocation motion and hinder the propagation of the crack. In contrast, the mineral in biological materials has ionic bonding and is nominally brittle, and the underlying mechanisms for energy dissipation has been identified here as crack trapping at TBs, multiple nanocracking, phase transformation and strain delocalization driven by the crack-tip stress field.

In summary, the present study clearly indicates that nanoscale growth twins in *Strombus gigas* conch shell play a critical role in the mechanical properties of the material. *In situ* nanoindentation-based fracture experiments on both nanotwinned and twin-free specimens from *Strombus gigas* and single-crystalline aragonite reveal that the TBs of nanoscale growth twins can effectively block crack propagation and induce phase transformation in the vicinity of the crack-tip, leading to the delocalization of deformation and efficient energy dissipation that delay catastrophic fracture, which is corroborated by atomistic simulations and FEM modeling. The results from both experiments and simulations show that the nanotwinned microstructure improves the fracture toughness of aragonite by roughly an order of magnitude. These findings provide

a fundamental understanding of the contribution of hard basic building blocks at nanoscale to fracture resistance of the overall structure, which complement our previous knowledge about the roles of soft organic content and bio-composite structure in the toughness of bio-materials. The present study may also have profound impact on the design of strong and tough biomimetic materials with minimum organic content.

Chapter 3 Recoverable plasticity in penta-twinned metallic nanowires

The work described in this Chapter is in collaboration with the experimental group of Prof. Yong Zhu (66). Dr. Qingquan, Dr. Guangming Chen and Tzu-Hsuan Chang in Prof. Zhu's group performed the *in situ* experiments.

3.1. Introduction

One-dimensional (1D) nanostructures are widely regarded as among the most important building blocks for a broad range of applications including nanoelectronics, optoelectronics, energy harvesting and storage, ultrasensitive sensing, and nanoelectromechanical devices (29, 30). 1D nanostructures commonly exhibit ultrahigh mechanical strength, which make them also ideal candidates for studying fundamental deformation mechanisms at the nanoscale (31-33). In the case of metallic nanowires (NWs), dislocation nucleation from free surfaces has been identified as a dominant deformation mechanism, in contrast to the forest dislocation dynamics in bulk materials (67-73). Recently, NWs with internal microstructures have received much interest. For instance, metallic NWs with different types of twin boundaries (TBs) have been studied, including parallel, inclined or perpendicular TBs with respect to the NW length direction (34, 35, 74-77). However, there has been relatively little study on time-dependent responses of NWs under sustained or cyclic loadings, in spite of the obvious importance of this subject to the function and reliability of NW-based devices.

A number of recent experimental and computational studies have revealed substantial time-dependent and partially reversible deformation behavior in small-scale materials with characteristic length scale below 100 nanometers (78), especially nanocrystalline metal thin films (79-82). Such behavior has been attributed to the coupling and competition of reversible dislocation activities and grain boundary (GB)-mediated processes at different temperature and strain rates (83-89). At relatively high temperatures and small strain rates, GB diffusion/sliding can dominate the time-dependent behavior, while dislocation nucleation and motion become more prevalent at lower temperatures and larger strain rates. More recently, atomistic simulations predicted a reversible transition between two crystal orientations during loading, leading to shape memory and pseudoelastic behavior for several face-centered-cubic (FCC) single-crystalline metal NWs (68, 90-92). This phenomenon was attributed to the formation of defect-free twins facilitated by relatively low stacking fault energy, nanometer size scale and surface stress.

In this chapter, I report an unusual time-dependent deformation behavior in penta-twinned Ag NWs, with stress relaxation upon loading and complete strain recovery upon unloading. Large-scale atomistic simulations are performed to explore the mechanisms underlying the observed behavior in detail and to show the critical role of the penta-twinned nanostructure on this response.

3.2. Experimental studies

3.2.1. Structural characterization and *in situ* TEM tensile testing

Microstructure characterization of single-crystalline and penta-twinned Ag NWs is shown in Fig. 3.1 by Prof.Yong Zhu's group.

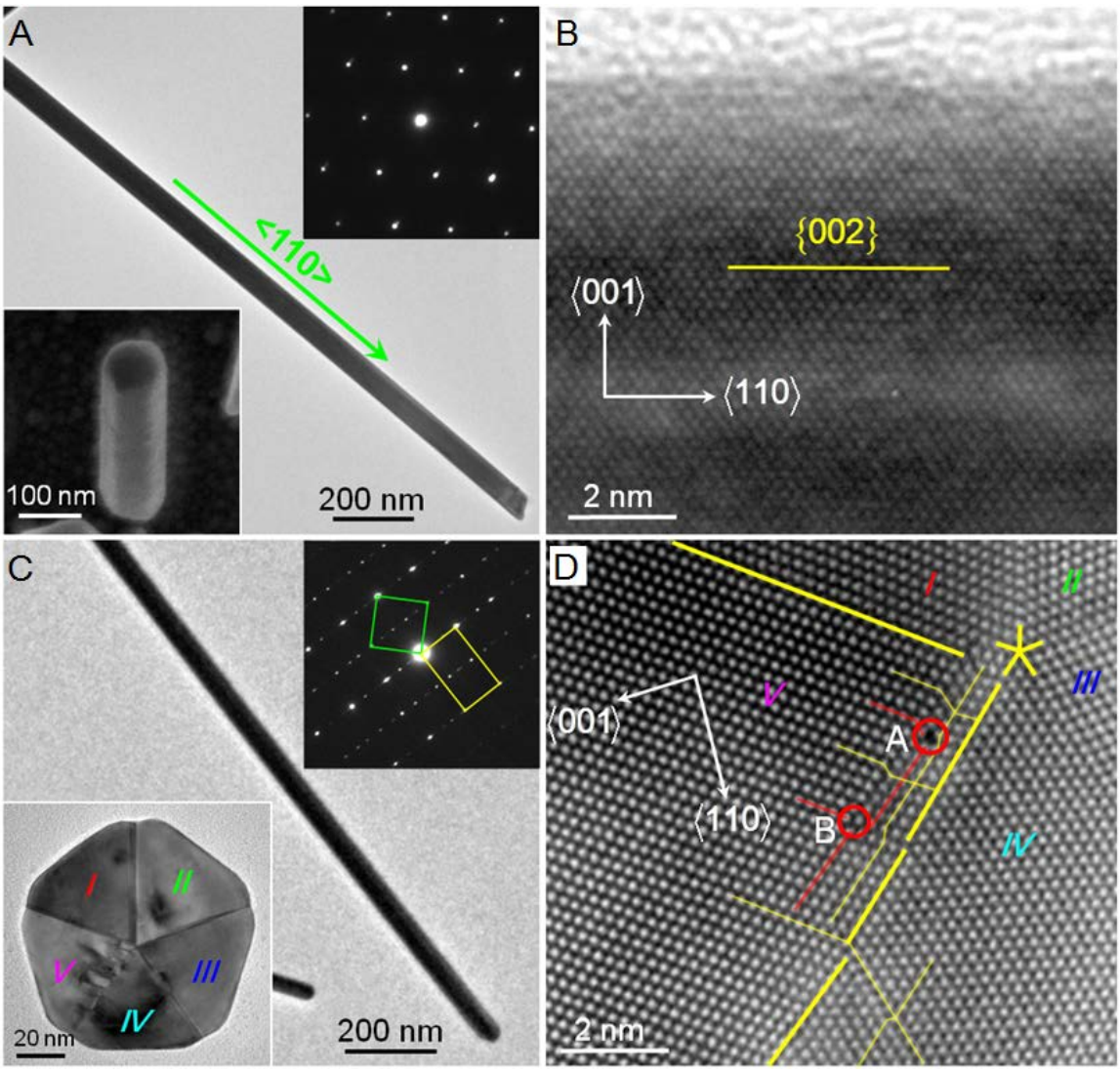

Figure 3.1 | Structural of single crystal and penta-twinned Ag NWs. **a-b,** Low-magnification and high-resolution TEM images of single crystal Ag NW with growth direction of <110>. Scale bar, 200nm and 2 nm respectively. Right and left insets (scale bar, 100nm) in (a) show the SAED pattern taken from <110> zone axis and the hexagonal cross-sectional shape from SEM observation, respectively. **c,** TEM image of Ag NWs showing five-fold twinned structure. Scale bar, 200nm. Right and left insets (scale bar, 20nm) in (c) display the corresponding SAED pattern and the pentagonal cross-sectional shape, respectively. Stacking faults along the boundary between grains IV and V can be clearly seen in the left inset of (c). **d**, HAADF STEM image of the cross-sectional sample showing the presence of vacancy defects near the boundary between grains IV and V. The yellow star in (d) indicates the center of the cross-sectional sample. Scale bar, 2nm. (Courtesy of Prof. Yong Zhu and Dr.Guangming Chen)

In-situ tensile experiments inside an SEM and a TEM were performed using a microelectromechanical system (MEMS)-based testing system that allows accurate measurement of both load and displacement simultaneously (93-96) by Prof. Yong Zhu's group, as shown in Fig. 3.2a. Load is applied using a thermal actuator on one side of the testing stage and measured using a differential capacitive sensor on the other side. Displacement (and strain) is measured by digital image correlation of SEM images of two local markers on the specimen. This MEMS-based system has a strain resolution of 0.01% (gage length 2 μm) and a stress resolution of 1.4 MPa (e.g., for NW diameter of 104 nm).

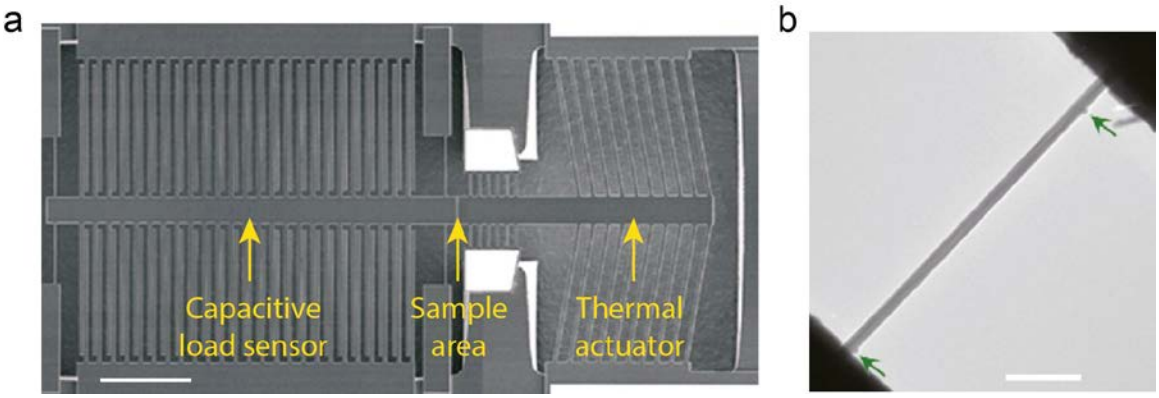

Figure 3.2 | TEM tensile testing of NWs. **a**, The MEMS stage used for *in-situ* SEM and TEM tensile testing of Ag NWs. Scale bar, 200nm. **b**, Low-mag TEM image of a NW bridged between the actuator and the load sensor, with two marks (arrowed) for displacement measurement. Scale bar, 500nm. (Courtesy of Prof. Yong Zhu and Dr.Guangming Chen)

3.2.2. Time-dependent deformation behavior in penta-twinned Ag NWs

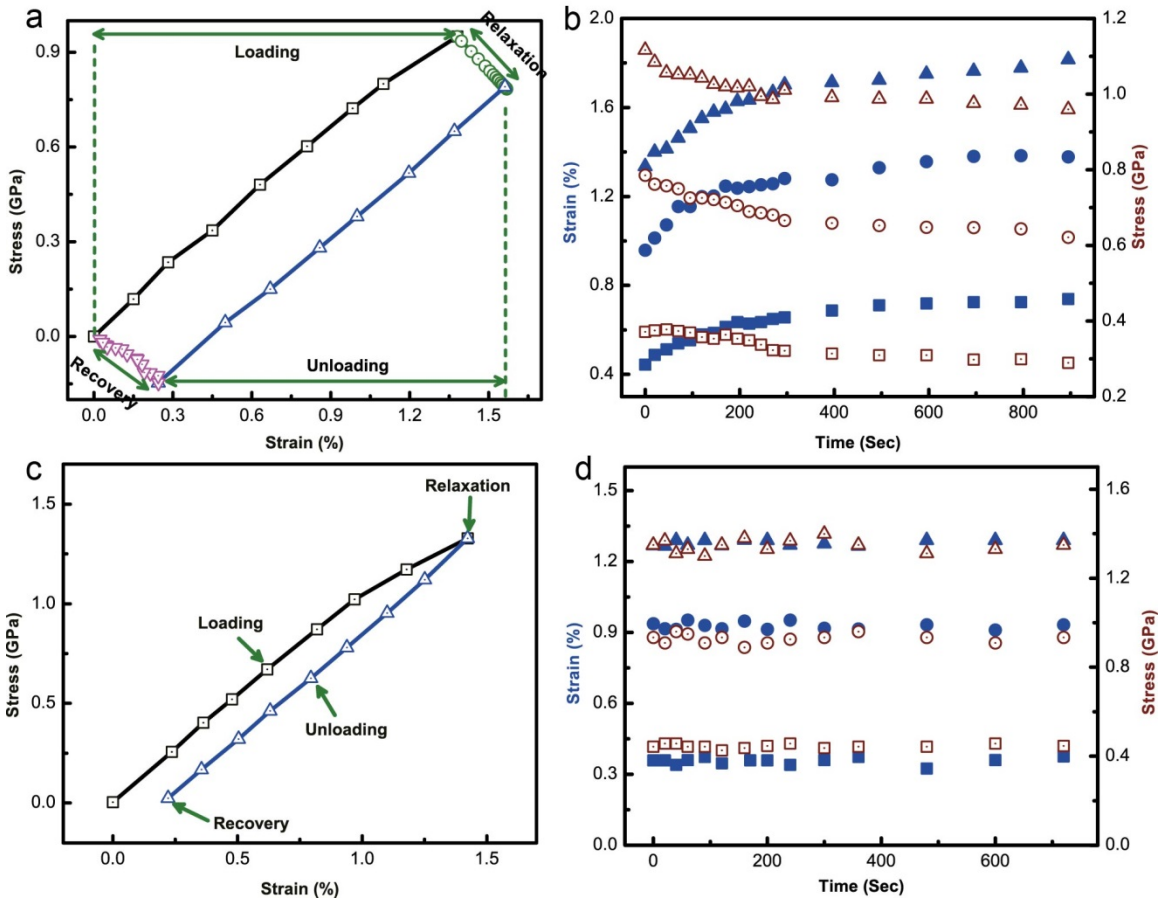

Figure 3.3 | Strain and stress evolutions as functions of time. **a, c**, Stress-strain curves for a penta-twinned Ag NW (120 nm in diameter) and a single-crystalline Ag NW (99 nm in diameter). Note that in both cases the relaxation and recovery steps took 15 minutes each. **b, d**, Relaxation curves for a penta-twinned Ag NW (104 nm in diameter) and a single-crystalline Ag NW (71 nm in diameter). Note: Solid and open symbols correspond to the strain-time and stress-time relationships, respectively. Square, circle and triangle symbols correspond to 1st, 2nd and 3rd stress levels, respectively. (Courtesy of Prof. Yong Zhu and Dr.Guangming Chen)

Figure 3.3a shows the stress–strain response during a typical tensile test of a penta-twinned Ag NW in four steps: loading, relaxation, unloading and recovery. During the loading step, the NW exhibited nearly linear response (slightly nonlinear when the

applied stress is high). During the relaxation step, the stress decreased with time while the strain increased. Figure 3.3b shows the strain and stress as functions of time at three stress levels. When the initial stress is ~ 0.37 GPa, the NW strain increased monotonically with time from 0.44% to 0.74%, while the stress decreased monotonically from 371 MPa to 290 MPa. Upon unloading, the strain in the NW completely recovers in about the same amount of time as the relaxation. The same procedure was repeated for the relaxation and recovery steps at two additional stress levels (with initial stresses of 0.79 and 1.12 GPa), corresponding to the circle and triangle symbols in Fig. 3.3b, respectively. The same experiments were conducted for five single-crystalline Ag NWs with diameters of 71, 99, 111, 130 and 152 nm at similar stress levels as that used for penta-twinned Ag NWs, but neither stress relaxation (Figs. 3.3c-d) nor recovery of plastic strain (Fig. 3.3d) was observed in any of them.

3.3. Atomistic simulations

To reveal the underlying mechanisms behind the observed relaxation and recovery behaviors of penta-twinned Ag NWs, I performed a series of molecular dynamics simulations.

3.3.1. Simulation methodology

Large-scale molecular dynamics simulations were performed using the software package LAMMPS (42). Three kinds of NW samples are generated: a penta-twinned NW with a five-fold twin, a bi-crystalline NW with a single coherent twin boundary (TB) in the middle, and a single-crystalline NW. Figure 3.4 shows the atomic configurations of

the three kinds of simulated samples. Each sample is 30 nm in diameter and 30 nm in length, and contains about 1.3 million atoms. The embedded atom method (EAM) potential for Ag(97) is used to describe the interatomic interactions. The vacancies are introduced by randomly removing atoms out of the samples.

The samples are initially relaxed and equilibrated at an elevated temperature of 800 K (about 65% of the melting point of Ag) for 80 ps using the Nosé-Hoover thermostat and barostat (38). Periodic boundary condition is imposed along the axial direction (i.e., the loading direction <110>) of all simulated samples. The samples are first stretched to a strain of 1.8% at a constant strain rate of 10^8/s under NVT ensemble, and then relaxed for several nanoseconds under NVT ensemble while holding the strain fixed. In the relaxation process, I monitor the variation of the axial stress by averaging the Virial stresses (98) over all atoms in the samples. Note that I have used an elevated temperature of 800K in our MD simulations to accelerate the thermally activated processes of vacancy diffusion and the associated dislocation nucleation within the time scale of MD simulations. To examine the reversibility of deformation (related to the reverse motion of dislocations) and to measure the residual strain, I unload the elongated samples at a strain rate of 10^8/s until the axial stress in the simulated samples approaches zero. Subsequently, the samples are further relaxed at the equilibrium state while the axial stress is kept zero by a Nosé-Hoover barostat. The residual strain is calculated by comparing the initial and final lengths of the samples. Throughout the simulations, the temperature is kept constant at 800 K by the Nosé-Hoover thermostat. The loading and unloading processes are designed to mimic the real experimental testing apart from the use of much higher strain rates.

To identify defects during deformation of the samples, atoms were painted with different crystalline order in different colors using a common neighbor analysis. The green colored atoms stand for atoms with FCC symmetry, the red ones those with HCP symmetry, and the grey ones those at dislocation cores, surfaces and point defects.

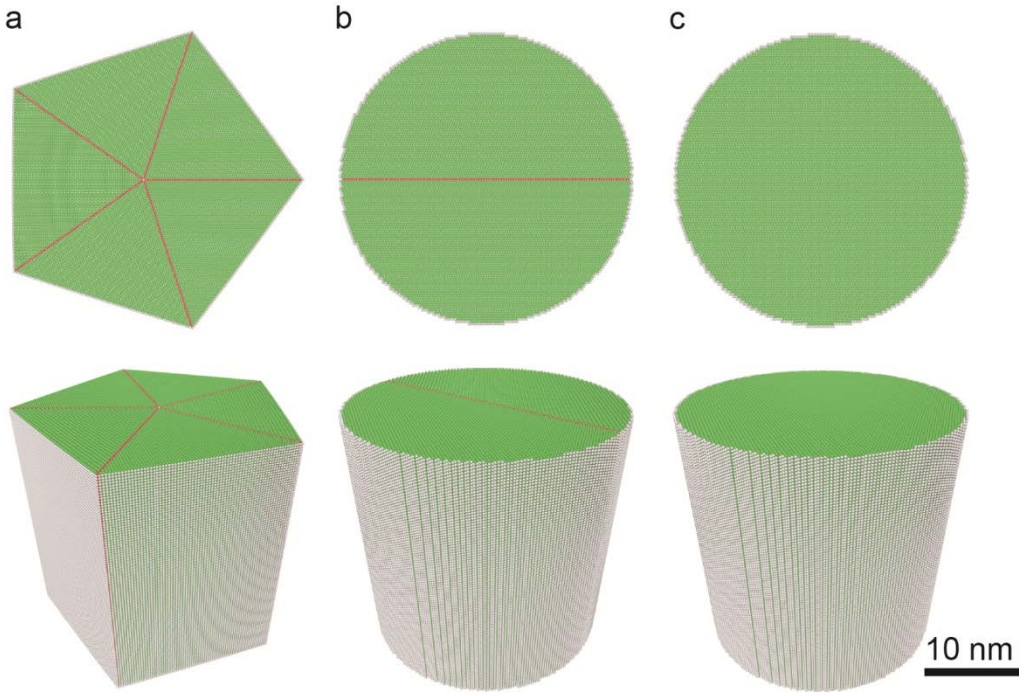

Figure 3.4 | Atomic configurations of three kinds of NW samples. a, penta-twinned, **b**, mono-twinned bi-crystalline, and **c**, single-crystalline NWs. The upper parts are viewed from NWs axis and the lower parts are side views of NWs.

3.3.2. Stress relaxation in penta-twinned NWs

It is known that stress relaxation is highly sensitive to the microstructures, particularly point defects (78, 99, 100). Therefore, I introduced a population of vacancies with concentration from 0% to 2% in the simulated samples to facilitate dislocation nucleation. To investigate stress relaxation behavior, I first stretched the simulated samples to a strain of 1.8%, and then monitored stress relaxation while the applied strain

was held fixed. The simulation results showed no stress relaxation during a simulation time period over tens of nanoseconds in a vacancy-free NW. However, with 1% vacancies introduced as initial defects in the penta-twinned NWs, the stress gradually decreased from an initial stress of 1.15 GPa by about 200 MPa (i.e., 17.4% of the initial stress) in 2 ns, as illustrated in Fig. 3.5a. The insets in Fig. 3.5a capture a sequence of partial dislocation nucleation events in the TB-separated nanograins. The partial dislocation nucleation events exhibit a one-to-one correspondence with discrete stress drops in the stress relaxation profile shown in Fig. 3.5a, indicating that the stress relaxation is a direct consequence of dislocation nucleation in the penta-twinned nanostructure.

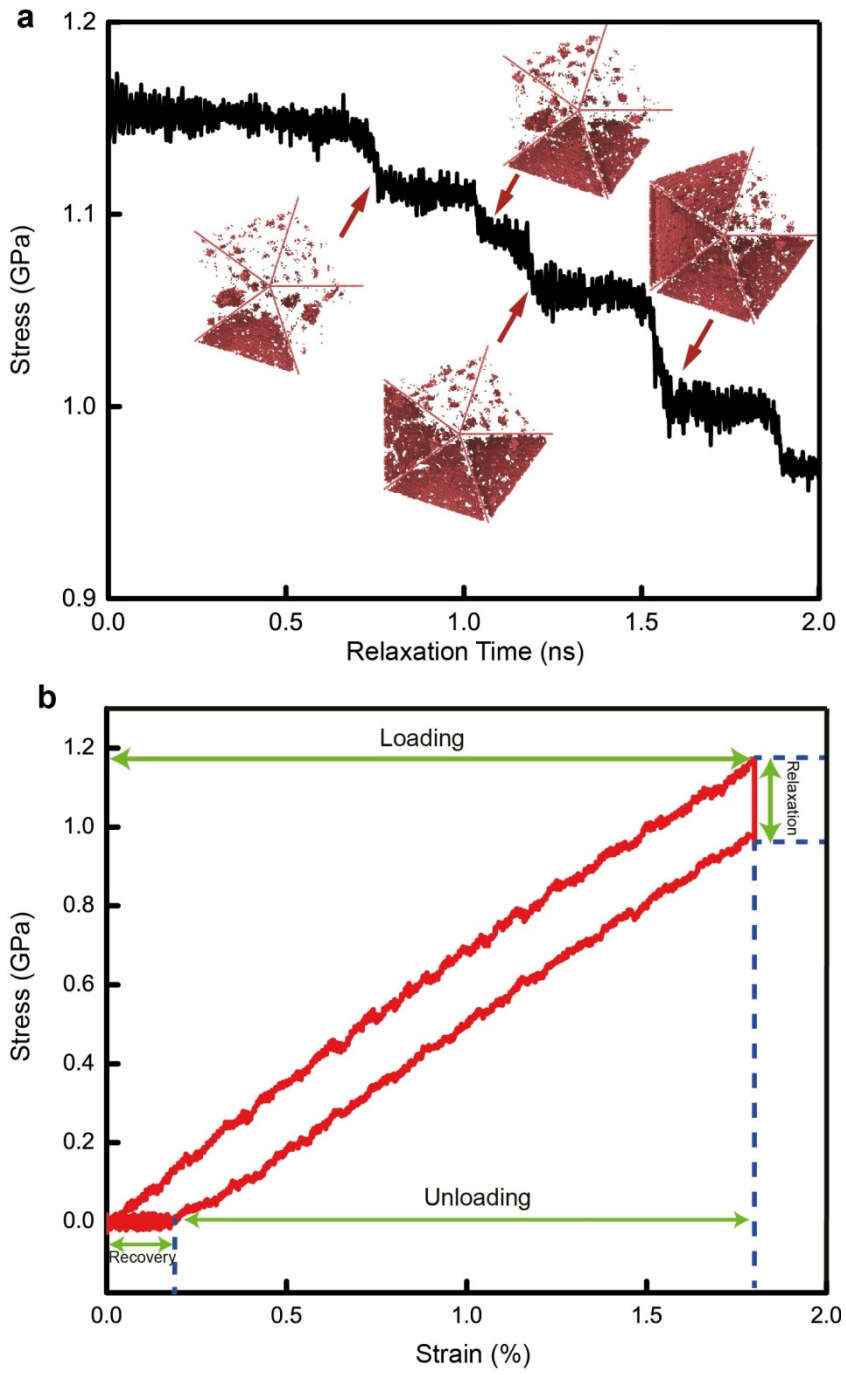

Figure 3.5 | Reversible plasticity in simulations. **a**, Stress relaxation of a 30 nm-diameter penta-twinned Ag nanowire. Each stress drop corresponds to a discrete event of dislocation nucleation shown in insets (i), (ii) and (iii). **b**, The stress-strain curve.

3.3.3. Strain recovery in penta-twinned NWs

Similar to experiments, after stress relaxation, the simulated samples were unloaded to a stress-free state. When the applied stress came down to zero, there was still a 0.21 % of strain remaining in the sample, as shown in Fig. 3.5b. Continuing relaxation of the sample under zero stress resulted in complete recovery of the residue strain after 0.3 ns (see Fig. 3.6a). This phenomenon is very similar to the experimental observations. Figure 3.6b-c illustrates two snapshots of the deformed sample during relaxation and recovery, respectively. During stress relaxation, partial dislocation loops were found to nucleate spontaneously from free surface and then expand through the grain interiors separated by the five TBs. Each discrete dislocation nucleation event leads to a visible stress drop in our simulation. During stress relaxation, it was observed that several dislocation loops moved and leaned against TBs as the stress level went down, and some dislocation segments were absorbed by, while others stayed close to, the TBs. During subsequent strain recovery after unloading, partial dislocation loops were seen to retract from the five-fold TBs under zero applied stress, resulting in complete strain recovery. It is known that there exists a repulsive force between TB and curved dislocation loop (11, 101). When the external stress is removed, the repulsive force from the TBs appears to induce reverse motion of dislocations by pushing the non-inserted segments as well as extracting the inserted segments from the TBs back toward where the dislocations were nucleated. Moreover, we have analyzed the Peach-Koehler force exerted on the partial dislocations by the inhomogeneous intrinsic stress field of the five-fold twin and found that it will also act as a driving force for dislocation retraction during strain recovery (see discussion in **3.3.4**).

Previous studies (84-88) showed that plastic strain recovery in thin films can be attributed to dislocation- and GB-mediated processes. In penta-twinned NWs, there are no regular GBs and the TBs have low energy, high symmetry, coherent atomic structure, and one side geometrically constrained in the center of the NWs. In this nanostructure, the sliding and diffusion processes should be suppressed to a large extent. Therefore, the controlling mechanism for the observed strain recovery behavior can only be attributed to TB-dislocation interactions. The five-fold TBs separate the NW into five nanograins which confine the length of dislocation segments as well as the mean free path of vacancy diffusion. More importantly, TBs are effective obstacles for dislocations and produce a repulsive force to drive the reverse motion of dislocations during unloading. In addition to these effects, the inhomogeneous stress field generated by the five-fold twin may also benefit vacancy diffusion and reversible dislocation motion.

To further demonstrate the unique role of TBs in the recovery behavior of NWs, I performed two additional simulations for a single-crystalline NW and a bi-crystalline NW with a single TB in the middle – a mono-twinned NW. To facilitate dislocation nucleation in simulation, these two samples have the same vacancy concentration of 1.0%. Repeating the simulations as before but relaxing the two NWs from an initial strain of 2.0%, I can observed nearly full plastic strain recovery in the mono-twinned NW, but not in the single-crystalline NW, as illustrated in Fig. 3.6a. In the mono-twinned NW, the TB can effectively blocks the motion of leading partials, preventing them from escaping out of the sample (see Fig. 3.6c), allowing them to retract back from the TB under the residual internal stress field upon unloading, leading to plastic strain recovery. In contrast, in the single-crystalline NW, dislocations nucleated from the free surface,

travelled across the NW and eventually escaped out of the sample, leaving a permanent surface step. In this case, the dislocation motion, and the associated deformation, becomes irreversible during subsequent unloading.

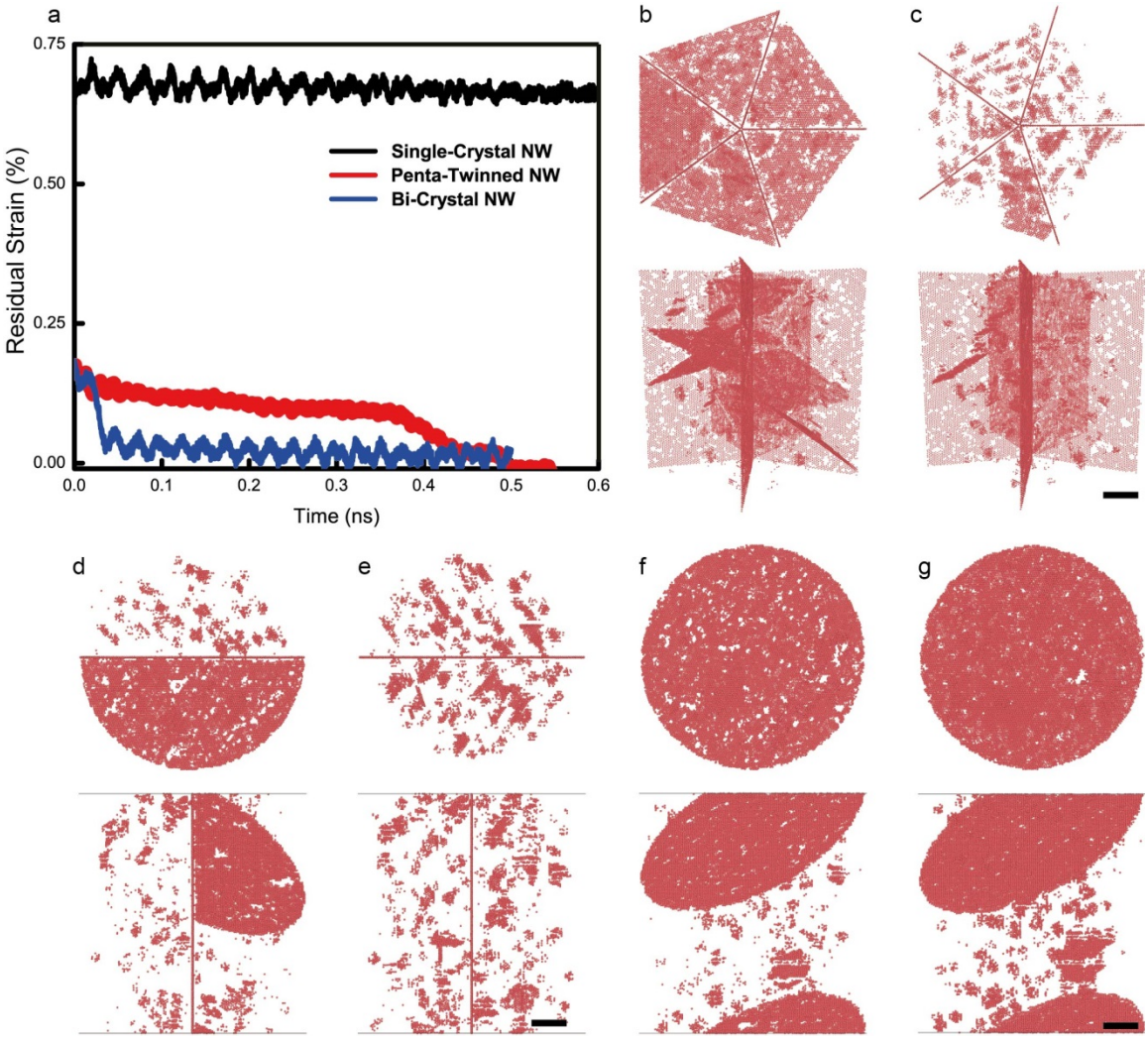

Figure 3.6 | Fully recoverable plasticity and associated dislocation activities in NWs. **a**, Time-dependent strain recovery due to the reverse motion of partial dislocations. **b-c**, Penta-twinned nanowire; **b**, during relaxation, dislocations are nucleated and confined by the penta-twinned nanostructure; **c**, dislocations retract and disappear during recovery. **d-e**, Bi-crystalline nanowire; **d**, during relaxation, a dislocation is impeded by the twin

boundary; **e**, the dislocation retracts and disappears during recovery. **f-g**, Single-crystalline nanowire; **f**, during relaxation, dislocations travel through the sample interior and escapes out of the free surface, leaving behind a permanent stacking fault; **g**, after unloading, the stacking fault still resides in the sample interior, resulting in permanent plastic deformation. Only HCP atoms are visible in (**b-g**) for clarity, upper parts are viewed from NW axis and lower parts are side view of NWs. Scale bar, 5nm.

The MD simulations reveal that the controlling mechanism for the observed stress relaxation and strain recovery behavior is TB-dislocation interactions. The *in-situ* TEM testing further confirmed that the stress relaxation and strain recovery in a penta-twinned Ag NW are accompanied by nucleation and annihilation of dislocations, respectively, as shown in Fig. 3.7a-d. Before the relaxation step (Fig. 3.7a), there were no dislocations in the NW as the strain increased to 1.6 %. At the relaxation step, a dislocation network appeared in < 5 min. The dislocations were terminated at the TBs (Fig. 3.7b). During the unloading step, the applied load gradually decreased to zero but the dislocations remained (Fig. 3.7c). In the recovery step, the dislocation network gradually retracted and suddenly disappeared after ~8 min (Fig. 3.7d). After 15 min, the NW was totally recovered.

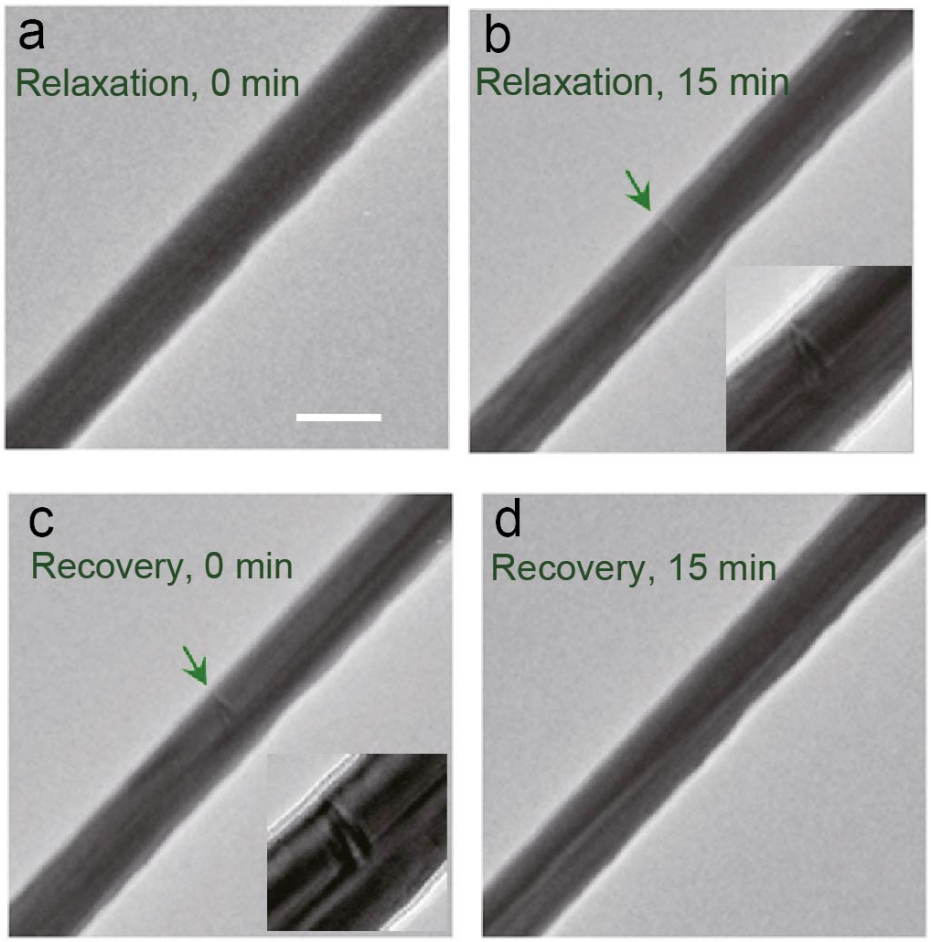

Figure 3.7 | *In-situ* observation of dislocation activities during fully recoverable plasticity in NWs. a-d, *In-situ* TEM observations of dislocation nucleation and annihilation in a penta-twinned Ag NW (85 nm in diameter). The arrows in **b** and **c** point to the dislocation networks with high-mag images shown in the insets. Scale bar, 150nm. (Courtesy of Prof. Yong Zhu and Dr.Guangming Chen)

Plastic deformation in metals generally consists of two components: an athermal part and a thermal part. The former, driven by the long-range internal stress, has weak temperature dependence, while the latter accounts for thermally activated processes that are usually sensitive to both temperature and strain rate. In our experiments and simulations reported above, the nanowires did not reach the athermal yield point during

loading. It was during the relaxation step that the thermally activated nucleation of partial dislocations was observed.

To investigate whether the phenomenon of recoverable plasticity also occurs for similar samples beyond the athermal plastic yield point, I have performed additional MD simulations to investigate the loading-unloading behavior of the penta-twinned Ag NWs under much larger strains. The NWs were loaded beyond the athermal yielding point such that partial dislocations are nucleated even without the relaxation step. In the first simulation, the sample was loaded to 4.5% strain, which is only slightly beyond the athermal yielding point (Fig. 3.8). In this case, a number of partial dislocations were nucleated during loading and then retracted back to their original nucleation sites during unloading, still resulting in full plastic strain recovery. During this process, no complex dislocations reactions occur within the grains. In the second simulation, the sample was loaded to about 10% strain, corresponding to very large plastic deformation before unloading (Fig. 3.9). There was only about 1% strain recovered during unloading. In this case, the applied stress was large enough to allow multiple slip systems to be activated, leading to reactions and entanglement between dislocations from different slip systems. As a result, more complex and disordered dislocation structures prevented full strain recovery and only 1% strain was observed to recover, reminiscent of the classical Bauschinger's effect.

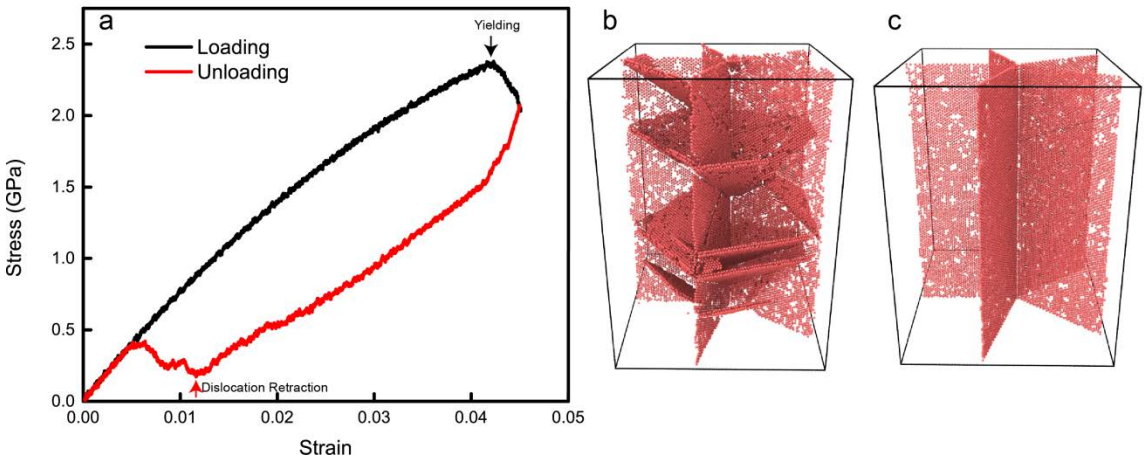

Figure 3.8 | MD simulations of a penta-twinned nanowire loaded slightly beyond the athermal yielding point, and then unloaded. a, Stress strain curve of loading and unloading of penta-twinned NW. **b,** Partials nucleation and stacking faults in NW before unloading. **c,** After unloading, all the partials retracted back to free surface. Only HCP atoms are shown.

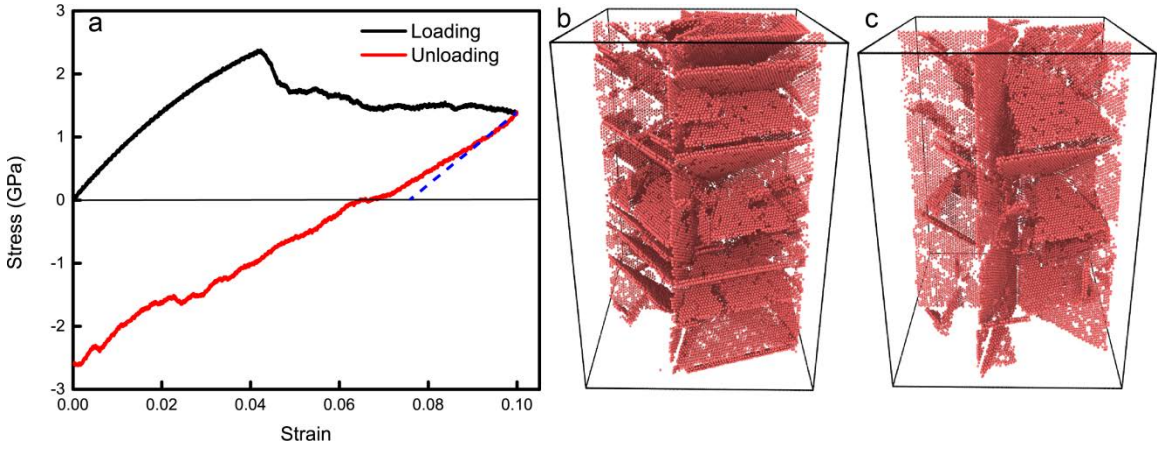

Figure 3.9 | MD simulations of a penta-twinned nanowire loaded to 10% strain and then unloaded. a, Stress strain curve of loading and unloading of penta-twinned NW. **b,** Partials nucleation and stacking faults in NW before unloading. **c,** After unloading, dislocation left in the NW. Only HCP atoms are shown.

3.3.4. Intrinsic residual stress field of penta-twin

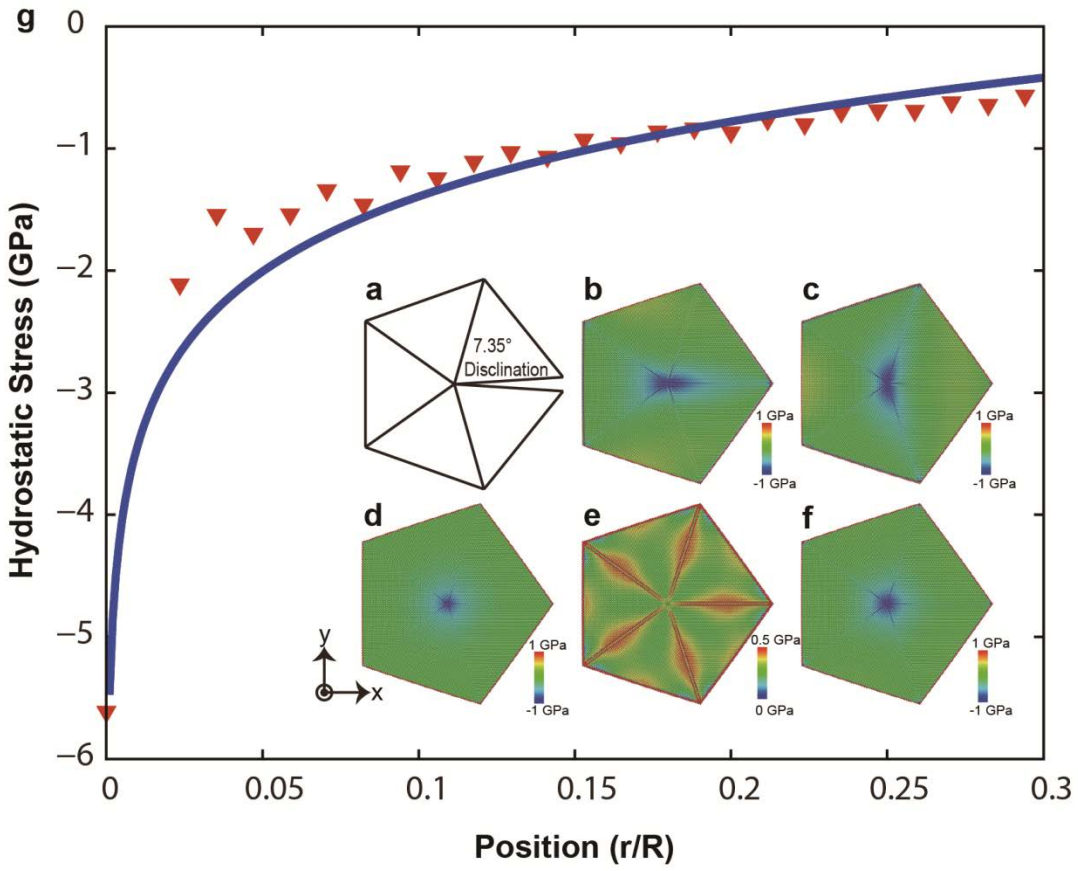

Figure 3.10 | Intrinsic stress field in the penta-twinned nanostructure. a, Sketch of the disclination for the penta-twinned structure. **b-f**, Contours of normal (σ_{xx}, σ_{yy} and σ_{zz}), von Mises and hydrostatic stresses from atomistic simulations, respectively. **g**, Hydrostatic stress as a function of r/R, r being the radial distance and R the radius of NW. The blue solid curve represents the exact solution from disclination theory, while the red triangles are the results from atomistic simulation.

In FCC structures, the angle between adjacent {111} planes is 70.53º. The penta-twin structure can be regarded as a disclination with an angular deficiency of 7.35º (as shown in Fig. 3.10a). Such a structure can create an intrinsic stress field due to the angular

elastic misfit (102). Fig. 3.10b-f show the internal normal stresses (σ_{xx}, σ_{yy} and σ_{zz}), von Mises stress and hydrostatic stress contours of a penta-twin from atomistic simulations at a constant temperature of 1.5 K, respectively. The highest tensile stress occurs at the free surface, while the lowest compressive stress occurs at the core. The von Mises stress exhibits a quinquefoliate-like distribution, with local maximum on twin boundaries and local minimum at the bisecting line of two neighboring boundaries. Such stress distribution is thought to be the origin of pronounced stiffening of smaller penta-twinned NWs(102). In the region close to the core of the five-fold twin, the hydrostatic stress distribution at the atomic scale is in good agreement with theoretical predictions from the continuum disclination theory (103), as demonstrated in Fig. 3.10g. Notably, the intrinsic stress field caused by the penta-twin is significantly inhomogeneous, and thus could serve as a driving force to the reverse motion of dislocations responsible for strain recovery.

Figure 3.11 shows a Shockley partial dislocation in one of the penta-twinned NW grains. I calculate the Peach-Koehler force exerted on the partial dislocation segment by the intrinsic stress field of the penta-twin. As illustrated in the Fig. 3.11c, the Burgers vector of the Shockley partial is 1/6[11-2], and its edge segment is in [1-10] direction while its screw segment in [11-2] direction. According to the disclination theory(103), the intrinsic stress field of a penta-twin in a cylindrical NW can be expressed in Cartesian coordinates (x,y,z) shown in Fig. 3.11 as

$$\sigma_{xx} = \frac{G\omega}{2\pi(1-\nu)}\left(\frac{1}{2}\ln\frac{x^2+y^2}{R^2}+\frac{y^2}{x^2+y^2}\right)$$
$$\sigma_{yy} = \frac{G\omega}{2\pi(1-\nu)}\left(\frac{1}{2}\ln\frac{x^2+y^2}{R^2}+\frac{x^2}{x^2+y^2}\right) \quad (3.1)$$
$$\sigma_{xy} = -\frac{G\omega}{2\pi(1-\nu)}\frac{xy}{x^2+y^2}$$
$$\sigma_{zz} = \frac{G\omega\nu}{2\pi(1-\nu)}\left(\ln\frac{x^2+y^2}{R^2}+1\right)$$

where R is the radius of the NW, ω the disclination angle, G the shear modulus, and ν Poisson's ratio. The Peach-Koehler force **F** acting on a dislocation segment with Burges vector of **b** and line vector of **ξ** by the stress field **σ** of a wedge disclination is expressed as

$$\mathbf{F} = \boldsymbol{\xi}\times(\boldsymbol{\sigma}\bullet\mathbf{b}) \quad (3.2)$$

The Peach-Koehler force is projected in the direction of the Burgers vector ***b*** and the y direction:

$$F_b = \left[\boldsymbol{\xi}\times(\boldsymbol{\sigma}\bullet\mathbf{b})\right]\bullet\mathbf{b}$$
$$F_y = \left[\boldsymbol{\xi}\times(\boldsymbol{\sigma}\bullet\mathbf{b})\right]\bullet\vec{e}_y \quad (3.3)$$

Substituting stress field into the above equation and we obtain,

$$F_b = \frac{\sqrt{2}}{18}\xi_y(\sigma_{xx}-\sigma_{zz}) - \frac{1}{18}(2\xi_z+\sqrt{2}\xi_x)\sigma_{xy}$$

$$F_y = -\frac{1}{3}\xi_z\sigma_{xx} - \frac{\sqrt{2}}{6}\xi_x\sigma_{zz}$$

Note that ν=0.37 for silver and $\left|\frac{y}{x}\right| < \tan(\frac{70.53^\circ}{2})$ in the grain shown in Fig. 3.11a. We obtain,

$$\sigma_{xx}-\sigma_{zz}=\frac{G\omega}{2\pi(1-\nu)}\left(\frac{1}{2}\ln\frac{x^2+y^2}{R^2}+\frac{y^2}{x^2+y^2}-\nu\ln\frac{x^2+y^2}{R^2}-\nu\right)$$
$$=\frac{G\omega}{2\pi(1-\nu)}\left(0.13\ln\frac{x^2+y^2}{R^2}-0.04\right)<0$$

If the dislocation segment has an edge character, i.e. $\boldsymbol{\xi}$ is normal to $\boldsymbol{b}$, $\boldsymbol{\xi}$ =1/2[1-10], then

$$F_b=\frac{\sqrt{2}}{18}(\sigma_{xx}-\sigma_{zz})<0$$

$$F_y=0$$

If the dislocation segment has a screw character, i.e. $\boldsymbol{\xi}$ is parallel to $\boldsymbol{b}$, or $\boldsymbol{\xi}=\boldsymbol{b}$, then

$$F_b=0$$

$$F_y=\frac{\sqrt{2}}{18}(\sigma_{zz}-\sigma_{xx})>0$$

In both cases, the Peach-Koehler force exerted on the dislocation by the five-fold twin is repulsive, indicating that the intrinsic stress field favors dislocation retraction.

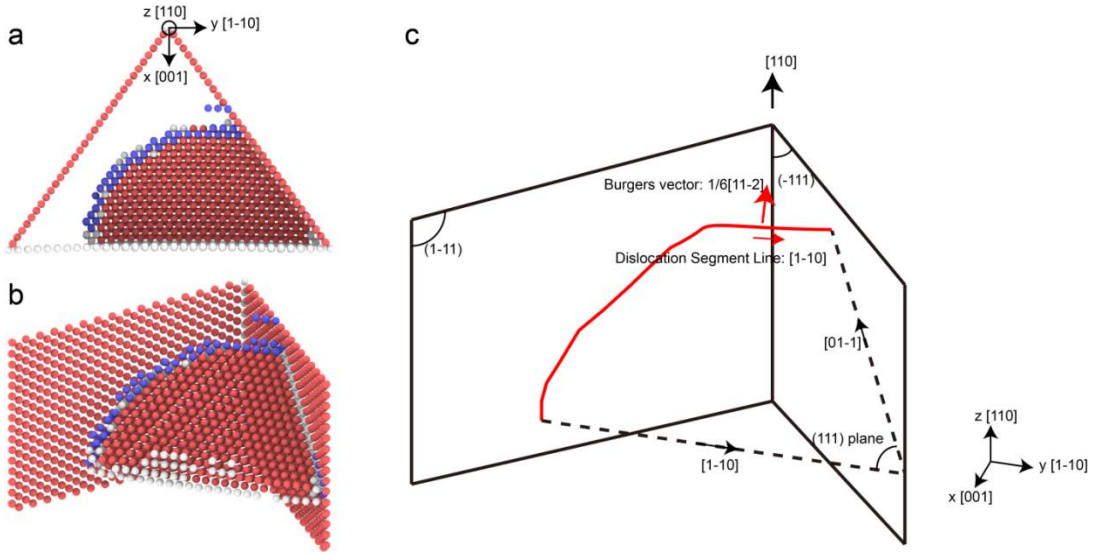

Figure 3.11 | Nucleation and propagation of a Shockley partial dislocation in one grain of the penta-twinned nanowire. a-b, Atomic structures of the partial dislocation. **c**, Schematic illustration of the dislocation gliding on its slip plane.

3.3.5. Tilting and mixed-type grain boundaries instead of twin boundary

I have shown that TBs are effective obstacles for dislocations and produce a repulsive force to drive the reverse motion of dislocations during unloading. How about other kinds of boundaries? Can they also block the glide of partial dislocations? Will a similar recoverable mechanism work in other types of structure? In this part, I have also investigated bi-crystalline NWs with different types of regular GBs (such as low-angle/high-angle tilt GBs and mixed GB).

I selected a tilt GB with mis-orientation of 7º, a tilt GB with mis-orientation of 45º and a tilt-twist mixed GB to repeat the atomistic simulations of relaxation. In the case of the low-angle tilt GB, partial dislocation nucleated from the surface can easily transverse through the GB during relaxation, as shown in Fig. 3.12a. Such low-angle tilt GB cannot impede dislocation slip, because it consists of a sparse array of edge dislocations. During

unloading, a dislocation cannot move backwards because it has escaped out of the sample from free surface. As a result, the stacking fault remains in the sample and no strain recovery is observed in this case. For the high-angle tilt GB, dislocations are sufficiently blocked by the GB and firmly trapped in it (Fig. 3.12b). However, in this case, dislocations are locked to the GB and cannot retract back upon unloading, leading to irreversible plastic deformation. The same phenomenon was observed in the case of the tilt-twist mixed GB (Fig. 3.12c). In summary, tt is found that the tilt and tilt-twist mixed GBs either failed to block the dislocation or trapped the dislocation upon unloading, resulting in no strain recovery (Fig 3.12). These studies further demonstrate that the TBs play an essential role in the reverse motion of partial dislocations, which leads to the observed plastic strain recovery in the penta-twinned Ag NWs. It is noted that in penta-twinned NWs, five-fold TBs divide the NW interior into five nanograins, which can prevent the escape of dislocations from free surfaces and facilitate dislocation retraction more effectively compared to a single TB in bi-crystalline NWs. In addition, the intrinsic residual stress field induced by the fivefold twin also favors dislocation retraction upon unloading.

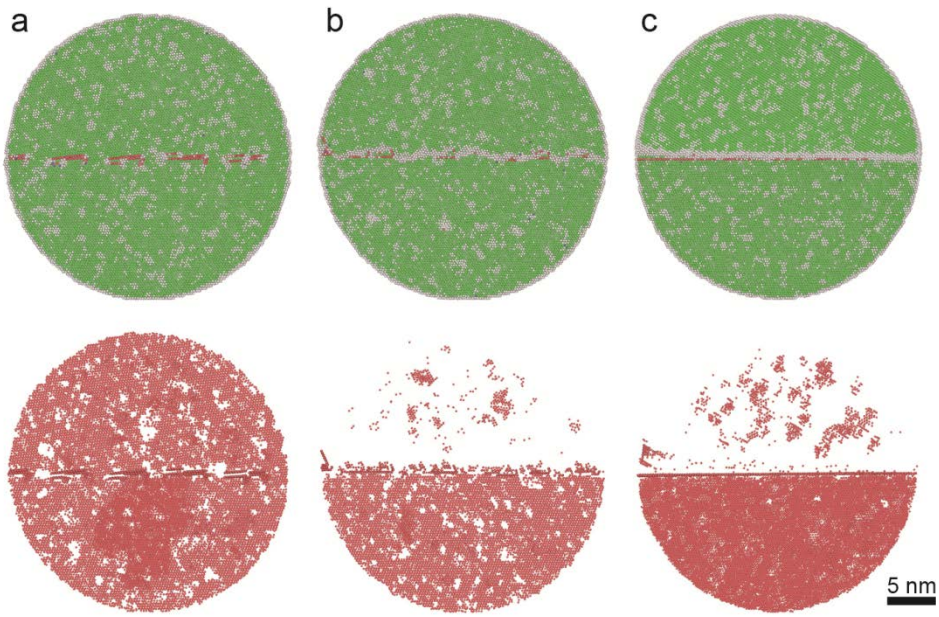

Figure 3.12 | Cross-sectional view of bi-crystalline NWs with different types of grain boundaries before and after relaxation. The upper Figs show the cross-section atomic configurations of NWs before relaxation, and the lower ones display their configurations after relaxation (only HCP atoms are shown). **a**, In the case of a low angle 7º tilt grain boundary, dislocations can easily traverse through the grain boundary and escape out of the sample, leaving behind stacking faults in the NW. **b**, In the case of a 45º tilt grain boundary, dislocations are blocked by the grain boundary but they fail to retract upon unloading. **c**, In the case of a tilt-twist mixed grain boundary, dislocations are also impeded by the grain boundary, but they also fail to retract upon unloading. In all these cases, no strain recovery is observed.

3.4. Summary

In this chapter, I have discovered an unusual dislocation-based stress relaxation and strain recovery behaviour in penta-twinned Ag NWs large-scale MD simulations. This behavior consists of two facets: stress relaxation under an applied strain and complete plastic strain recovery upon unloading. Our studies indicate that stress relaxation

originates from the nucleation of leading partial dislocations assisted by vacancy diffusion, while the complete strain recovery is due to the reverse motion of partial dislocations driven by the repulsive force from the TBs and the intrinsic stress field due to the five-fold twin. The simulations demonstrate that the TBs play a crucial role in the observed phenomenon in penta-twinned NWs, as bi-crystalline NWs with a single TB exhibit a similar behavior while single-crystalline NWs or NWs with other types GBs do not. It is noted that diffusion and sliding processes associated with GBs should be suppressed in penta-twinned NWs. Therefore, in contrast to previous studies in nanocrystalline metals due to a cooperation of dislocation- and GB- mediated processes; the present study demonstrates a new type of stress relaxation and full plastic strain recovery induced by TB-dislocation interactions. Our study opens up a promising prospect of designing one-dimensional nanostructures with time-dependent strain recovery capabilities.

Chapter 4 Tensile-Detwinning and Superplasticity in Bi-twinned Metallic Nanowires

The work described in this Chapter is in collaboration with Prof. Yong Zhu's group, of which Dr. Guangming Chen and Tzu-Hsuan Chang performed the *in situ* experiments.

4.1. Introduction

Recently, there has been intensive study on the mechanical behavior of metallic nanowires (NWs) focusing on surface effects (67-73). However, fundamental understanding of the relationship between microstructure and deformation mechanisms in NWs is still lacking. The bi-twinned nanowires (NWs) used in this work were synthesized by physical vapor deposition (32), a well-known method for synthesis of single-crystalline metallic NWs. However, based on a thorough microstructure characterization, Prof.Yong Zhu's group found that the bi-twinned NWs occupy 81% and the single-crystalline NWs only 19% of the total 113 NWs examined (Fig. 4.1). Mechanical behavior of bi-twinned NWs has not been investigated, to the best of our knowledge; in contrast, that of single-crystalline NWs has been studied in several recent reports (32, 68, 104, 105). The novel bi-twinned structure leads to interesting mechanical properties and very different deformation modes based on its geometry.

In this chapter, based on *in situ* TEM tensile tests observations, I investigate the deformation mechanisms in the so-called bi-twinned metallic NWs by molecular dynamics (MD) simulations. In addition to localized dislocation slip, a detwinning

induced superplasticity (failure strain more than 30%) mode was observed. The two deformation modes were found to depend on the volume ratio between the two twin variants and the cross-sectional aspect ratio. Specifically, in bi-twinned NWs with balanced volume ratios, localized dislocation slip across the TB leads to permanent slip and limited ductility, while in those with small volume ratios a novel two-step detwinning mechanism dominates, leading to superplastic deformation. The detwinning process is unexpected as there is no resolved shear stress on the TB, the unique detwinning process is attributed to multiple dislocation interactions with the TB that can alter the local atomic arrangement and form a unique TB-GB-TB structure. An energy-based criterion on the transition of the two deformation modes is proposed. Single crystalline Ag NWs were studied for the purpose of comparison, which also exhibited pronounced superplasticity.

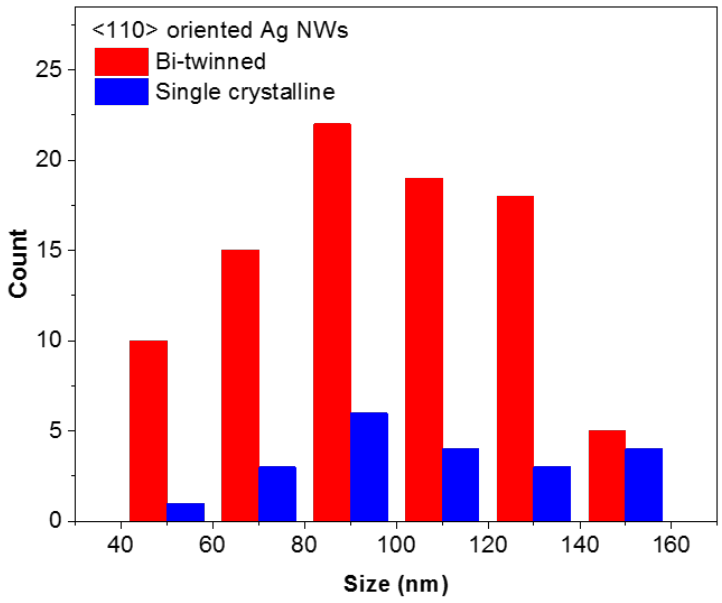

Figure 4.1 | Distribution of bi-twinned and single crystalline NWs in the examined 113 NWs. "Size" used here referred to the NW width directly measured from the TEM images. (Courtesy of Prof. Yong Zhu and Dr.Guangming Chen)

4.2. Experimental studies

4.2.1. NW morphology and *in situ* TEM tensile testing

The Ag NWs in this study exhibited high crystalline quality owing to near-equilibrium growth conditions. Based on TEM characterization, there are two types of Ag NWs with growth direction along a <110> direction, those that are bi-twinned and others that are single-crystalline, as shown in Fig. 4.2. Figure 4.2a-b show schematic drawings of the morphology of the bi-twinned and single crystalline NWs, respectively. The corresponding cross-sectional TEM images of the two types of NWs are shown in Fig. 4.2c-d. Both show hexagonal cross-sectional shapes but with different arrangement of surface facets (marked in Fig. 4.2a-b). The high-resolution scanning TEM (STEM) image in Fig. 4.2e shows that the internal TB in a bi-twinned NW is coherent without other line or planar defects as in the case of penta-twinned metallic NWs (106). From our comparison of the mechanical properties between single crystalline, bi-twinned and penta-twinned NWs (Table 1), the bi-twinned NWs offer a good combination of mechanical properties, with higher yield strength and good ductility.

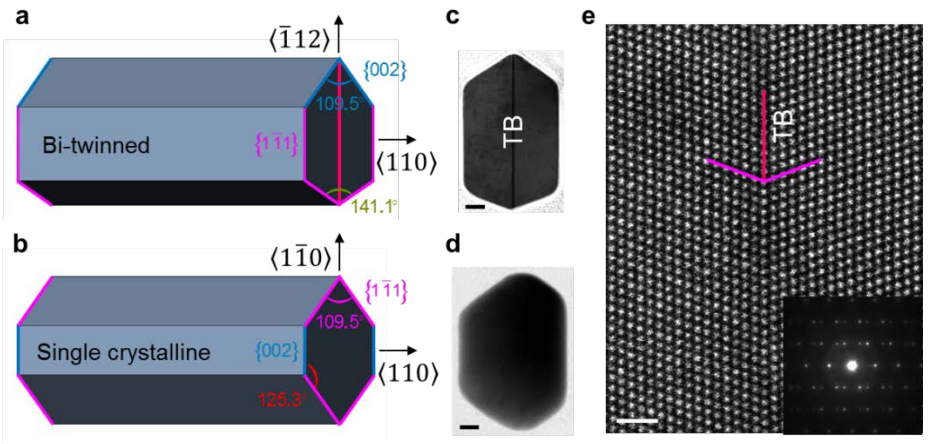

Figure 4.2 | Characterization of crystalline Ag NWs. a,b, Schematic drawings of bi-twinned and single crystalline NWs, respectively. **c,d**, Cross-sectional TEM images of bi-twinned and single crystalline NWs, respectively. Scale bar, 20 nm. **e**, A cross-sectional high-resolution STEM image of a bi-twinned Ag NW. Inset in **e** is the corresponding SAED pattern. Scale bar, 1 nm. (Courtesy of Prof. Yong Zhu and Dr.Guangming Chen)

Table 1 | Mechanical properties of single crystalline, bi- and penta-twinned Ag NWs under uniaxial tensile testing. Note that all three types of NWs have similar cross-sectional areas corresponding to a diameter ranging from 95-120 nm (treated as round shape) so as to avoid the size dependent effect on the Young's modulus.

	Single crystalline	Bi-twinned	Penta-twinned
Young's Modulus (GPa)	82±2.2		
Yield Strength (GPa)	0.8-1.0	1.2-1.4	0.8-1.1
Ultimate Strength (GPa)	1.0-1.2	1.5-1.8	1.1-1.5
Total Elongation (%)	35-41	3.5-34.5	1.9-3.8
Number of tested NWs	5	17	13

4.2.2. *In-situ* tensile Deformation and failure modes

In-situ TEM tensile testing of individual NWs were performed using a microelectromechanical system (MEMS) based tensile testing stage that allows accurate measurements of both load and displacement simultaneously, as well as real-time imaging of microstructure evolution during deformation (107, 108). Figure 4.3 shows stress-strain responses and snapshots of microstructure evolution for typical tensile tests of two bi-twinned and one single crystalline Ag NWs. Insets in Fig. 4.3a-c are the corresponding cross-sectional TEM images of the tested NWs, taken from the undeformed parts (beyond the clamps). The two bi-twinned NWs, as shown in the insets of Fig. 4.3a-b, possess different volume ratios (V_{small}/V_{large}) between the two twin variants, 0.64 and 0.19, respectively.

The bi-twinned NW with a balanced (or large) volume ratio exhibited a limited fracture strain (3.5%, Fig. 4.3a,d), while the other with a small volume ratio showed superplasticity (109) (an elongation of 34.5% measured between the two deposited local markers, Fig. 4.3b,e), comparable to the superplasticity in the single crystalline NW (an elongation of 37.5% for the fully deformed part between the two local markers, Fig. 4.3c,f). Moreover, the yield strength and the ultimate tensile strength (UTS) of the bi-twinned Ag NWs, regardless of the deformation mode, were found to be 1.21-1.38 and 1.47-1.54 GPa, respectively, which are higher than those of the single crystalline NWs (0.95 GPa and 1.21 GPa).

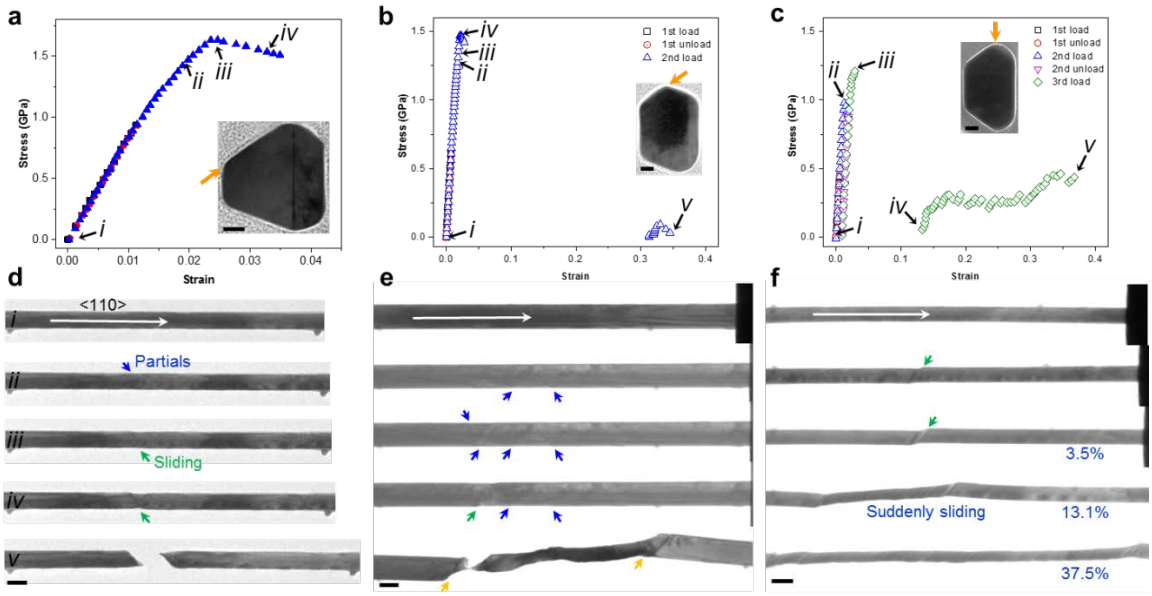

Figure 4.3 | Mechanical behaviors and microstructure evolutions of crystalline Ag NWs under *in situ* TEM tensile tests. a-c, Engineering stress-strain curves of a bi-twinned Ag NW with balanced volume ratio, a bi-twinned Ag NW with small volume ratio and a single crystalline Ag NW, respectively. Insets in **a-c** are the corresponding cross-sectional images of the tested NWs (each sectioned from the undeformed part after the test). Scale bar, 20 nm. **d-f**, Snapshots of microstructure evolutions corresponding to **a-c**, respectively. The five snapshots in each case correspond to the stresses and strains marked in **a-c**. Partial dislocations are marked by blue arrows and planar sliding by green arrows. The viewing directions are from the $\langle 1\bar{1}0 \rangle$ zone axis of the small twin variant in **d**, the large twin variant in **e** and the whole grain in **f,** , which are marked by the yellow arrows in the insets in **a-c**, respectively. The new inclined TBs in **e** are marked by yellow arrows. All scale bars in **d-f**, 100 nm. (Courtesy of Prof. Yong Zhu and Dr.Guangming Chen)

For the purpose of comparison, *in situ* tensile testing of single crystalline Ag NWs was also performed, as shown in Fig. 4.3c,f. Twinning deformation leading to superplasticity was observed. The microstructure evolution in a single crystalline Ag NW during the plastic deformation is illustrated in Fig. 4.3f. At the yielding point, leading partials were

nucleated from the NW free surface and propagated across the NW cross section, which resulted in a permanent planar slip. Nucleation and propagation of the leading partials continued, followed by a sudden, large elongation of the NW accompanying a nearly full release of the applied stress. After that, the NW underwent a continuous twinning deformation with the increase of the applied load, leading to superplastic deformation. Twinning is a well-known deformation mechanism in single crystalline metallic NWs (68, 92, 110), and twinning-mediated superplasticity was observed in *in situ* SEM tensile testing of single crystalline Au NWs (111). However, a high density of defective structures (nanotwins and SFs) was observed in our case. Owing to the low SF energy of Ag, partial nucleation and twinning are almost equally likely to occur, as observed in our single crystalline Ag NWs.

4.3. Atomistic simulations

To further understand the deformation mechanism in bi-twinned metallic NWs, I have performed a series of MD simulations. The MD simulation results reveal a unique two-step tensile detwinning mechanism in bi-twinned NWs.

4.3.1. Simulation methodology

Large-scale MD simulations were performed using the software package LAMMPS (42). Simulation samples of bi-twinned NWs and single crystalline NWs were generated according to experimentally observed geometries. The inset in Fig. 4.11a shows the atomic cross-section of the bi-twinned NW samples. For each sample, W equals 13 nm and H ranges from 3 nm to 10 nm, and all samples are 80 nm in length. The embedded atom method potential for Ag(112) was used to describe the interatomic interactions.

Periodic boundary condition was imposed along the axial direction (that is, the loading direction <110>) of all simulated samples. The samples were initially relaxed and equilibrated at temperature of 300 K for 800 ps using the Nosé–Hoover (38) thermostat and barostat, followed by stretch at a constant strain rate of 10^8 s^{-1} under NVT ensemble (canonical ensemble) until failure. To visualize defects generated during deformation, atoms were painted with different crystalline order in different colors using a common neighbor analysis by OVITO (113). The green-colored atoms stand for atoms with face-centered cubic symmetry, the red ones those with hexagonal close-packed symmetry and the grey ones those at dislocation cores, surfaces and point defects.

4.3.2. Three different deformation modes in MD simulation

Three different deformation modes were observed in the *in-situ* tensile experiments for single crystalline and bi-twinned NWs as showed in Fig. 4.3. The bi-twinned Ag NWs with a balanced volume ratio shows localized dislocation nucleation and propagation with limited plastic strain at failure. However, large plasticity was observed in the bi-twinned Ag NWs with small volume ratios. Similar superplasticity was observed in all single crystalline <110> Ag NWs. Figure 4.4 shows stress strain curves of typical NWs deformation modes in MD simulations. The MD simulations match very well with the experimental results. In the following parts, I'll explore the detailed mechanism of deformation modes transition observed in MD simulations.

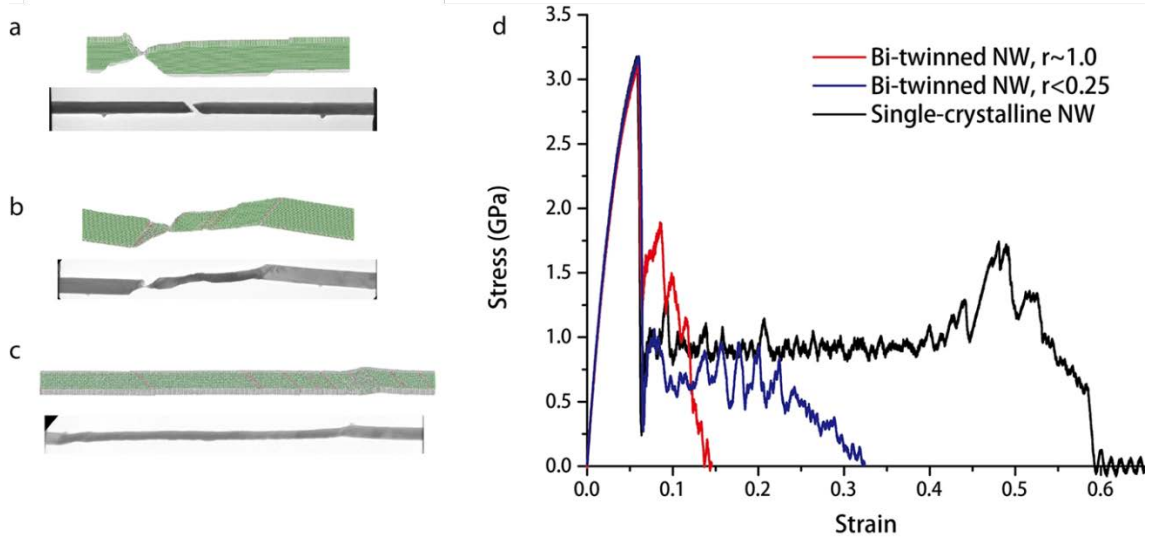

Figure 4.4 | Three deformation modes and corresponding stress-strain curves in MD simulations. a, A bi-twinned NW with volume ratio equal to 1, where localized slip dislocation was dominated with limited plasticity. **b**, A bi-twinned NW with volume ratio smaller than 0.25, where a tensile detwinning deformation mechanism was dominated leading to superplasticity. **c**, A single crystalline NW stretched in <110> direction, resulting in reorientation of the NW to <100> direction. In **a-c**, the corresponding deformation modes observed in experiments (TEM images) were also shown below the simulation Figs. **d**, Stress-strain curves of the corresponding three typical deformation modes in **a-c**.

4.3.3. Localized Slip in Bi-twinned NWs

Localized dislocation nucleation and propagation is dominant in bi-twinned Ag NWs with a balanced volume ratio, as was previously shown in Fig. 4.3d. Partial dislocations (identified by blue arrows in Fig. 4.3d) emerged upon yielding. After that, partial dislocations were continuously nucleated under increasing stress, leading to permanent plastic deformation (planar sliding) in the NW as they swept across the whole cross-sectional area. Continuous dislocation nucleation and propagation resulted in permanent

plastic deformation and failure of the NW. Note that only dislocation slip was observed without obvious necking at the fracture region, as seen in Fig. 4.3a. According to the MD simulation results in Fig. 4.5b and the schematic of the slip systems (114) shown in Fig. 4.5c, during localized slip, usually a partial dislocation, $\boldsymbol{\alpha B}$ from plane ***BCD*** (or $\boldsymbol{\beta A}$ from plane ***ACD***), nucleated from a surface vertex (Fig. 4.5b-i), propagates in the dominant twin variant towards the TB (Fig. 4.6b-ii), then interacts with the TB and transmits into the small twin variant (Fig. 4.6b-iii), leaving a stair-rod dislocation $\boldsymbol{\alpha\alpha'}$ with a magnitude of $\frac{2}{9}\langle 1\bar{1}1\rangle$ across the TB. After that, the trailing partial ($\boldsymbol{C\alpha}$ in plane ***BCD***) is nucleated (Fig. 4.5b-iv) and sweeps through the defective area, resulting in a slip step (one atomic layer along ***CB***) in the bi-twinned NW (Fig. 4.5b-vi). Figure 4.6 also shows the snapshots of surface dislocation nucleation and sweeping though the NW and leaving a surface step on the NW surface. When this single dislocation nucleation and propagation is dominant, surface steps will localize and NWs will fail at very limited plastic stain as showed in Fig. 4.5a, with the original TB remaining pristine. Dislocation activities in this deformation mode are isolated without reactions between multiple dislocations.

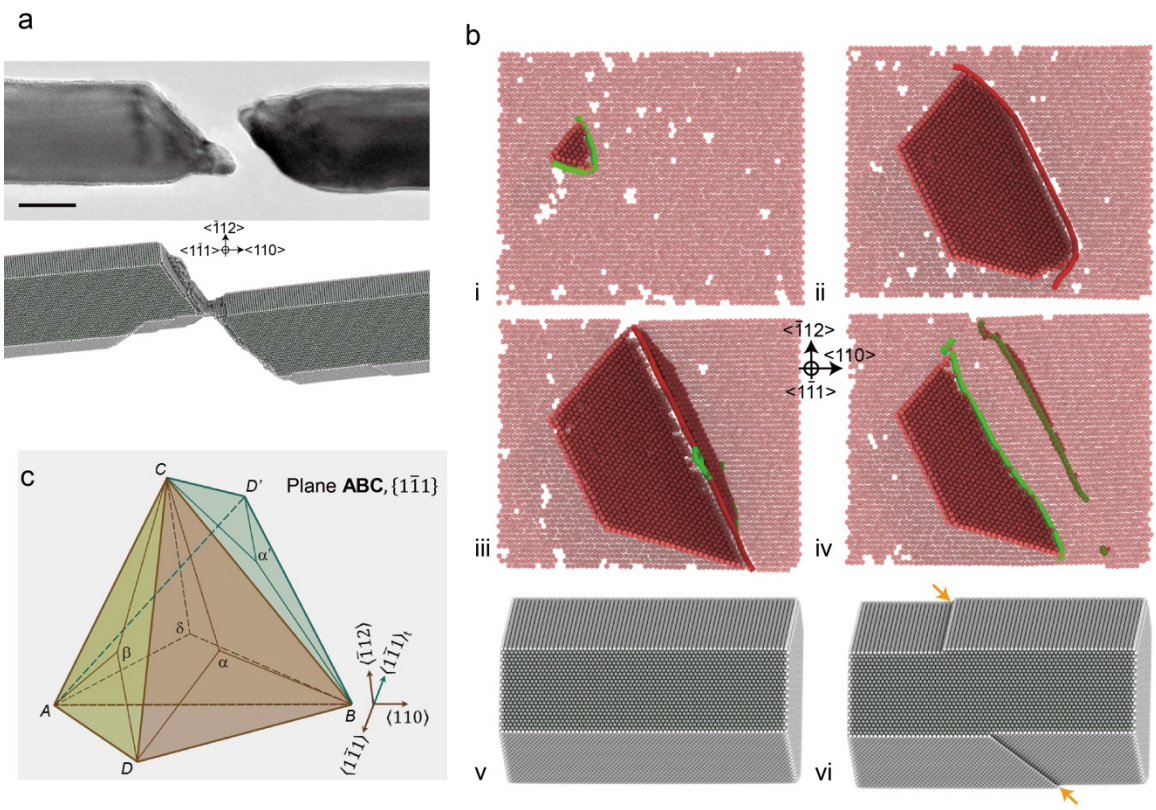

Figure 4.5 | Dislocation slip dominated deformation in bi-twinned Ag NWs with balanced volume ratio. a, Fracture morphology of the bi-twinned Ag NWs with balanced volume ratios from experiments and simulations, respectively. Scale bar 100 nm. **b,** Snapshots from MD simulations showing nucleation, propagation of partial dislocations and interaction between the partials and the TB. A permanent slipping step with one atomic layer is marked by a yellow arrow in **b**-vi. **c**, Illustration of a double Thompson tetrahedron on the coherent {1$\bar{1}$1} TB in bi-twinned NWs. The front tetrahedron (in the front of the TB) represents the matrix slip systems in the dominant twin variant, while the back one represents twin slip systems in the small twin variant.

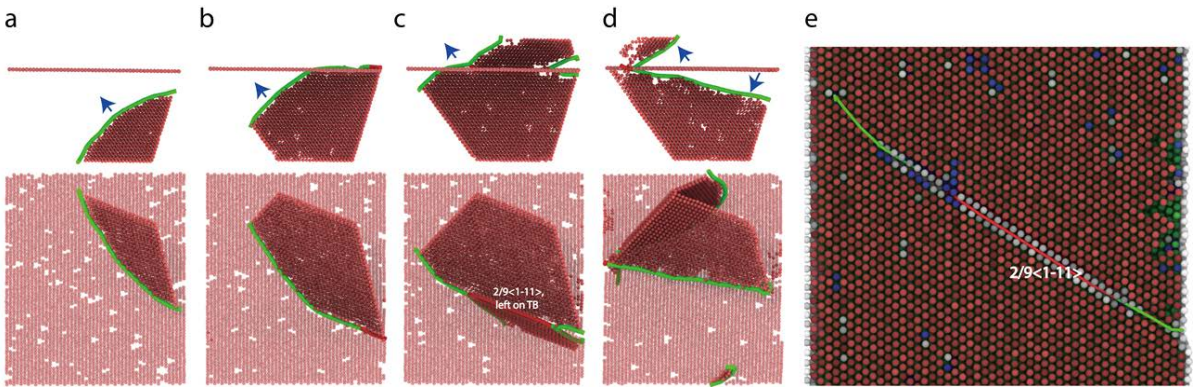

Figure 4.6 | Snapshots of typical slip dislocation nucleation in a bi-twinned. a, Nucleation of a leading partial from a corner of the NW in the dominant twin variant (dislocation line shown here is post-processed through Ovito's DXA algorithm: green lines for partials and red line for stair-rod dislocation). **b**, Glide of the leading partial over the cross-section of the NW. **c**, Cross-slip of the leading partial through the twin plane to the smaller twin variant. Nucleation and glide of the trailing partial. **d**, Escape of the leading and trailing partials at the free surface. **e**, The atom arrangement of the twin boundary after leading partial cross-slip the twin plane as showed in **c**, the red line indicates the stair-rod dislocation on the twin boundary.

4.3.4. Tensile Detwinning in Bi-twinned NWs

In contrast to the dislocation slip dominated deformation described above, experiments confirmed large plasticity in the bi-twinned Ag NWs with small volume ratios (Fig. 4.3b,e). A tensile detwinning deformation was identified to contribute to the large plasticity in such bi-twinned NWs. From MD simulations, I found that the new tensile detwinning mechanism in bi-twinned NWs contains two steps as shown in Fig. 4.7: *the first step* is the nucleation of a single phase embryo and formation of the unique TB-GB-TB structure (Fig. 4.7ii) in the middle of the NW through multiple dislocation interactions at the parallel twinning boundary. In *the second step*,(Fig. 4.7iii), after the

single phase has nucleated, further loading leads to the expansion of the single phase via continuous dislocation nucleation. I'll explain this two-step detwinning mechanism in detail in the following parts.

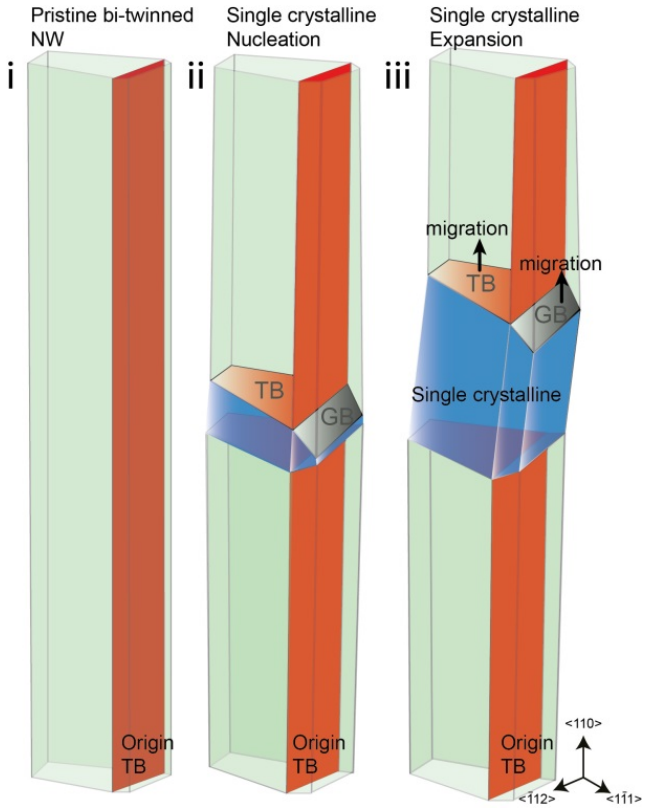

Figure 4.7 | Schematic Figs showing two steps of the tensile detwinning mechanism in bi-twinned NW. i, The pristine bi-twinned NW. **ii**, Step one, single crystalline (colored by blue) embryo nucleated in the middle of bi-twinned NW through multiple dislocation interactions at the parallel twinning boundary and formed a unique TB-GB-TB structure. **iii**, Second step, single crystalline expansion through dislocation nucleation from the triple junction of inclined TB, GB and original TB, lead to tensile detwinning and superplasticity in bi-twinned NW.

Step-one detwinning: Different from the previous localized slip mode that single dislocation nucleated and propagated to the free surface, when grain volume ratio is small, multiple dislocations tend to react on the TB and lead to detwinning of a small segment TB, this dislocation reaction induced detwinning is the step-one detwinning showed in Fig. 4.7ii. Figure 4.8 shows the snapshots of the step one detwinning in MD simulation. I can observe multiple dislocation reactions around the initial detwinning site. Detail dislocation reactions in step one detwinning is described in the following part.

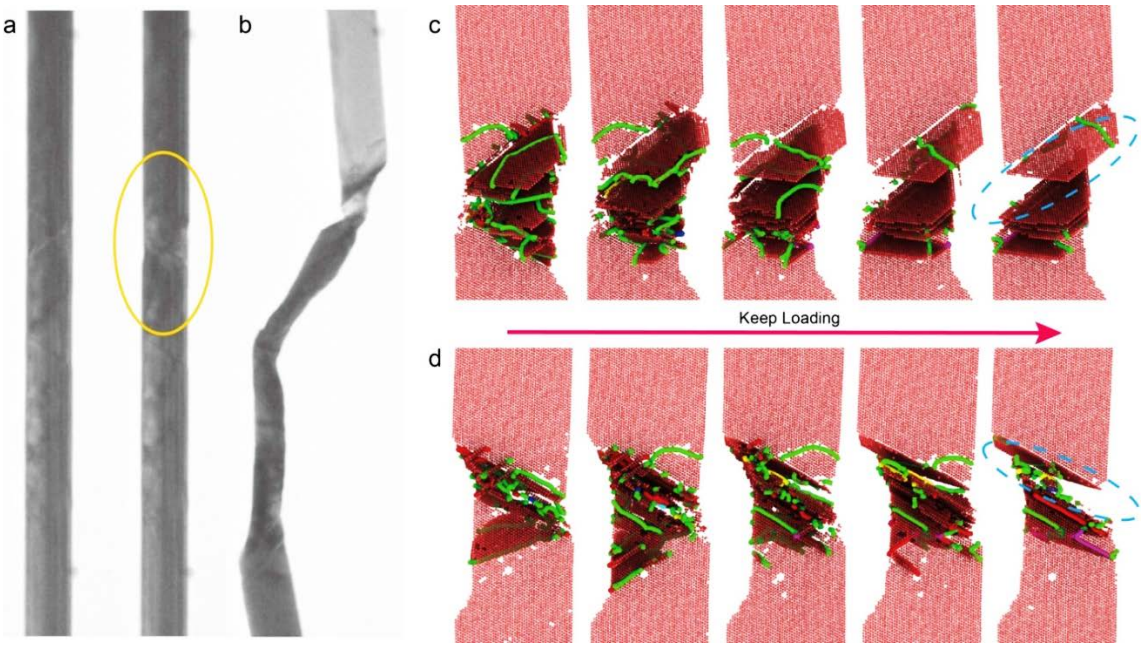

Figure 4.8 | Step one detwinning in a bi-twinned NW. a, TEM images of a bi-twinned NW with small volume ratio subjected to tension. The yellow circle shows some complex dislocation activities related to the detwinning process. **b**, After the detwinning process, subsequent twinning deformation leads to superplasticity in the bi-twinned NW. **c**, Snapshots of complex dislocation activities of step one detwinning in MD simulations. Green lines indicate dislocation lines, and red atoms are HCP atoms. The detwinned region is marked by the dashed blue circle. **d**, Viewed from the other side of **c**. In **c**-**d**,

dislocations can be seen nucleating in two twin variants, propagating in both $\{111\}$ and $\{11\bar{1}\}$ planes, and interacting with the TB.

The detailed dislocation activities in step one detwinning process are illustrated in Fig. 4.9a-d. Initially, two partials, $\boldsymbol{\alpha B}$ and $\boldsymbol{\alpha C}$ nucleated from the surface but on neighboring slip planes ***BCD*** (Fig. 4.5c) react on the TB and form a temporary partial $\boldsymbol{D\alpha}$, which decomposes into another stair-rod dislocations $\boldsymbol{\alpha\delta}$ and a Hirth dislocation (115), $\frac{1}{3}\langle 010\rangle$ (Fig. 4.9a). Because of the high energy state of the two newly formed dislocations, an extended jog is formed among them with a new partial $\boldsymbol{\delta C}$ in plane ***ABC*** which will glide along $\langle 10\bar{1}\rangle$ direction within the TB (Fig. 4.9b). Partials nucleated from the surface on the neighboring slip planes will be block by the TB and tend to react on the TB. In Fig. 4.9c, partials $\boldsymbol{\alpha B}$, $\boldsymbol{\alpha C}$ from the same grain react with a partial $\boldsymbol{D\alpha}$ on neighboring planes and form two twinning partials $\boldsymbol{\delta C}$, $\boldsymbol{\delta B}$ between them. Similarly, partials $\boldsymbol{\alpha' B}$, $\boldsymbol{\alpha' C}$ in the mirror grain can also react with $\boldsymbol{D\alpha}$ on neighboring planes and form two twinning partials $\boldsymbol{\delta C}$, $\boldsymbol{\delta B}$ as showed in Fig. 4.9d. Subsequent dislocation nucleation, propagation and interaction continue to contribute to the generation of twinning partials segments $\boldsymbol{\delta C}$, $\boldsymbol{\delta B}$. These twinning partials span over several atomic planes, around 0.5nm in length (decided by the spacing of reacting partials), and they glide within the TB in $\langle 10\bar{1}\rangle$ or $\langle 011\rangle$ direction (the NW axis direction is <110>) and induce migration of a narrow segment of the TB, finally leading to the nucleation of a single crystalline embryo (Fig. 4.7ii). At each interface of the single crystalline embryo and a bi-twinned part, a unique TB-GB-TB structure is formed (Fig. 4.10b), which contains a low-energy, inclined TB in the dominant twin variant and a high-angle GB in the other twin variant.

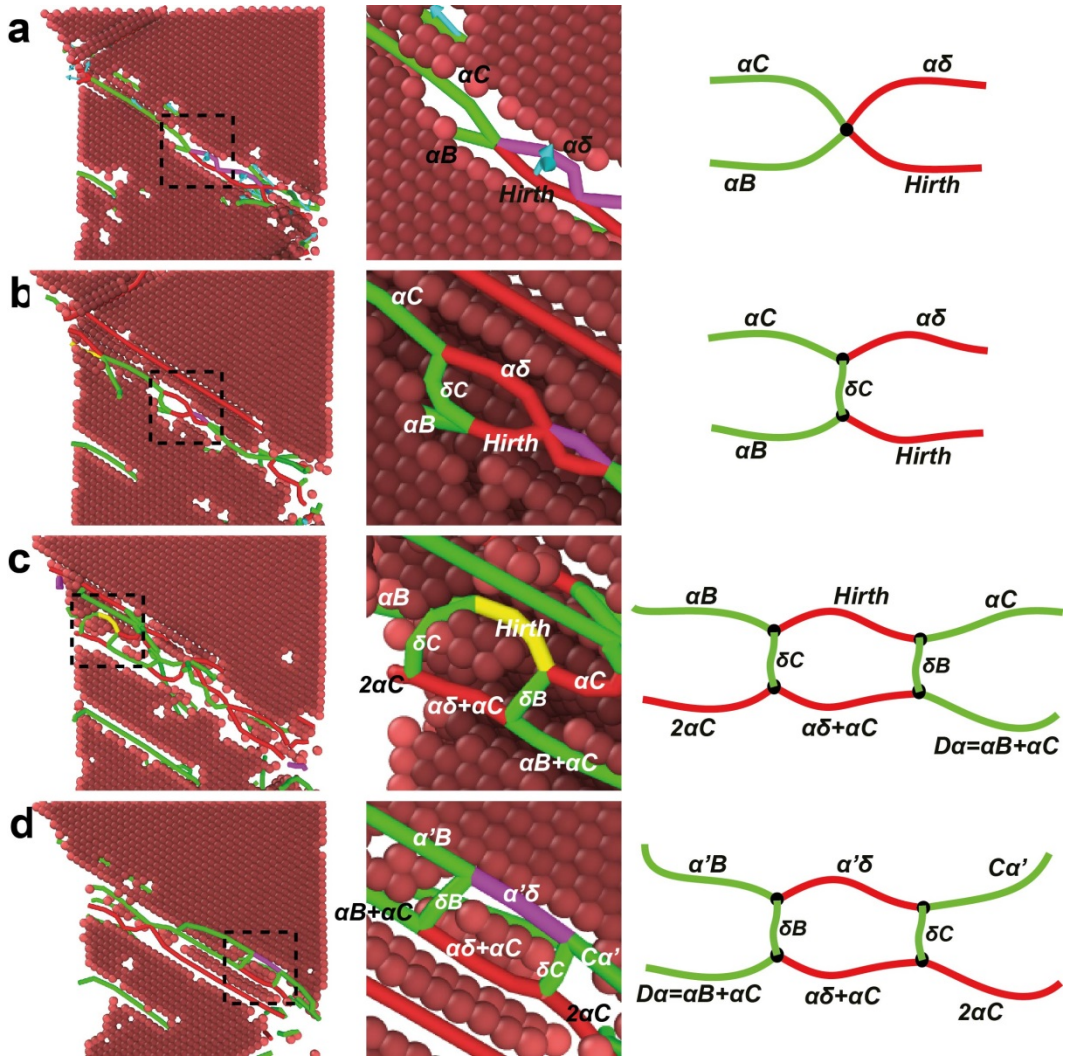

Figure 4.9 | Representative dislocation reactions during step one of the tensile detwinning process. Only hexagonal close-packed atoms are made visible

Step-two detwinning: Once the single crystalline embryo is nucleated and the unique TB-GB-TB structure formed, the step-two detwinning mechanism will dominate under further loading. Figure 4.10d shows the step-two detwinning mechanism in which twinning partials continue nucleating at the triple junction between the newly formed TB and GB and original TB, leading to the migration of the inclined TB and GB and the expansion of the single crystalline phase. Figure 4.10a,c show the cross-sections of the

original bi-twinned phase and the newly formed single crystalline phase, respectively. The bi-twinned NW with <110> axis is transformed into the single crystalline phase with <001> axis by coherent twinning migration from the detwinning site during the step-two detwinning, which is somewhat similar to the deformation mechanism in single crystalline Ag NWs

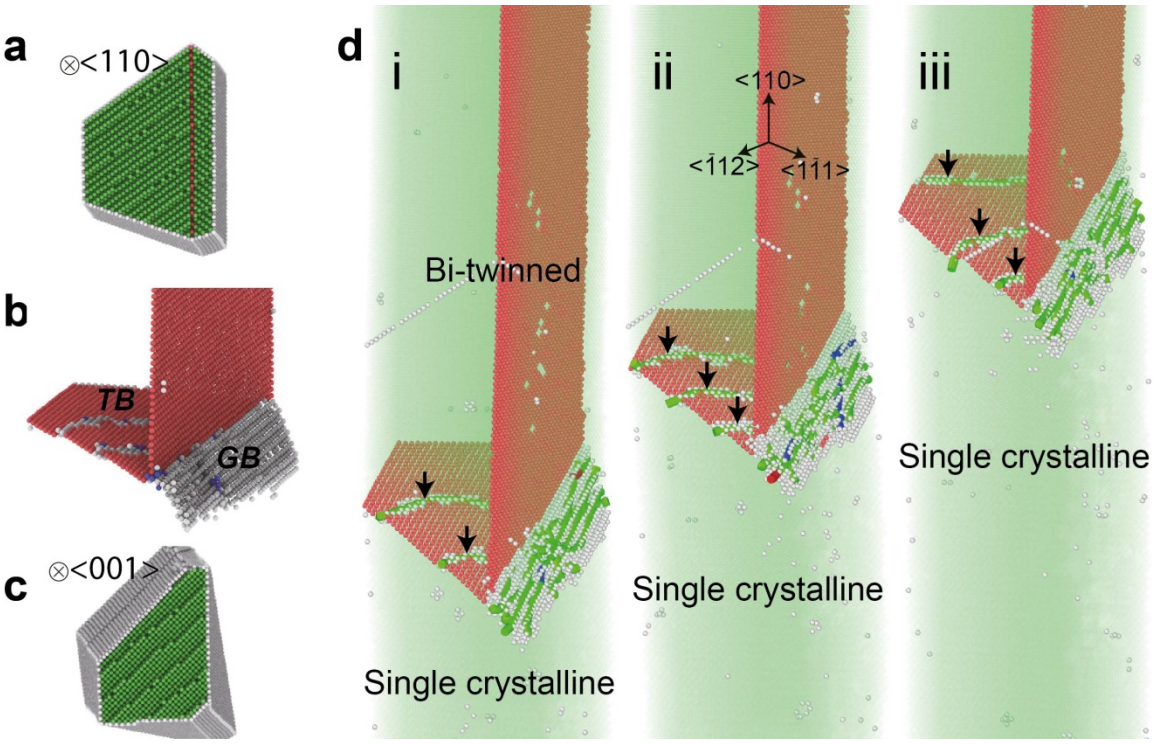

Figure 4.10 | Step two detwinning in a bi-twinned NW. a, Cross-section of the bi-twinned phase with axial direction of <110>. **b**, Detailed structure of the newly formed TB-GB-TB structure during the step one detwinning process. **c**, Cross-section of the single crystalline phase with the axial direction reoriented to <001>. **d**, MD snapshots in step two detwinning. Dislocations continuously nucleated from the surface joint among the newly formed TB-GB-TB (large resolved shear force involved on inclined TB), leading to TB-GB migration and thereby converting the bi-twinned structure to single crystalline structure. Black arrows indicate the partials on the inclined TB that lead to TB migration.

In short, I found that a novel tensile detwinning deformation mechanism leads to the observed large plasticity in bi-twinned NWs with a small volume ratio, characterized by interaction of multiple dislocations with the original TB, which is different from dislocation slip dominated deformation in bi-twinned NWs with balanced volume ratios and twinning dominated deformation in single crystalline NWs.

Detwinning has been extensively studied recently especially in FCC metals (34, 114, 116-118). The key to detwinning is to nucleate a partial in the twinning plane at the TB. Zhu *et al.* (114) proposed a detwinning mechanism via cross-slip of partials into the twinning plane at the TB. Subsequent dislocation interactions with the TB continue the detwinning process. Wang *et al.* (116) attributed the detwinning to the rapid migration of incoherent TBs formed by twinning partials during compressive loading. Defective twin boundaries with kinks can also easily migrate under shear stress (119). Twinning partials from the incoherent TBs can directly activate the detwinning process owing to the shear stresses. Detwinning has also been observed in Cu nanopillars (34) and Au NWs (117) with preexisting TBs under tension and compression, respectively. In all these cases, a finite resolved shear stress is needed for the detwinning process. In contrast, the detwinning mechanism reported here is unique in that the loading direction is parallel to the twinning plane and there is no resolved shear stress. Therefore, I have found a novel two-step tensile detwinning mechanism that starts with multiple dislocation interactions with the TB and nucleation of a single crystalline embryo, followed by migration of a unique newly formed TB-GB-TB structure that finally leads to superplastic deformation.

4.4. Energetic model for prediction

There are two deformation modes observed in the bi-twinned NWs. One is superplasticity due to tensile detwinning and the other is localized slip failure with limited plastic strain. How do we determine the dominant deformation mode in a bi-twinned NW based on its geometry? Here, I'll propose an energetic model to predict the deformation mode of bi-twinned NWs and verify it with the experiment and simulation data.

As discussed above, this new tensile detwinning mechanism includes two steps. Whether the step one - nucleation of the single crystalline embryo - can occur determines the succeeding deformation mechanism of bi-twinned NW. During the step one detwinning, dislocation reactions on TB finally lead to a small segment of detwinning and the formation of a unique TB-GB-TB structure (Fig. 4.10b) – a low energy TB in the dominant twin variant and a high-angle GB in the other twin variant. The energy change associated with the step-one detwinning process can be calculated as the energy needed to create these new boundaries:

$$\Delta E = 2A_1\gamma_{twin} + 2A_2\gamma_{GB} \tag{4.1}$$

where A_1 and A_2 are the areas of the TB and the high-angle GB in Fig. 4.10b; γ_{twin} and γ_{GB} are the interfacial energies of TB and the newly formed high-angle GB, with the values of 5.9 and 539 mJ/m^2, respectively from MD simulation. Equation (4.1) describes the energy difference of the system after the nucleation of the single phase embryo, in other word, it's the formation energy of the unique inclined TB-GB-TB structure, and it can be the energy criterion for the step-one detwinning. This energy change as a function

of the volume ratio for a fixed H = 9 nm and W = 13 nm NW is plotted in Fig. 4.11a. The volume ratio in bi-twinned NWs can be quite different, ranging from 0.1 to 1.0 in the 20 NWs examined in our experiments. It can be seen that ΔE can be reduced by decreasing the volume ratio, indicating that a reduced volume ratio can facilitate the detwinning process in bi-twinned Ag NWs.

To systematically investigate the transition of the two deformation mechanisms in bi-twinned NWs, a parametric study was conducted in MD simulations. Inset in Fig. 4.11a shows the cross-section of the simulated bi-twinned NWs, where W, H and h_1 are the independent geometrical parameters. For a given value of H, the energy difference of the detwinning process ΔE in equation (4.1) can be expressed in terms of two dimensionless parameters: H/W and volume ratio $r \in (0,1]$:

$$\Delta E(A_1, A_2) = \Delta E(W, H, h_1) = \Delta E(H, H/W, r) \tag{4.2}$$

According to the geometrical relations, one finds

$$\begin{aligned} \Delta E &= 2A_{twin}\gamma_{twin} + 2A_{gb}\gamma_{gb} \\ &= 2(\sqrt{\frac{3}{2}}Wh_1 - \frac{3\sqrt{3}}{8}h_1^2)\gamma_{twin} + 2(2Wh_2 - \frac{3\sqrt{2}}{4}h_2^2)\gamma_{gb} \qquad (h_1 \geq h_2) \end{aligned} \tag{4.3}$$

The twin volume ratio is defined as $r = \frac{A_2}{A_1} \in (0,1]$, where

$$A_1 = (W - \frac{3\sqrt{2}}{8}h_1)h_1,\ A_2 = (W - \frac{3\sqrt{2}}{8}h_2)h_2$$
$$\text{and} \quad H = h_1 + h_2$$

The contour of ΔE is plotted in Fig. 4.11b for a fixed H = 8.9 nm, where the x-axis is H/W and the y-axis is r. The color from blue to red indicates an increase in ΔE. The value

of ΔE varies for different H, but the contour lines are the same regardless of H. The plot shows that NWs with smaller volume ratio and larger *H/W* have lower energy change, thus favoring detwinning; while those with larger volume ratio and smaller *H/W* have higher energy change, thus favoring a dislocation slip dominated mechanism.

As showed by the blue triangle dots in Fig. 4.11b, the MD simulations suggested a transitional deformation mode in between the two deformation mechanisms. The details of the transitional mode are shown in Fig. 4.12. In this mode, dislocation slip dominated initially, leading to a necking of the NW in the *W* direction, which increased the *H*/*W* value in the necking region. This geometrical change made detwinning more favorable in the necked region according to the energy contour plot Fig. 4.11b, and very limited detwinning would occur in the necking region, as observed in the MD simulations.

Based on the experimental and simulation results, a transition line, corresponding to a critical ΔE of 140eV for H=8.9 nm, was found to separate the dislocation slip mechanism and the detwinning-twinning mechanism in bi-twinned Ag NWs (Fig. 4.11b). Our simulation results over 100 different case studies showed good agreement with the prediction based on ΔE. The transitional mode of mixed deformation mechanisms describe in Fig 4.12 was frequently seen around this transition line. In addition, a total of 20 experimental data are included in Fig. 4.11b (solid symbols), also in good agreement with the prediction based on ΔE.

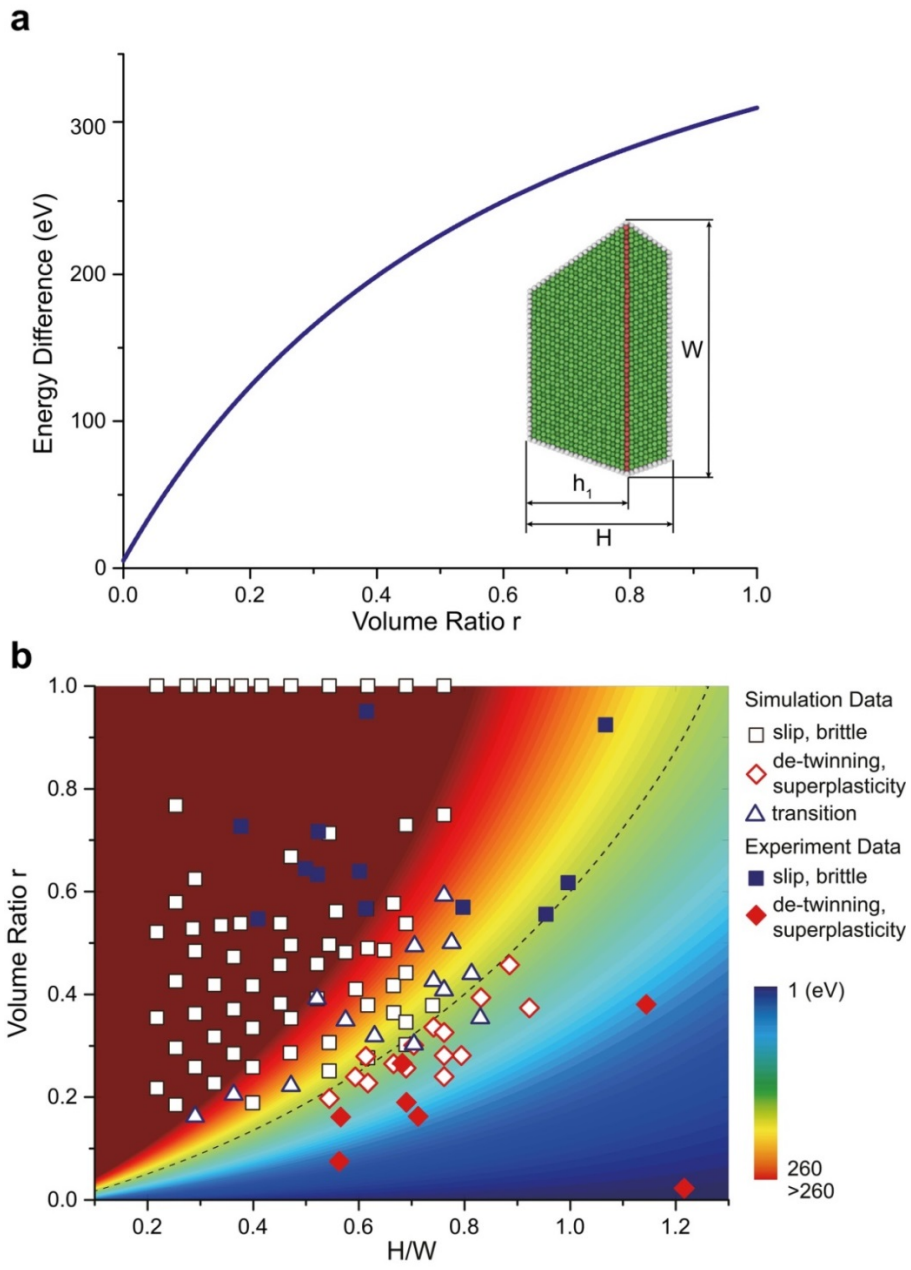

Figure 4.11 | Transition of deformation mechanisms in bi-twinned Ag NWs. a, Energy difference associated with the detwinning process as a function of the twin volume ratio for a sample with fixed W and H. Inset in **a** shows the cross-section of a typical bi-twinned NW in MD simulation and its corresponding geometrical parameters. **b**, Contour plot of energy difference in the detwinning process for a fixed H as a function of *H/W* and twin volume ratio r, along with simulation and experimental data. For the simulation results: open black squares, open red rhombuses and open blue triangles stand

for the slip dominated mode, the detwinning-twinning mode and the transitional deformation mode, respectively. For the experiment results: solid blue squares and solid red rhombuses stand for the slip dominated mode and the detwinning-twinning mode, respectively.

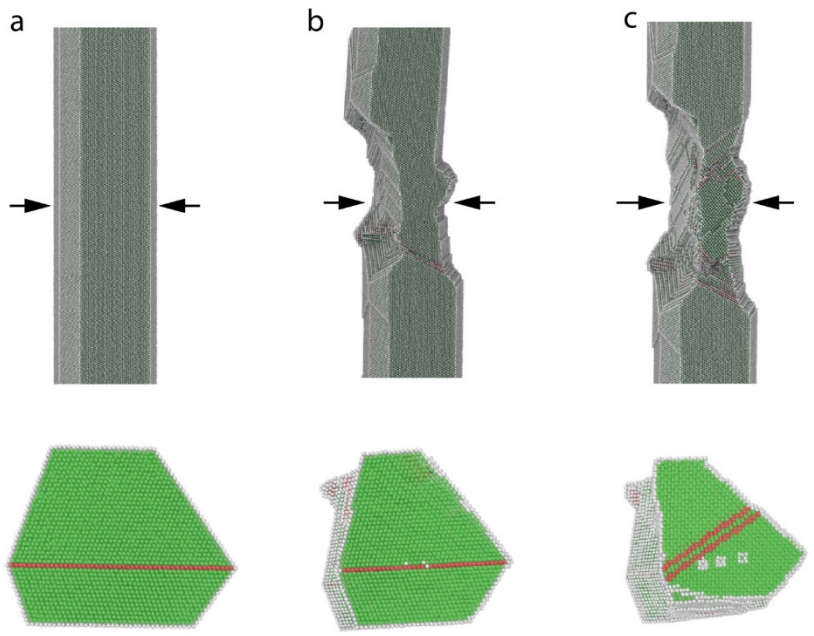

Figure 4.12 | A transition mode of deformation with mixed slip and detwinning in a bi-twinned NW. a, A bi-twinned NW before deformation. The lower image shows the cross-section at where the black arrows point to in the upper image. According to our theoretical model, this NW falls on the left of the dashed line in Fig. 4.11b, where dislocation slip dominates. **b**, After loading, the NW is deformed as predicted, with dislocation slip leading to necking of the NW in W direction. However, in the necking region, increased H/W makes detwinning more favorable. **c**, Detwinning is observed in the necking region. Due to the localized necking region, plasticity is still limited in this case.

4.5. Additional Discussion

4.5.1. Decoupling step-one and step-two detwinning in bi-twinned NWs

It is worth noting that in most experiment samples, the tensile detwinning process in bi-twinned NWs did not propagate as far as the twinning process in single crystalline NWs before failure, as shown in Fig. 4.3e. This is attributed to the competition between shear localization and tensile detwinning in bi-twinned NWs, as supported by MD simulations (shown in Fig. 4.13). In some cases, tensile detwinning can propagate through the whole NW, leading to large plasticity as in the case of single crystalline NWs. However, in most cases, shear localization and failure can occur close to the initial detwinning site after tensile detwinning propagates a certain distance. Figure 4.13 demonstrated two typical levels of superplasticity in bi-twinned NW. In case i, the whole NW can be detwinned, with an overall elongation of 45% (as good as single crystalline NW). In case ii, after a certain tensile detwinning, shear localization occurred in the detwinned region and led to the necking failure (an overall fracture strain of 28%). However, the elongation in bi-twinned NWs is still much larger than those in bi-twinned NWs with large volume ratio. The competition of tensile detwinning and shear localization depends on the detwinning energy that is related to the volume ratio. As I discussed before, the tensile detwinning is a two-step process. Step-one detwinning is through multiple dislocation reactions. During the complex dislocation reactions in step-one detwinning, many defects such as stacking fault and surface steps were created along with the single crystalline embryo. These defects will be the potential sources for shear localization and compete with step-two detwinning mechanism with further loading.

However, if I can decouple step-one detwinning and step-two detwinning, I can eliminate the defects that created along with the step-one detwinning and the whole bi-twinned NW is expected to be detwinned. In the following part, additional MD simulations were done to decouple the step-one and step-two detwinning.

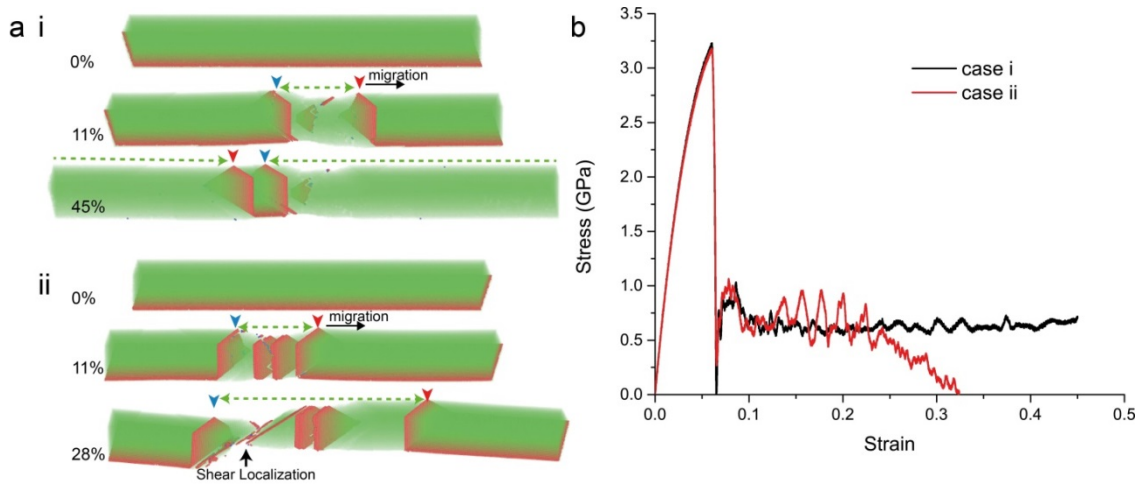

Figure 4.13 | Different levels of superplasticity in bi-twinned NWs. a, Snapshots of detwinning process in two different cases of bi-twinned NWs. Green dashed line indicated the detwinned region. The blue and red arrows indicated two ends of the single crystalline region. Periodic boundary condition was set along the axial direction of NWs. In case i, the TB-GB junction indicated by the red arrow migrated (or propagated) to the right to detwin the NW; it went through the periodic boundary at the end until met the blue arrow. Finally the whole NW can be detwinned, with an overall elongation of 45%. In case ii, after a certain tensile detwinning, shear localization occurred in the detwinned region and led to the necking failure (a fracture strain of 28%), as indicated by the black arrow. **b,** Stress-strain curves of the two different bi-twinned cases.

When the bi-twinned NWs are under tensile loading, the two step detwinning can only occur in order. Whether the step one detwinning can occur determines the succeeding

deformation mechanism of bi-twinned NW, and that's the physical process described by our energetic model in Chapter 4.4. If NW cannot overcome the energy barrier for step-one detwinning, it will fail by planar slip with limited plasticity. In additional, the quality of this step-one detwinning also determines whether the detwinning can propagate along the whole NW as showed in Fig. 4.13.

In MD simulations, I can construct a perfect step-one detwinning by directly manipulating crystalline structure and avoiding dislocation reactions, and then study the step two detwinning. Figure 4.14 showed that, by cutting the bi-twinned NW and single crystalline embryo and then welding the two pieces according the unique TB-GB-TB structure that observed after step-one tensile detwinning process in previous simulations, I can create the bi-twinned NW with a single crystalline embryo without multiply dislocation reactions in step-one tensile detwinning. When tensile loading is applied to these samples, step-two detwinning mechanism is activated and bi-twinned NW will be detwinned and shows the superplasticity.

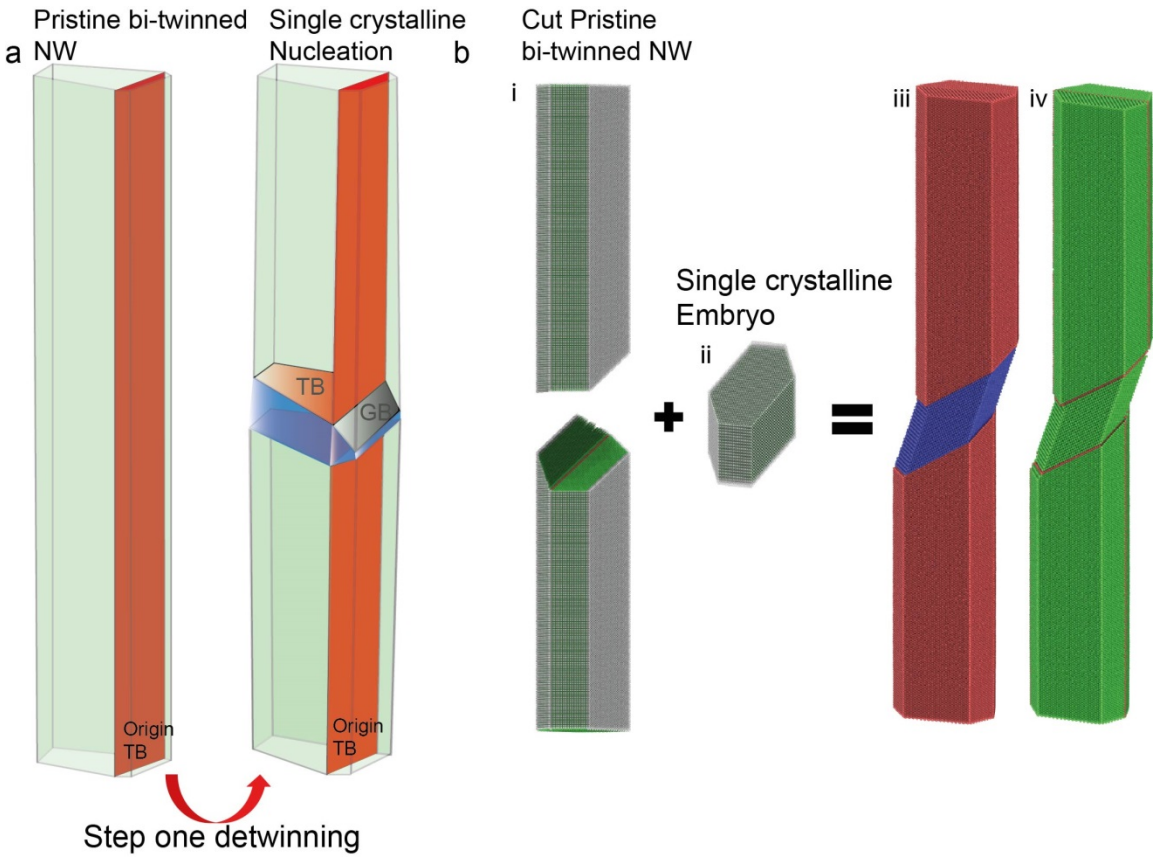

Figure 4.14 | Directly construct step-one detwinning by crystalline geometry. a, Schematic Figs of step-one detwinning process. **b**, Cut the bi-twinned NW (**b**.i) and single crystalline embryo (**b**.ii) and then weld the two pieces according the unique TB-GB structure that observed during step-one tensile detwinning process. **b**.iii shows the bi-twinned NW with single crystalline embryo.The red color stands for the bi-twinned structure, the blue color stands for single crystalline embryo. **b**.iv shows the structure colored in CNA method. Green represents perfect FCC atoms and red represents HCP atoms.

I studied three different bi-twinned NWs (Fig. 4.15). All of them fall into the brittle, slip region in Fig. 4.11b and showed planar slip without detwinning due to the high energy required for step-one detwinning. However, when the single crystalline embryos were directly constructed and step-one detwinning was skipped, step-two detwinning will

be the dominate deformation mechanism in all these NWs, and finally all the NWs were detwinned and failed with superplasticity, as showed in Fig. 4.15b-d. We can observe more stacking faults left in the sample with large volume ratio r, but the origin TB was totally detwinned in all cases and NWs showed a comparable superplasticity to the single crystalline NWs.

These results in Fig. 4.15b-d consistent with our previous hypothesis about shear localization competing with step-two detwinning. When a single crystalline embryo was directly constructed instead of through dislocation reactions, all the potential defects in the system to compete with step-two detwinning were eliminated and all the samples can be detwinned through the whole NW regardless of the sample geometry and detwinning energy. In addition, by decoupling step-one and step-two detwinning, I further prove that step-one de-twinning is the key step to determine the whole deformation mechanism. The currently energy criterion that consider the step-one detwinning is reasonable.

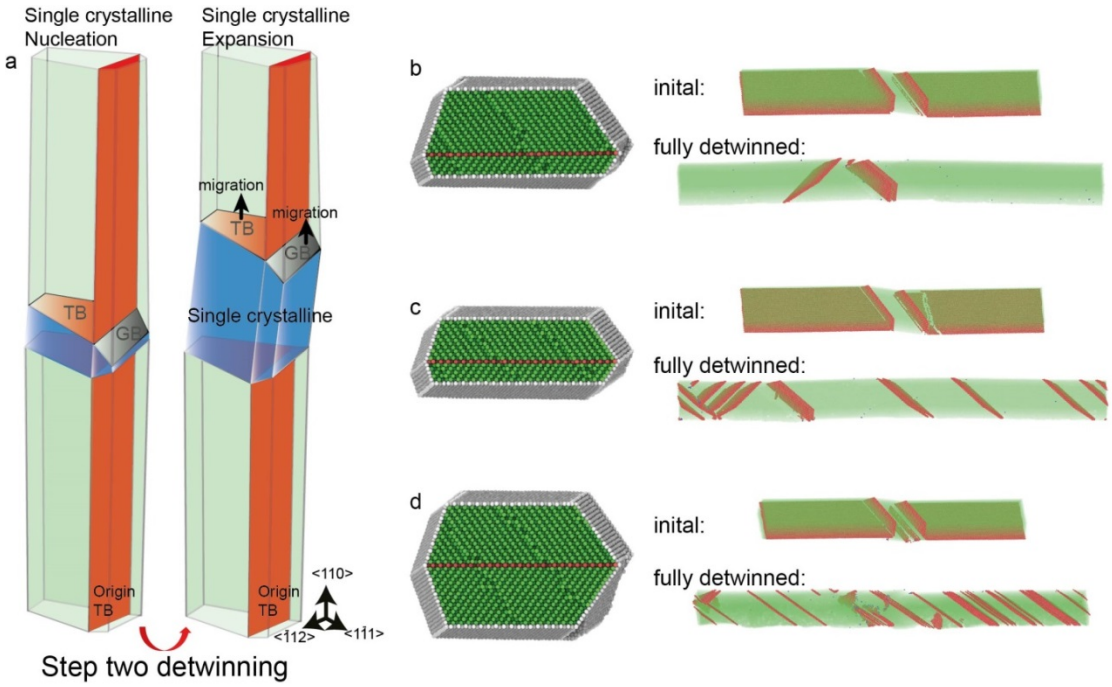

Figure 4.15 | Step-two detwinning with samples directly constructed from step-one detwinning. a, Schematic Figs of step-two detwinning process. **b-d,** The bi-twinned NWs that cannot overcome the energy barrier for step-one detwinning. When introduce the single crystalline embryo by crystalline geometry and skip step-one detwinning according to Fig. 4.15, they can be fully detwinned during tensile loading by step-two detwinning mechanism.

4.6. Summary

In this chapter, I have explored a transition between two deformation modes, dislocation slip and tensile detwinning, in bi-twinned FCC metallic NWs via MD simulations. Localized dislocation nucleation and propagation across the TB led to permanent planar sliding and limited fracture strain in bi-twinned NWs with balanced volume ratios, while a unique two step tensile detwinning deformation resulted in

superplasticity in those with small volume ratios. The detwinning process is unexpected in view of the absence of resolved shear stress on the TB and is attributed to complicated dislocation interactions with the TB that can alter the local atomic arrangement during step-one detwinning. The step-two detwinning mechanism observed in bi-twinned metallic NWs is somewhat similar to that in single crystalline metallic NWs due to coherent twinning propagation. A criterion for the detwinning deformation was proposed based on the detwinning energy barrier, which was shown capable of capturing the effects of the volume ratio and cross-sectional aspect ratio on the transition of deformation modes in bi-twinned NWs. Among the single crystalline, bi- and penta-twinned Ag NWs, bi-twinned Ag NWs offer the best combined mechanical properties.

Chapter 5 Hydrogen Embrittlement in Penta-twinned Silver Nanowire

The work described in this Chapter is in collaboration with Dr. Guangming Chen and Tzu-Hsuan Chang from the experimental group of Prof. Yong Zhu, who performed the *in situ* experiments.

5.1. Introduction

Impurity atoms in the environment, such as hydrogen, can have a deleterious effect on a wide range of structural metals and alloys, which is a centuries-old problem known as hydrogen embrittlement (HE) (120-122). Many different effects can be attributed to the presence of hydrogen in metals; thus, the exact mechanism of HE remains controversial. Different mechanisms have been proposed (123, 124), such as H-enhanced de-cohesion (HEDE) (125, 126), H-enhanced local plasticity (127-129), blister/bubble formation (130, 131), interface failure (132, 133) and hydrogen-induced superabundant vacancies (134-136). However, these mechanisms are not exclusive and multiple mechanisms could be active over different areas. There are also debates about the effects of hydrogen on dislocation motion. Continuum theory and atomic-scale simulation show that in the presence of hydrogen, the solute drag force exerted on a moving dislocation will add resistance to dislocation motion (137-140). A hydrogen shielding model proposed that hydrogen can reduce the long-range elastic interaction between dislocations, thus making individual dislocation motion easier (124, 129). A recent study showed that hydrogenated vacancies can lock dislocations in aluminum (141). Most of these studies focused on the

movement, multiplication and interaction of dislocations with solute hydrogen in bulk materials; however, in nanoscale, due to dislocation starvation, dislocation nucleation plays a dominant role in the deformation mechanism (4, 73, 105, 142-146). Therefore, new insight is required into the hydrogen embrittlement mechanism in nanostructure materials.

Dislocation nucleation by nanoindentation in bulk systems in the presence of hydrogen has also been studied in various experiments and simulations. In experiments, it has been observed that hydrogen can reduce the activation energy for homogeneous dislocation nucleation and decrease the pop-in stress (147). In simulations, the presence of hydrogen has a limited effect on the pop-in load and can be entirely attributed to lattice dilation (148, 149). In simulations, the effects of hydrogen on dislocation nucleation are very complicated and are affected by many factors, such as strain rate, nucleation source and initial defects. Pre-existing dislocation and defects cannot be neglected in hydrogen-charged dislocation nucleation simulations (150, 151). Different from the homogeneous dislocation nucleation under nanoindentation (152), the emission of dislocations from the crack tip was found to be suppressed by the accumulation of high concentrations of hydrogen (153, 154). Despite the extensive studies of HE in bulk systems, there has been little study on hydrogen's effect on the mechanical properties of nanoscale systems (155-157), especially nanowires with a large surface/volume ratio.

In this chapter, I report enhanced yield strength and a transformation of failure mode from distributed plasticity (158) to localized necking in penta-twinned Ag nanowires in the presence of hydrogen. By large-scale atomistic simulations, I show that the

underlying mechanism of surface nucleation was suppressed due to the presence of hydrogen, leading to a higher yield strength and more localized necking failure.

5.2. Tensile Testing

5.2.1. *In-situ* TEM tensile testing

Based on TEM characterization, the NWs are straight and uniform in diameter, with a growth direction of <110> (Fig. 5.1a). The inset in Fig. 5.1a shows a cross-sectional TEM image of a penta-twinned Ag NW, with five-folded twining grains running parallel to the length direction. In this study, Ag NWs were immersed in H/Ar (molar ratio, 1:1) atmosphere for hydrogen charging. The relative concentration of hydrogen inside the samples was characterized by Time-of-Flight Secondary Ion Mass Spectrometry (SIMS). The increment of hydrogen (ΔH) in the samples (compared to the value in the as-received sample) ranges from 0.15 to 0.80% owing to different charging times (12 to 48 hrs.), as shown in the inset in Fig. 5.1b. *In-situ* TEM tensile testing were performed using a microelectromechanical system (MEMS) based tensile testing stage that allows accurate measurements of both load and displacement simultaneously, as well as real-time imaging of microstructure evolution during deformation. Figure 5.1b shows the stress-strain responses for Ag NWs with different H concentrations inside. Figure 5.1c, d shows snapshots of microstructure evolution for typical tensile tests of an as-received Ag NW and the one with ΔH of 0.80%. All the tested NWs have a closed diameter of 71±3 nm. As shown in Fig. 5.1b, with the increase of hydrogen inside the NWs (ΔH, from 0 to 0.80%), the yielding strength and ultimate strength are increased from 0.95 and 1.02 GPa to 1.54 and 1.59 GPa; the total elongation (measured between the two deposited local

markers) is dramatically decreased (from 4.92 to 2.32%). This presents a clear phenomenon of hydrogen-induced embrittlement in the NWs owing to the diffusion of hydrogen. From the snapshots in Fig. 5.1c, d, as the applied stress was over the yield strength, multiple dislocations nucleated from the free surface and propagated into the as-received NW (Fig. 5.1c-ii). As the load increased, multiple necking was observed in the as-received NWs leading to substantial plasticity (Fig. 5.1c iii-iv). In the NW with ΔH of 0.80%, there was rarely dislocation activity until the applied stress was close to the ultimate tensile strength (Fig. 5.1d ii-iv), yet the NW was almost immediately fractured when the plastic deformation was activated. Multiple dislocation nucleation and propagation were observed in the NW with ΔH of 0.41%. These results suggest that the diffusion of hydrogen inside the metallic NWs directly suppress the nucleation of surface dislocation.

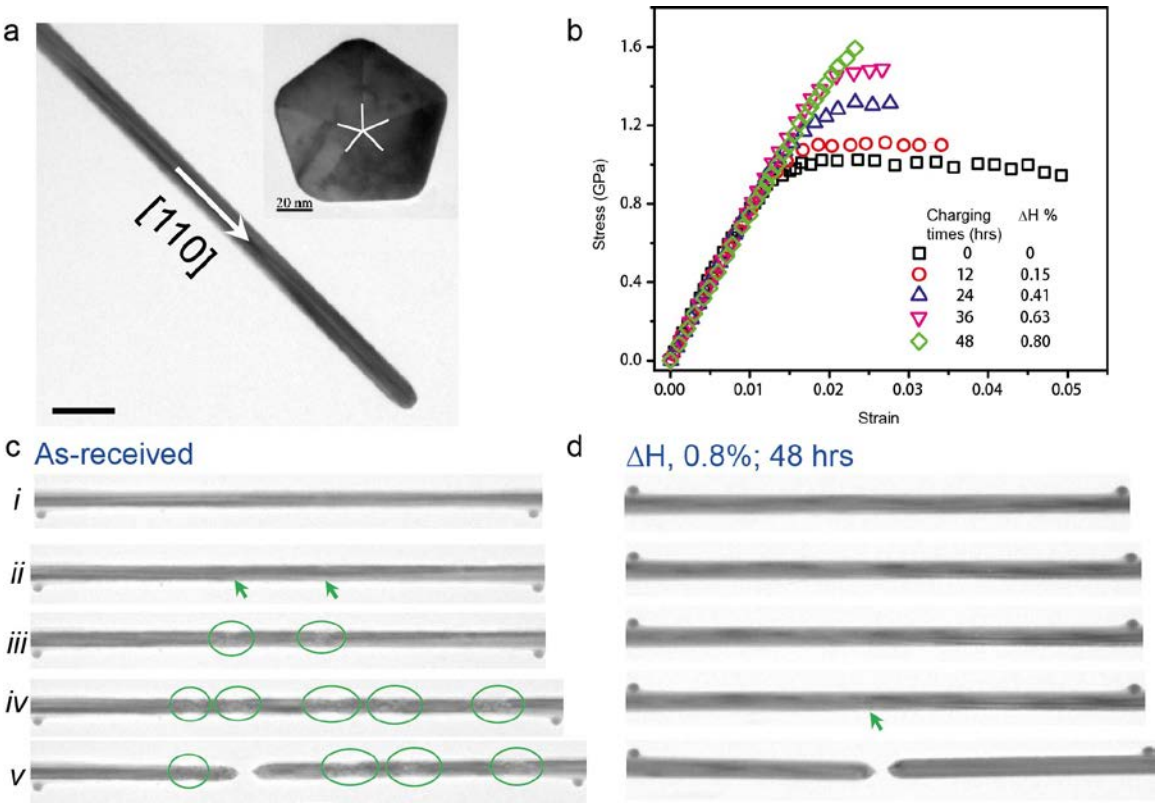

Figure 5.1 | Characterization of penta Ag NWs and TEM tensile tests. a, Penta-twinned NW TEM sample, which is straight and uniform in diameter, with a growth direction of <110>. **b**, Stress-strain responses for Ag NWs with different H concentrations. **c,** Distributed plasticity in a penta-twinned NW without hydrogen. **d,** Localized failure of a penta-twinned NW with hydrogen. (Courtesy of Prof. Yong Zhu and Dr.Guangming Chen)

5.2.2. MD simulations of tensile testing

To reveal the underlying mechanism behind the observed enhanced yield strength and localized necking behaviors of penta-twinned Ag NWs, I performed a series of molecular dynamics simulations. Details of the simulations are supplied in part **5.4.1**. Dislocation nucleation is very sensitive to pre-existing defects, surface roughness and other types of nucleation sites (73, 159-161). Previous studies (66) have shown that vacancy defects can

significantly decrease the activation energy for surface dislocation nucleation. In the current atomic model, I introduced a uniformly distributed vacancy as initial defects to promote surface dislocation nucleation. Hydrogen atoms were randomly inserted into the interstitial sites in the crystalline lattice.

The strain rate is of critical importance in current simulations. To capture the hydrogen effect in simulation, the loading time scale should be comparable with the hydrogen diffusion time scale; otherwise, hydrogen will behave like sessile inclusions and promote dislocation nucleation, and all the effects will be attributed to lattice distortion. To overcome the time scale issue, a strain rate of 10^6 and an enhanced temperature of 800K were adopted in our tensile atomic simulations. Figure 5.2a shows snapshots of the failure mode transition in the simulations. In hydrogen-free NWs, dislocation nucleation is evenly distributed in the whole NW, which is consistent with distributed plastic deformation. In the presence of hydrogen, localized dislocation nucleation and necking are captured by the simulation. The stress-strain curves in Fig. 5.2b show that in the presence of hydrogen, yield strength is higher than the hydrogen-free NW, which is consistent with the enhanced yield strength observed in the experiment. The consistent results of our simulation show that low strain rates and pre-existing defects are necessary for atomic modeling of the hydrogen effect in this nucleation-controlled plasticity mechanism. Surface dislocation nucleation is the dominant deformation mechanism in NWs due to the small size and dislocation starvation (73, 105, 142-145, 158). The distributed plasticity in pristine penta-twinned NWs in our experiments is a typical example of the dislocation nucleation-dominated deformation mechanism. The transition of this distributed plasticity to localized necking in the presence of hydrogen implies that,

in contrast to previous HE mechanisms in bulk systems and homogeneous dislocation nucleation under nanoindentation, the hydrogen in NWs will dramatically affect the surface dislocation nucleation. The presence of hydrogen around the surface nucleation sites will increase the activation energy and suppress surface dislocation nucleation. To further verify this hypothesis, we did *in situ* TEM stress relaxation experiments and additional related atomic simulations.

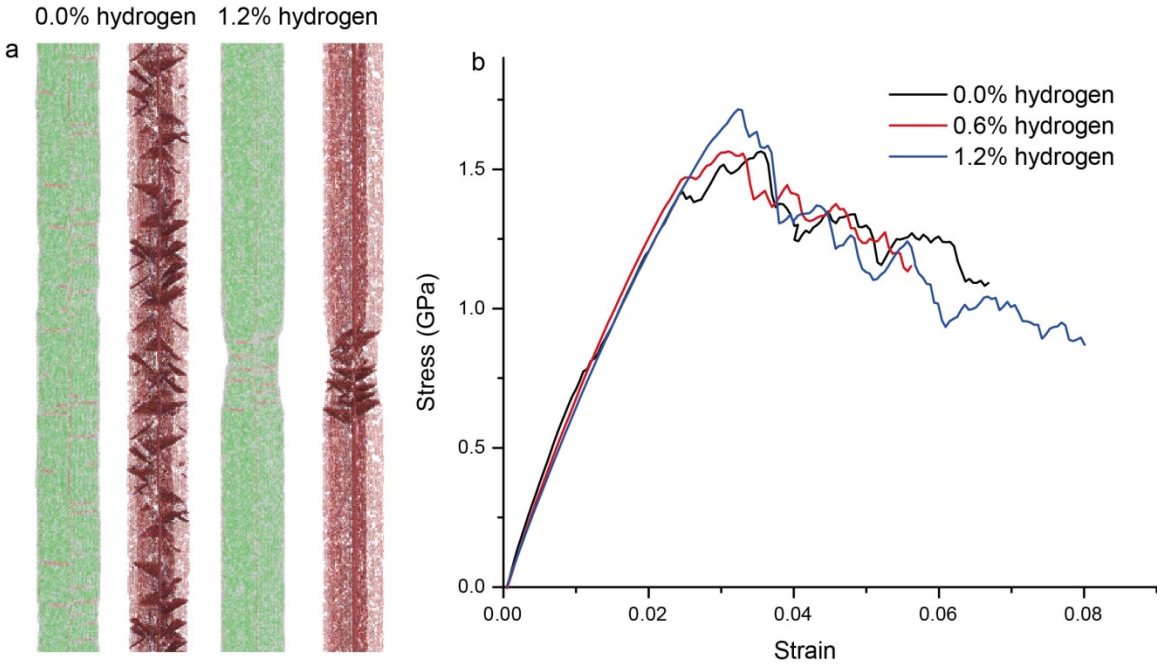

Figure 5.2 | MD simulation of tensile testing. a, Distributed plasticiy without hydrogen transition to localized plasticity with hydrogen in MD simulation. **b,** Stress-strain curves of penta-twinned NWs with different concentration of hydrogen.

5.3. Stress-relaxation Testing

5.3.1. *In-situ* TEM stress relaxation testing

Our previous study in Chapter 3 discovered an unusual dislocation-based stress relaxation and strain recovery behavior in penta-twined Ag NWs by *in-situ* TEM/SEM tensile testing and MD simulations(66). It has been corroborated that the stress relaxation is governed by the nucleation of surface dislocations. To further illustrate the effect of hydrogen on surface dislocation nucleation, Dr. Guangming performed similar *in situ* stress relaxation experiments on NWs charged by hydrogen. Stress relaxation experiments were conducted by loading the actuator to a given displacement and then, while the actuator displacement was held constant, the specimen was relaxed as a function of time. Since the experiment was not under true displacement control, the load on the specimen decreased and the specimen elongation increased at the same time.

Figure 5.3a-c shows the stress–strain response during typical tensile tests of three penta-twinned Ag NWs with different concentrations of H inside (charging time, 0, 24 and 48 hrs.) in four steps: loading, relaxation, unloading and recovery. During the loading step, all three NWs exhibited nearly linear responses (slightly nonlinear when the applied stress is high). During the relaxation step, the stress decreased with time, while the strain increased; the relaxation magnitude decreased with increasing hydrogen inside the NWs. Figure 5.4a-c shows the strain and stress as functions of time for the three NWs at stress levels close to the yield strength. For the as-received NWs, when the initial stress is 0.91GPa, the NW strain increases monotonically with time from 1.20 to 1.46%, and the stress decreases monotonically from 0.91 to 0.79GPa. For the 24-hr hydrogen-charged

sample, the stress decreases from 0.94 to 0.87GPa and the strain increases from 1.23 to 1.34%. For the 48-hr hydrogen-charged sample, the stress decreases from 1.11 to 1.09GPa and the strain increases from 1.41 to 1.45%, and almost negligible relaxation can be observed. The stress relaxation is obviously attenuated as the hydrogen concentration increases. Since the stress relaxation is due to dislocation nucleation, the attenuated stress relaxation suggests that the presence of hydrogen suppresses surface dislocation nucleation in the penta-twinned NWs.

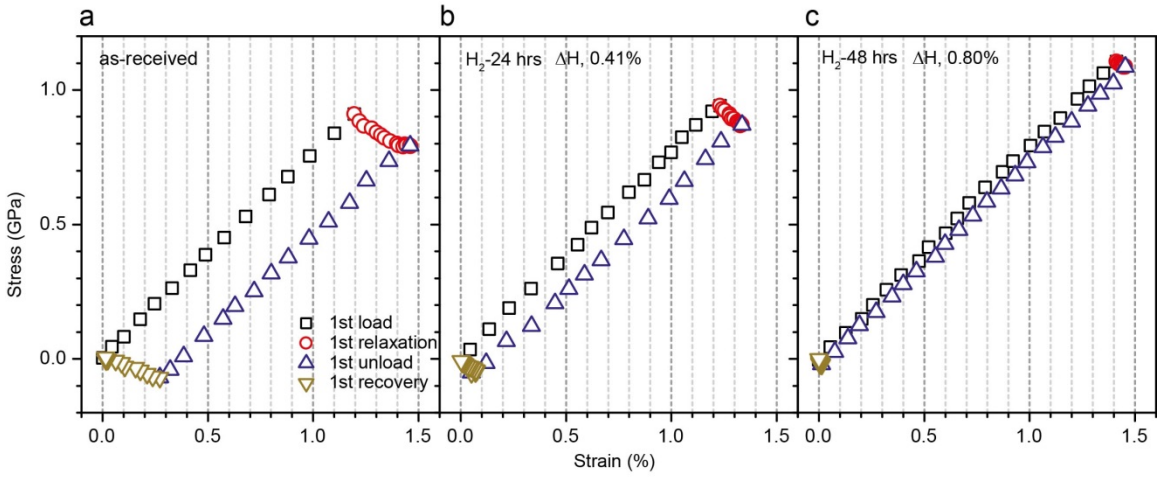

Figure 5.3 | *In-situ* TEM stress relaxation tests. a-c, Stress-strain curves of stress relaxation tests for a penta-twinned Ag NW with different concentrations of hydrogen. (Courtesy of Prof. Yong Zhu and Dr.Guangming Chen)

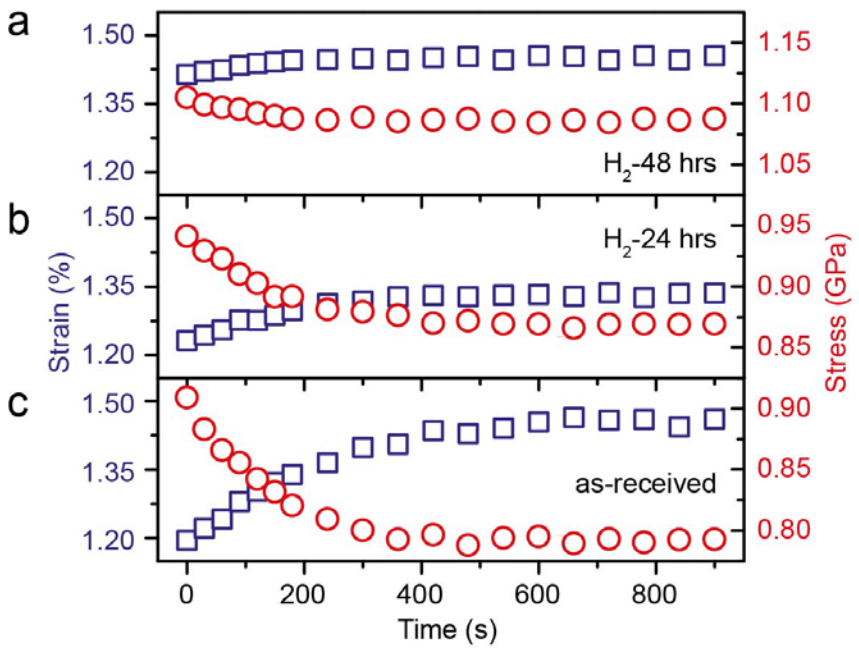

Figure 5.4 | *In-situ* TEM stress relaxation results. a-c, Relaxation curves for a penta-twinned Ag NW with different hydrogen concentrations. (Courtesy of Prof. Yong Zhu and Dr.Guangming Chen)

5.3.2. MD simulation of stress relaxation

To further support the hypothesis that hydrogen can suppress surface dislocation nucleation, atomic simulations similar to the *in situ* stress relaxation were carried out with artificial vacancies as initial defects that promote dislocation nucleation. Different concentrations of hydrogen were inserted into the NW samples, ranging from 0% to 1%. To mimic stress relaxation behaviors, I first stretched the simulated samples to a constant stress and then monitored stress relaxation while the applied strain was fixed. The simulation results show a significant stress relaxation during several nanoseconds in a hydrogen-free NW (Black curve in Fig. 5.5). The inset in Fig. 5.5 represents the final

atomic configuration of NWs after relaxation. Stacking faults can be observed in the NWs with zero or low hydrogen concentrations. The discrete stress drops in the stress relaxation profile correspond to the partial dislocation nucleation events. With hydrogen introduced into the penta-twinned NWs, there is clearly a decrease and delay in stress drops during relaxation, and fewer dislocations are observed, as illustrated in Fig. 5.5. When the hydrogen concentration further increases, no stress relaxation and dislocation nucleation can be observed within the simulation time scale (Purple and green curves in Fig. 5.5). The atomic simulation results clearly show that the presence of hydrogen will delay and suppress dislocation nucleation in penta-twinned NWs. Similar stress relaxation simulations were also performed on a penta-twinned NW with a surface notch instead of vacancies. Hydrogen was found to accumulate around the surface notch and suppress dislocation nucleation from the notch tip, which is similar to previous crack tip simulations (154).

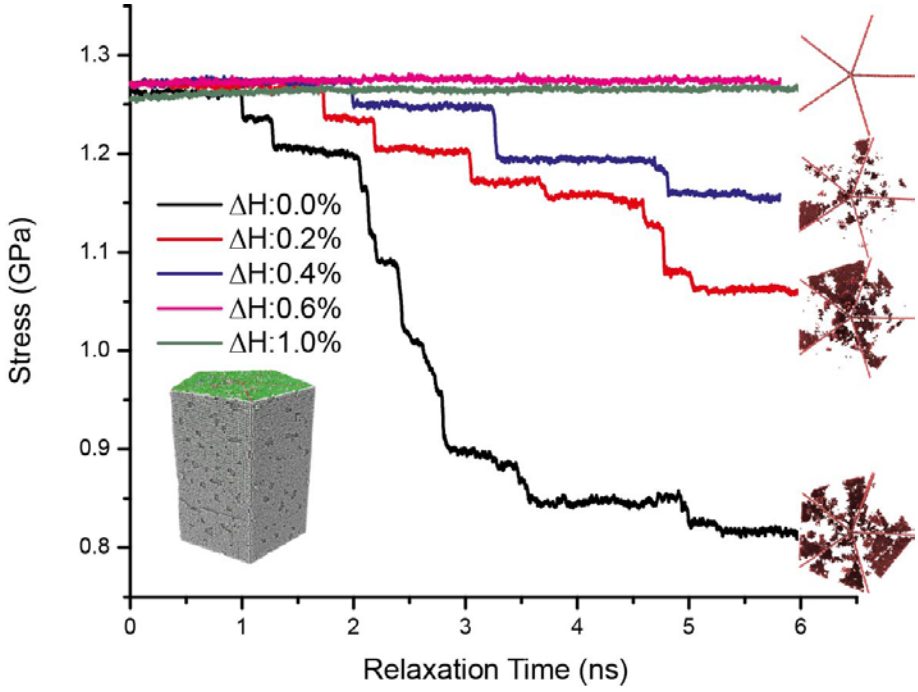

Figure 5.5 | MD simulations of stress relaxation. Relaxation curves for a penta-twinned Ag NW with different hydrogen concentrations.

5.3.3. Dislocation nucleation from surface ledges

In the above stress relaxation simulations, pre-existing defects were introduced as uniformly distributed vacancies in the NWs or as a single surface notch. It is shown that hydrogen can effectively diffuse into the vacancy sites or accumulate around the notch tip and significantly suppress dislocation nucleation. In addition to the vacancy defects, surface steps and roughness were thought to be the preferred sites for dislocation nucleation in NWs (73, 159, 161-163). Below, by using a simplified atomic model, I further show that hydrogen can increase the activation energy for surface dislocation nucleation and suppress dislocation nucleation.

In the experiments, the axis direction of tested NWs is <110> and the free surface of the NWs is (001). To model the dislocation nucleation from a NW surface with roughness, I constructed a simplified 2D model, as shown in the inset in Fig. 5.6e. The tensile direction <110> and the out-of-plane direction $< 1\bar{1}0 >$ are periodic. Surface roughness, represented by several surface ledges, was applied on the (001) free surface. The three different kinds of ledges are preferred nucleation sites for surface dislocation with different priorities. To avoid limitations from the diffusion timescale in the simulation, hydrogen atoms were directly inserted into the interstitial sites right next to the surface ledge. The green stars in Fig. 5.6a-d represent the positions of the hydrogen atoms, and the dislocation nucleation sites in the succeeding deformation are also shown. Figure 5.6e shows the stress-strain curves of different cases corresponding to different hydrogen positions and dislocation nucleation sites in Fig. 5.6b-d. The dislocation prefers to nucleate at the inner ledge at a strain of 4.68% without hydrogen (Fig. 5.6a). When the easiest ledge for surface nucleation is charged with hydrogen, nucleation from that ledge will be suppressed (Fig. 5.6b). Critical strain for nucleation is delayed to 5.29%, and nucleation occurs at the neighboring ledges (Fig. 5.6b). Continued charging of hydrogen will further suppress the dislocation nucleation from the surface ledges (Fig. 5.6c-d), and finally, when all the ledges are charged with hydrogen, the critical nucleation strain is increased to 6.54% and the nucleation site is on the flat surface but close to the inner surface ledge (Fig. 5.6d). The increment critical strain for dislocation nucleation and the change to the initial dislocation nucleation sites that is due to the hydrogen clearly suggest that hydrogen atoms around the surface ledge can suppress dislocation nucleation.

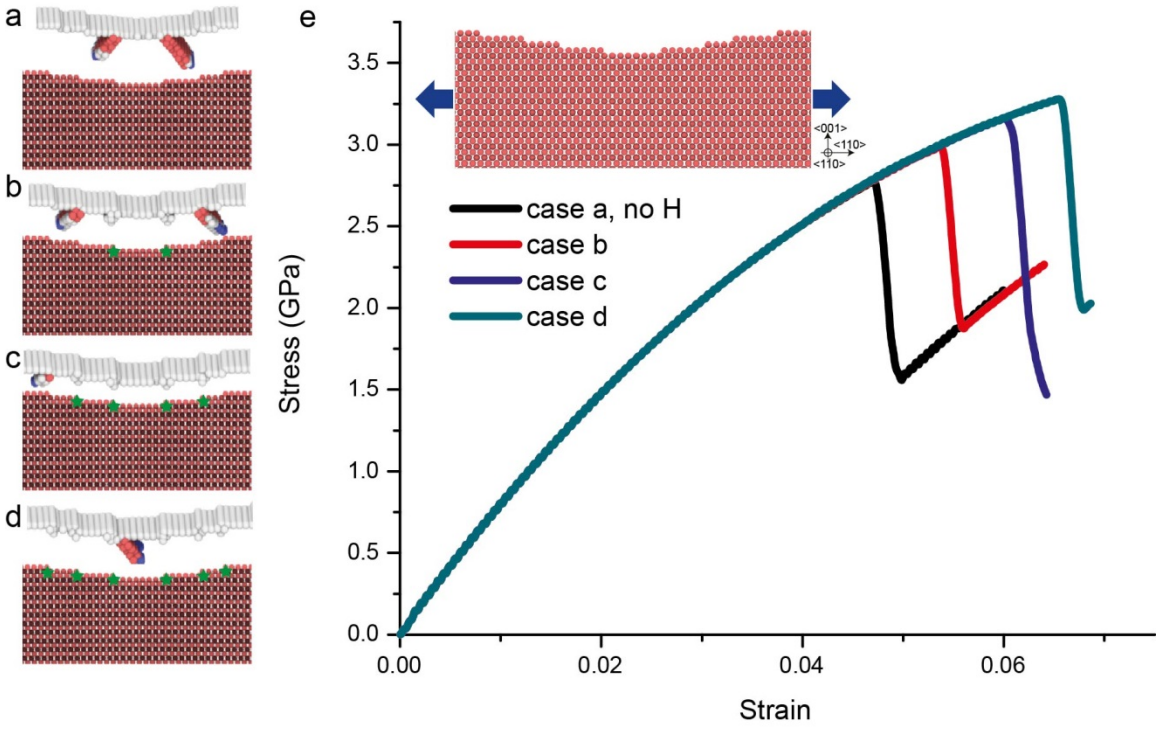

Figure 5.6 | MD simulations of dislocation nucleation. a-c, Upper parts of the figure show the dislocation nucleation sites. Green stars in the lower part of the figures indicate the hydrogen positions. **e,** Stress-curves of different cases correspond to configurations (**a-d**).

To quantify the activation energy changes of the surface dislocation nucleation from the ledge that are due to hydrogen, the climbing image nudged elastic band method (CINEB)(10, 73, 164) was applied to the hydrogen-free case and case (d), as showed in Fig. 5.7. See method in part **5.4.1** for details of the simulation. In Fig. 5.7, I show the calculated activation energies of two different samples at different stresses; the solid lines represent fitting curves by taking the functional form $Q_0(\sigma)=A(1-\sigma/\sigma_{th})^{\alpha}$. I get A=31.3eV, α=1.46, σ_{th}=2.8GPa for the hydrogen-free sample and A=99eV, α=1.44, σ_{th}=3.3GPa for hydrogen charged case (d). The CINEB results in Fig. 5.7 indicate that the activation

energy curve of the hydrogen-charged sample is significantly shifted to the right side. The activation energy for dislocation nucleation at a certain stress increases significantly due to the hydrogen; for example, at a tensile stress of 2.8 GPa, the activation energy in case (d) increases at least 5 eV. In the above simulations, hydrogen atoms were inserted right next to the ledges and occupied all the possible interstitial sites in the periodic out-of-plane direction. Additional simulations found that when hydrogen was within 2nm of surface ledges and even partially occupied the interstitial sites, it could still suppress dislocation nucleation effectively. Atomic simulations of stress relaxation and dislocation nucleation with surface roughness further reveal that hydrogen can increase the activation energy of nucleation and suppress surface dislocation nucleation in the NWs. This effect of hydrogen will change the mechanical properties of NWs, leading to an enhanced yield strength and, finally, a more localized necking failure.

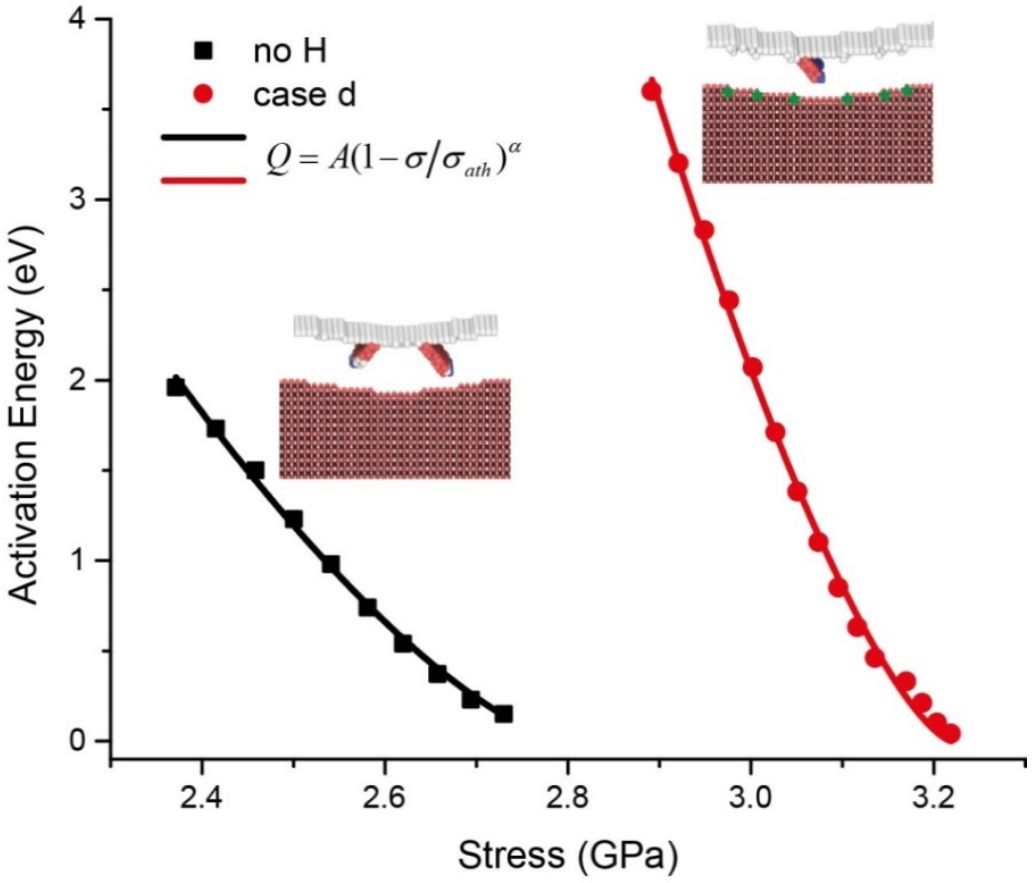

Figure 5.7 | Stress-dependent activation energy of dislocation nucleation. Black squares correspond to case (a) without hydrogen; Red dots correspond to case (d). Solid lines are the fitting curves.

5.4. Discussion

5.4.1. Method of atomic simulations in 5.2 & 5.3.

Tensile testing: The penta-twinned NW samples were 15 nm in diameter and 80 nm in length. Then, 1.2% of Ag atoms were randomly removed from the samples to introduce vacancies. Hydrogen atoms were inserted into the octahedral sites in the whole NW samples at random. The samples were initially relaxed and equilibrated at an elevated

temperature of 800 K (approximately 65% of the melting point of Ag) for 500 ps using the Nosé-Hoover thermostat (38). Periodic boundary conditions were imposed along the axial direction. During loading, the samples were stretched at a constant strain rate of 10^6/s under NVT ensemble.

Stress Relaxation: The penta-twinned NW samples were 24 nm in diameter and 30 nm in length. Then, 1.0% of Ag atoms were randomly removed from the samples to introduce vacancies. Hydrogen atoms were inserted into the octahedral sites in the whole NW samples at random. The samples were initially relaxed and equilibrated at an elevated temperature of 800 K for 500 ps using the Nosé-Hoover thermostat. Periodic boundary conditions were imposed along the axial direction. The samples were first stretched to a certain stress at a constant strain rate of 10^8/s, and then relaxed for several nanoseconds under NVT ensemble while holding the strain fixed. During the relaxation process, I monitored the variation of the axial stress by averaging the Virial stresses over all atoms in the samples.

Nucleation on ledges & NEB calculation: The simulation box was oriented along x-[110], y-[001], z-[$\bar{1}$10], with dimensions of 26 nmx50 nmx10 nm. Periodic boundary conditions were applied in the x and z direction. Hydrogen atoms were inserted into octahedral sites in the designated positions. The system was initially relaxed and equilibrated at temperature of 5 K for 500 ps using the Nosé-Hoover thermostat and then tensile loading was applied in the x direction at a strain rate of 10^8/s under NVT ensemble. For NEB calculation, the initial images were the system with no dislocation at different stresses. The final images were created by a remap of the system with a dislocation embryo to the corresponding strain and minimized so that the system energy

is only 0.01 eV lower than the corresponding initial image. During the NEB calculation, 60 replicas were used and the final image with the dislocation embryo was fixed.

5.5. Summary

In this chapter, we have studied hydrogen embrittlement in a nanoscale system and discovered a transition between distributed plasticity and localized necking in penta-twinned Ag NWs by an integrated approach that combines *in situ* TEM tensile testing, microstructure characterization and MD simulations. In contrast to previous studies of hydrogen embrittlement in bulk systems, the effect of hydrogen on nanoscale systems, especially NWs with large surface/volume ratios, are related to the nucleation of dislocation. *In situ* TEM tensile testing and MD simulations capture a clear transition of the failure mode from distributed plasticity to localized necking. The ultimate strength of the NW increases significantly with the diffusion of more hydrogen. Further *in situ* TEM relaxation tests and simulations show that the unique stress relaxation behavior in penta-twinned NWs that is dominated by dislocation nucleation will be attenuated as the hydrogen concentration increases. These results suggest that hydrogen can suppress dislocation nucleation in NWs. CINEB simulations further quantify that hydrogen can increase the activation energy for the dislocation nucleation from single-atom surface ledges. Therefore, in contrast to previous studies in bulk materials showing that hydrogen was attributed to the effect of dislocation movement and multiplication, the present study reveals that hydrogen can affect nanostructures that are dominated by a dislocation-nucleation-controlled deformation mechanism and can alter their mechanical properties.

Our study provides new insight into hydrogen embrittlement mechanisms in nanostructure materials.

Chapter 6 Conclusions and Perspectives

6.1. Concluding remarks

Using FEM, atomistic simulations and continuum models, I have investigated the nanotwin-governed toughening mechanism in hierarchically structured biological materials. Different deformation mechanisms in NWs, such as recoverable plasticity in penta-twinned NW, tensile-detwinning in bi-twinned NW and hydrogen embrittlement in penta-twinned NWs were explored and explained by MD simulations. The scientific findings for each chapter are summarized as follows.

In Chapter 2, *in-situ* experiments clearly indicate that nanoscale growth twins in *Strombus gigas* conch shell play a critical role in the mechanical properties of the material. The CTOD *in-situ* tests combined with our FEM modeling quantify the fracture resistance in twinned conch shell and single crystalline aragonite. The results from our atomistic and cohesive FEM simulations demonstrate that TBs can act as effective obstacles to crack propagation, leading to crack blunting and delocalization of deformation, which facilitates energy dissipation and delays catastrophic crack propagation. Atomic simulations also revealed that there exists a phase transformation region near the crack tip in the twinned aragonite sample while the transformation in single crystalline aragonite is very limited. Detail HRTEM examination of crack tips in twinned conch shell and single crystalline aragonite further confirm this. Self-similar hierarchical model indicates that the lowest-level structure plays a crucial role in increasing the overall toughness of the conch-like material by driving energy dissipation

in the organic matrix at all upper levels. In summary, these findings provide a fundamental understanding of the contribution of hard basic building blocks at nanoscale to fracture resistance of the overall structure, which complement our previous knowledge about the roles of soft organic content and bio-composite structure in the toughness of bio-materials.

In Chapter 3, I have explored an unusual dislocation-based stress relaxation and strain recovery behaviour in penta-twinned Ag NWs. This behavior consists of two facets: stress relaxation under an applied strain and complete plastic strain recovery upon unloading. Using MD simulations, I found that stress relaxation originates from the nucleation of leading partial dislocations, while the complete strain recovery is due to the reverse motion of partial dislocations driven by the repulsive force from the TBs and the intrinsic stress field due to the penta twin structure. The TEM microstructural characterizations further confirm this mechanism found by MD simulations. The simulations also demonstrate that the TBs play a crucial role in the observed phenomenon in penta-twinned NWs, as bi-crystalline NWs with a single TB exhibit a similar behaviour while single-crystalline NWs and bi-crystalline NWs with other types of GBs do not. It is noted that diffusion and sliding processes associated with GBs should be suppressed in penta-twinned NWs. Therefore, in contrast to previous studies in nanocrystalline metals due to a cooperation of dislocation- and GB- mediated processes; the present study demonstrates a new type of stress relaxation and full plastic strain recovery induced by TB-dislocation interactions. Our study opens up a promising prospect of designing one-dimensional nanostructures with time-dependent strain recovery capabilities.

In Chapter 4, *in-situ* TEM tensile testing discovered a transition between two deformation modes, dislocation slip and tensile detwinning, in bi-twinned FCC metallic NWs. Using MD simulations, I revealed the detail deformation mechanism in this two deformation modes and found a novel two-step tensile detwinning mechanism in bi-twinned NWs. The unusual tensile detwinning mechanism starts with detwinning of the existing TB under no resolved shear stress, followed by propagation of newly formed TB and grain boundary leading to superplastic deformation. A criterion for the detwinning deformation was proposed based on the detwinning energy barrier, which was shown capable of capturing the effects of the volume ratio and cross-sectional aspect ratio on the transition of deformation modes in bi-twinned NWs. This study improved our understanding of the relationship between microstructure and deformation mechanisms in NWs.

In Chapter 5, we have studied the hydrogen embrittlement in a nanoscale system and discovered a transition between distributed plasticity and localized necking in penta-twinned Ag NWs by an integrated approach that combines *in situ* TEM tensile testing, microstructure characterization and MD simulations. In contrast to previous studies of hydrogen embrittlement in bulk systems, the effect of hydrogen on nanoscale systems, especially NWs with large surface/volume ratios, are related to the nucleation of dislocation. *In situ* TEM tensile testing and MD simulations capture a clear transition of the failure mode from distributed plasticity to localized necking. The ultimate strength of the NW increases significantly with the diffusion of more hydrogen. Further *in situ* TEM relaxation tests and simulations showed that the unique stress relaxation behavior in penta-twinned NWs that is dominated by dislocation nucleation will be attenuated as the

hydrogen concentration increases. These results suggest that hydrogen can suppress dislocation nucleation in NWs. CINEB simulations further quantify that hydrogen can increase the activation energy for the dislocation nucleation from single-atom surface ledges. Therefore, in contrast to previous studies in bulk materials showing that hydrogen was attributed to the effect of dislocation movement and multiplication, the present study reveals that hydrogen can affect nanostructures that dominated by dislocation-nucleation-controlled deformation mechanism and can alter their mechanical properties. This study provides new insight into hydrogen embrittlement mechanisms in nanostructure materials.

6.2. Outlook of future research

Recent experimental and computational studies have demonstrated that nanoscale twins can effectively enhance the mechanical and physical properties in different material systems. The deformation mechanisms of nanotwinned biomaterial (aragonite) and nanowires with different twinned structure were discussed in current thesis. However, there are still many interesting open questions in the studies of nanotwinned materials, a few of which are listed below.

(1) Intensive experiments and modeling have been focused on NT metals; however, for nanotwinned ceramic, although showing outstanding mechanical properties, there have been very few *in situ* experiments studies on its deformation and fracture mechanisms. Currently understanding of deformation mechanisms in nanotwinned ceramics are primarily based on *ab initio* calculations of very small samples under idealized loading conditions and without accounting for any temperature effects.

Size effect, temperature effect and real time observation are all needed to be accounted in the future's experiment studies. Large scale simulation with more accurate interatomic potential for ceramics is also necessary.

(2) Hierarchical twin structures can be introduce to system by pre-torsion deformation(165). Directly synthesis similar twins to bio-mimic hierarchical structure would be challenging but may further enhance the properties of nanotwinned metals.

(3) Gradient grain material can also provide good combinations of strength and ductility(166). If nanotwinned structures can be combined with gradient grains, there is some possibility to further push the limit of strength and ductility of the metal materials.

(4) Surface dislocation nucleation is thought to be the dominate mechanism in nanostructures. Recent *in-situ* experiments reveal that the first measurable inelastic event (dislocation nucleation) might be of a hybrid diffusive–displacive nature(160, 167). How to use simulation tools to study the origin of dislocation nucleation is an interesting challenge.

(5) In Chapter 4.5, I discussed the decouple detwinning mechanism in bi-twinned NWs in simulations, whether this mechanism can be applied to other kind of twinned NWs or can I decouple the detwinning mechanism in experiments is also challenging.

Bibliography

1. Lu L, Chen X, Huang X, & Lu K (2009) Revealing the maximum strength in nanotwinned copper. *Science* 323(5914):607-610.
2. Lu L, Shen Y, Chen X, Qian L, & Lu K (2004) Ultrahigh strength and high electrical conductivity in copper. *Science* 304(5669):422-426.
3. Lu K, Lu L, & Suresh S (2009) Strengthening materials by engineering coherent internal boundaries at the nanoscale. *Science* 324(5925):349-352.
4. Li X, Wei Y, Lu L, Lu K, & Gao H (2010) Dislocation nucleation governed softening and maximum strength in nano-twinned metals. *Nature* 464(7290):877-880.
5. Stukowski A, Albe K, & Farkas D (2010) Nanotwinned fcc metals: Strengthening versus softening mechanisms. *Physical Review B* 82(22):224103.
6. You Z*, et al.* (2013) Plastic anisotropy and associated deformation mechanisms in nanotwinned metals. *Acta Materialia* 61(1):217-227.
7. Cao A & Wei Y (2007) Molecular dynamics simulation of plastic deformation of nanotwinned copper. *Journal of Applied Physics* 102(8):083511.
8. Frøseth A, Derlet P, & Van Swygenhoven H (2004) Grown-in twin boundaries affecting deformation mechanisms in nc-metals. *Applied physics letters* 85(24):5863-5865.
9. Li L & Ghoniem NM (2009) Twin-size effects on the deformation of nanotwinned copper. *Physical Review B* 79(7):075444.
10. Zhu T, Li J, Samanta A, Kim HG, & Suresh S (2007) Interfacial plasticity governs strain rate sensitivity and ductility in nanostructured metals. *Proceedings of the National Academy of Sciences* 104(9):3031-3036.
11. Chen Z, Jin Z, & Gao H (2007) Repulsive force between screw dislocation and coherent twin boundary in aluminum and copper. *Physical Review B* 75(21):212104.
12. Wu Z, Zhang Y, & Srolovitz D (2009) Dislocation–twin interaction mechanisms for ultrahigh strength and ductility in nanotwinned metals. *Acta Materialia* 57(15):4508-4518.
13. Zheng Y, Lu J, Zhang H, & Chen Z (2009) Strengthening and toughening by interface-mediated slip transfer reaction in nanotwinned copper. *Scripta Materialia* 60(7):508-511.
14. Jin Z-H*, et al.* (2006) The interaction mechanism of screw dislocations with coherent twin boundaries in different face-centred cubic metals. *Scripta Materialia* 54(6):1163-1168.
15. Qin E, Lu L, Tao N, Tan J, & Lu K (2009) Enhanced fracture toughness and strength in bulk nanocrystalline Cu with nanoscale twin bundles. *Acta Materialia* 57(20):6215-6225.
16. Singh A, Tang L, Dao M, Lu L, & Suresh S (2011) Fracture toughness and fatigue crack growth characteristics of nanotwinned copper. *Acta Materialia* 59(6):2437-2446.

17. Jang D, Cai C, & Greer JR (2011) Influence of homogeneous interfaces on the strength of 500 nm diameter Cu nanopillars. *Nano letters* 11(4):1743-1746.
18. Kim S-W, Li X, Gao H, & Kumar S (2012) In situ observations of crack arrest and bridging by nanoscale twins in copper thin films. *Acta Materialia* 60(6):2959-2972.
19. Tian Y, *et al.* (2013) Ultrahard nanotwinned cubic boron nitride. *Nature* 493(7432):385-388.
20. Li X, Yin S, Oh SH, & Gao H (2017) Hardening and toughening mechanisms in nanotwinned ceramics. *Scripta Materialia* 133:105-112.
21. Fu X, Jiang J, Liu C, & Yuan J (2009) Fivefold twinned boron carbide nanowires. *Nanotechnology* 20(36):365707.
22. Zheng S, *et al.* (2016) Structure and energetics of nanotwins in cubic boron nitrides. *Applied Physics Letters* 109(8):081901.
23. Huang Q, *et al.* (2014) Nanotwinned diamond with unprecedented hardness and stability. *Nature* 510(7504):250-253.
24. Liu X, *et al.* (2016) Ultrahard stitching of nanotwinned diamond and cubic boron nitride in C2-BN composite. *Sci Rep-Uk* 6.
25. Xie KY, *et al.* (2015) Atomic-level understanding of "asymmetric twins" in boron carbide. *Physical review letters* 115(17):175501.
26. An Q, *et al.* (2016) Superstrength through Nanotwinning. *Nano letters* 16(12):7573-7579.
27. An Q, *et al.* (2016) Nucleation of amorphous shear bands at nanotwins in boron suboxide. *Nature communications* 7.
28. Shin YA, *et al.* (2016) Nanotwin-governed toughening mechanism in hierarchically structured biological materials. *Nature communications* 7.
29. Lieber CM & Wang ZL (2007) Functional nanowires. *Mrs Bull* 32(02):99-108.
30. Xia Y, *et al.* (2003) One‐dimensional nanostructures: synthesis, characterization, and applications. *Adv Mater* 15(5):353-389.
31. Greer JR & De Hosson JTM (2011) Plasticity in small-sized metallic systems: Intrinsic versus extrinsic size effect. *Progress in Materials Science* 56(6):654-724.
32. Richter G, *et al.* (2009) Ultrahigh strength single crystalline nanowhiskers grown by physical vapor deposition. *Nano letters* 9(8):3048-3052.
33. Zhu T & Li J (2010) Ultra-strength materials. *Progress in Materials Science* 55(7):710-757.
34. Jang D, Li X, Gao H, & Greer JR (2012) Deformation mechanisms in nanotwinned metal nanopillars. *Nature Nanotechnology* 7(9):594-601.
35. Wang J, *et al.* (2013) Near-ideal theoretical strength in gold nanowires containing angstrom scale twins. *Nature communications* 4:1742.
36. Zhu Y, *et al.* (2012) Size effects on elasticity, yielding, and fracture of silver nanowires: In situ experiments. *Physical Review B* 85(4).
37. Berendsen HJ, Postma Jv, van Gunsteren WF, DiNola A, & Haak J (1984) Molecular dynamics with coupling to an external bath. *The Journal of chemical physics* 81(8):3684-3690.

38. Nose S (1984) A Unified Formulation of the Constant Temperature Molecular-Dynamics Methods. *J Chem Phys* 81(1):511-519.
39. Schneider T & Stoll E (1978) Molecular-dynamics study of a three-dimensional one-component model for distortive phase transitions. *Physical Review B* 17(3):1302.
40. Andersen HC (1980) Molecular dynamics simulations at constant pressure and/or temperature. *The Journal of chemical physics* 72(4):2384-2393.
41. Parrinello M & Rahman A (1981) Polymorphic transitions in single crystals: A new molecular dynamics method. *Journal of Applied physics* 52(12):7182-7190.
42. Plimpton S (1995) Fast Parallel Algorithms for Short-Range Molecular-Dynamics. *J Comput Phys* 117(1):1-19.
43. MUTVEI H (1978) Ultrastructural characteristics of the nacre in some gastropods. *Zoologica Scripta* 7(1 - 4):287-296.
44. Suzuki M, Kim H, Mukai H, Nagasawa H, & Kogure T (2012) Quantitative XRD analysis of {110} twin density in biotic aragonites. *Journal of structural biology* 180(3):458-468.
45. Espinosa HD*, et al.* (2011) Tablet-level origin of toughening in abalone shells and translation to synthetic composite materials. *Nature communications* 2:173.
46. Gao H, Ji B, Jäger IL, Arzt E, & Fratzl P (2003) Materials become insensitive to flaws at nanoscale: lessons from nature. *Proceedings of the National Academy of Sciences* 100(10):5597-5600.
47. Kamat S, Su X, Ballarini R, & Heuer A (2000) Structural basis for the fracture toughness of the shell of the conch Strombus gigas. *Nature* 405(6790):1036-1040.
48. Mayer G (2005) Rigid biological systems as models for synthetic composites. *Science* 310(5751):1144-1147.
49. Meyers MA, Chen P-Y, Lin AY-M, & Seki Y (2008) Biological materials: structure and mechanical properties. *Progress in Materials Science* 53(1):1-206.
50. Ortiz C & Boyce MC (2008) Bioinspired structural materials. *Science* 319(5866):1053-1054.
51. Smith BL*, et al.* (1999) Molecular mechanistic origin of the toughness of natural adhesives, fibres and composites. *Nature* 399(6738):761-763.
52. Lakes R (1993) Materials with structural hierarchy. *Nature* 361(6412):511-515.
53. Kamat S, Kessler H, Ballarini R, Nassirou M, & Heuer AH (2004) Fracture mechanisms of the Strombus gigas conch shell: II-micromechanics analyses of multiple cracking and large-scale crack bridging. *Acta Materialia* 52(8):2395-2406.
54. Menig R, Meyers M, Meyers M, & Vecchio K (2001) Quasi-static and dynamic mechanical response of Strombus gigas (conch) shells. *Materials Science and Engineering: A* 297(1):203-211.

55. Schwalbe K-H, Newman JC, & Shannon JL (2005) Fracture mechanics testing on specimens with low constraint––standardisation activities within ISO and ASTM. *Engineering Fracture Mechanics* 72(4):557-576.
56. Xiao S, Edwards SA, & Gräter F (2011) A new transferable forcefield for simulating the mechanics of CaCO3 crystals. *The Journal of Physical Chemistry C* 115(41):20067-20075.
57. Stukowski A (2010) Visualization and analysis of atomistic simulation data with OVITO-the Open Visualization Tool. *Model Simul Mater Sc* 18(1).
58. Freund LB (1998) *Dynamic fracture mechanics* (Cambridge university press).
59. Archer T*, et al.* (2003) An interatomic potential model for carbonates allowing for polarization effects. *Phys Chem Miner* 30(7):416-424.
60. Pavese A, Catti M, Price G, & Jackson R (1992) Interatomic potentials for CaCO 3 polymorphs (calcite and aragonite), fitted to elastic and vibrational data. *Phys Chem Miner* 19(2):80-87.
61. Gao H (2006) Application of fracture mechanics concepts to hierarchical biomechanics of bone and bone-like materials. *International Journal of Fracture* 138(1-4):101.
62. Yao H & Gao H (2008) Reprint of "Multi-scale cohesive laws in hierarchical materials"[In. J. Solids Struct. 44 (2007) 8177–8193]. *International Journal of Solids and Structures* 45(13):3627-3643.
63. Zhang Z, Zhang Y-W, & Gao H (2011) On optimal hierarchy of load-bearing biological materials. *Proceedings of the Royal Society of London B: Biological Sciences* 278(1705):519-525.
64. Bechtle S, Ang SF, & Schneider GA (2010) On the mechanical properties of hierarchically structured biological materials. *Biomaterials* 31(25):6378-6385.
65. Sen D & Buehler MJ (2011) Structural hierarchies define toughness and defect-tolerance despite simple and mechanically inferior brittle building blocks. *Sci Rep-Uk* 1:35.
66. Qin Q*, et al.* (2015) Recoverable plasticity in penta-twinned metallic nanowires governed by dislocation nucleation and retraction. *Nature communications* 6.
67. Lu Y, Huang JY, Wang C, Sun S, & Lou J (2010) Cold welding of ultrathin gold nanowires. *Nature Nanotechnology* 5(3):218-224.
68. Park HS, Gall K, & Zimmerman JA (2005) Shape memory and pseudoelasticity in metal nanowires. *Physical Review Letters* 95(25):255504.
69. Park HS, Gall K, & Zimmerman JA (2006) Deformation of FCC nanowires by twinning and slip. *J Mech Phys Solids* 54(9):1862-1881.
70. Weinberger CR & Cai W (2012) Plasticity of metal nanowires. *Journal of Materials Chemistry* 22(8):3277-3292.
71. Yue Y*, et al.* (2012) Quantitative evidence of crossover toward partial dislocation mediated plasticity in copper single crystalline nanowires. *Nano letters* 12(8):4045-4049.
72. Zheng H*, et al.* (2010) Discrete plasticity in sub-10-nm-sized gold crystals. *Nature communications* 1:144.

73. Zhu T, Li J, Samanta A, Leach A, & Gall K (2008) Temperature and strain-rate dependence of surface dislocation nucleation. *Physical Review Letters* 100(2):025502.
74. Deng C & Sansoz F (2009) Fundamental differences in the plasticity of periodically twinned nanowires in Au, Ag, Al, Cu, Pb and Ni. *Acta Materialia* 57(20):6090-6101.
75. Filleter T*, et al.* (2012) Nucleation‐Controlled Distributed Plasticity in Penta‐twinned Silver Nanowires. *Small* 8(19):2986-2993.
76. Lu Y, Song J, Huang JY, & Lou J (2011) Fracture of Sub‐20nm Ultrathin Gold Nanowires. *Advanced Functional Materials* 21(20):3982-3989.
77. Zhu Y*, et al.* (2012) Size effects on elasticity, yielding, and fracture of silver nanowires: In situ experiments. *Physical Review B* 85(4):045443.
78. Baker SP, Vinci RP, & Arias T (2002) Elastic and anelastic behavior of materials in small dimensions. *MRS Bulletin-Materials Research Society* 27(1):26-29.
79. Choi D-h, Kim H, & Nix WD (2004) Anelasticity and damping of thin aluminum films on silicon substrates. *Microelectromechanical Systems, Journal of* 13(2):230-237.
80. Haque M & Saif M (2005) Thermo-mechanical properties of nano-scale freestanding aluminum films. *Thin Solid Films* 484(1):364-368.
81. Karanjgaokar N, Oh C-S, Lambros J, & Chasiotis I (2012) Inelastic deformation of nanocrystalline Au thin films as a function of temperature and strain rate. *Acta Materialia* 60(13):5352-5361.
82. Lang M*, et al.* (1999) Measurement of elastic and anelastic properties of nanocrystalline metals. *Nanostruct Mater* 12(5):811-816.
83. Chen B*, et al.* (2013) Anelastic Behavior in GaAs Semiconductor Nanowires. *Nano letters*.
84. Li X, Wei Y, Yang W, & Gao H (2009) Competing grain-boundary-and dislocation-mediated mechanisms in plastic strain recovery in nanocrystalline aluminum. *Proceedings of the National Academy of Sciences* 106(38):16108-16113.
85. Rajagopalan J, Han JH, & Saif MTA (2007) Plastic deformation recovery in freestanding nanocrystalline aluminum and gold thin films. *Science* 315(5820):1831-1834.
86. Wei X & Kysar JW (2011) Residual plastic strain recovery driven by grain boundary diffusion in nanocrystalline thin films. *Acta Materialia* 59(10):3937-3945.
87. Wei Y, Bower AF, & Gao H (2007) Recoverable creep deformation due to heterogeneous grain-boundary diffusion and sliding. *Scripta Materialia* 57(10):933-936.
88. Wei Y, Bower AF, & Gao H (2008) Recoverable creep deformation and transient local stress concentration due to heterogeneous grain-boundary diffusion and sliding in polycrystalline solids. *J Mech Phys Solids* 56(4):1460-1483.

89. Yamakov V, Wolf D, Phillpot SR, Mukherjee AK, & Gleiter H (2002) Dislocation processes in the deformation of nanocrystalline aluminium by molecular-dynamics simulation. *Nat Mater* 1(1):45-49.
90. Diao J, Gall K, & Dunn ML (2003) Surface-stress-induced phase transformation in metal nanowires. *Nat Mater* 2(10):656-660.
91. Liang W, Srolovitz DJ, & Zhou M (2007) A micromechanical continuum model for the tensile behavior of shape memory metal nanowires. *J Mech Phys Solids* 55(8):1729-1761.
92. Liang W & Zhou M (2006) Atomistic simulations reveal shape memory of fcc metal nanowires. *Physical Review B* 73(11):115409.
93. Qin Q & Zhu Y (2013) Temperature control in thermal microactuators with applications to in-situ nanomechanical testing. *Applied Physics Letters* 102(1):013101-013101-013105.
94. Zhu Y, Corigliano A, & Espinosa HD (2006) A thermal actuator for nanoscale in situ microscopy testing: design and characterization. *Journal of Micromechanics and Microengineering* 16(2):242.
95. Zhu Y & Espinosa HD (2005) An electromechanical material testing system for in situ electron microscopy and applications. *Proceedings of the National Academy of Sciences of the United States of America* 102(41):14503-14508.
96. Zhu Y, Moldovan N, & Espinosa HD (2005) A microelectromechanical load sensor for in situ electron and x-ray microscopy tensile testing of nanostructures. *Applied physics letters* 86(1):013506.
97. Williams P, Mishin Y, & Hamilton J (2006) An embedded-atom potential for the Cu–Ag system. *Model Simul Mater Sc* 14(5):817.
98. Tsai D (1979) The virial theorem and stress calculation in molecular dynamics. *The Journal of Chemical Physics* 70:1375.
99. Nowick AS (1972) *Anelastic relaxation in crystalline solids* (Elsevier).
100. Zener C (1948) *Elasticity and anelasticity of metals* (University of Chicago press).
101. Deng C & Sansoz F (2010) Repulsive force of twin boundary on curved dislocations and its role on the yielding of twinned nanowires. *Scripta Materialia* 63(1):50-53.
102. Wu JY, Nagao S, He JY, & Zhang ZL (2011) Role of five-fold twin boundary on the enhanced mechanical properties of fcc Fe nanowires. *Nano letters* 11(12):5264-5273.
103. Li JCM (1972) Disclination Model of High Angle Grain-Boundaries. *Surf Sci* 31(1):12-&.
104. Kang W & Saif MTA (2013) In Situ Study of Size and Temperature Dependent Brittle‐to‐Ductile Transition in Single Crystal Silicon. *Advanced Functional Materials* 23(6):713-719.
105. Oh SH, Legros M, Kiener D, & Dehm G (2009) In situ observation of dislocation nucleation and escape in a submicrometre aluminium single crystal. *Nat Mater* 8(2):95-100.

106. Qin Q, *et al.* (2015) Recoverable plasticity in penta-twinned metallic nanowires governed by dislocation nucleation and retraction. *Nature communications* 6:5983.
107. Zhu Y & Espinosa HD (2005) An electromechanical material testing system for in situ electron microscopy and applications. *Proceedings of the National Academy of Sciences of the United States of America* 102(41):14503-14508.
108. Chang T-H & Zhu Y (2013) A microelectromechanical system for thermomechanical testing of nanostructures. *Applied Physics Letters* 103(26):263114.
109. Anonymous (In bulk metallic materials, superplasticity typically refer to deformation over 200% during tensile deformation. Since NWs typically exhibit limited plasticity due to confined dislocation activities, a proportionally smaller deformation range is used to define superplasticity in NWs.
110. Sedlmayr A, *et al.* (2012) Existence of two twinning-mediated plastic deformation modes in Au nanowhiskers. *Acta Materialia* 60(9):3985-3993.
111. Seo J-H, *et al.* (2011) Superplastic Deformation of Defect-Free Au Nanowires via Coherent Twin Propagation. *Nano Letters* 11(8):3499-3502.
112. Williams PL, Mishin Y, & Hamilton JC (2006) An embedded-atom potential for the Cu-Ag system. *Modelling and Simulation in Materials Science and Engineering* 14(5):817-833.
113. Stukowski A (2010) Visualization and analysis of atomistic simulation data with OVITO-the Open Visualization Tool. *Modelling and Simulation in Materials Science and Engineering* 18(1):015012.
114. Zhu YT, *et al.* (2011) Dislocation–twin interactions in nanocrystalline fcc metals. *Acta Materialia* 59(2):812-821.
115. Hirth JP & Lothe J (1982) *Theory of dislocations* (John Wiley & Sons, New York) 2 nd Ed.
116. Wang J, *et al.* (2010) Detwinning mechanisms for growth twins in face-centered cubic metals. *Acta Materialia* 58(6):2262-2270.
117. Lee S, *et al.* (2014) Reversible cyclic deformation mechanism of gold nanowires by twinning–detwinning transition evidenced from in situ TEM. *Nature communications* 5:3033.
118. Zhou H, *et al.* (2015) Torsional Detwinning Domino in Nanotwinned One-Dimensional Nanostructures. *Nano letters* 15(9):6082-6087.
119. Wang YM, *et al.* (2013) Defective twin boundaries in nanotwinned metals. *Nat Mater* 12(8):697-702.
120. Louthan M, Caskey G, Donovan J, & Rawl D (1972) Hydrogen embrittlement of metals. *Materials Science and Engineering* 10:357-368.
121. Nagao A, Smith CD, Dadfarnia M, Sofronis P, & Robertson IM (2012) The role of hydrogen in hydrogen embrittlement fracture of lath martensitic steel. *Acta Materialia* 60(13):5182-5189.
122. Rogers H (1968) Hydrogen embrittlement of metals. *Science* 159(3819):1057-1064.

123. Myers SM, *et al.* (1992) Hydrogen interactions with defects in crystalline solids. *Reviews of Modern Physics* 64(2):559.
124. Robertson IM, *et al.* (2015) Hydrogen embrittlement understood. *Metallurgical and Materials Transactions B* 46(3):1085-1103.
125. Gerberich W, Marsh P, & Hoehn J (1996) Hydrogen induced cracking mechanisms—are there critical experiments? *Hydrogen Effects in Materials*:539-554.
126. Troiano AR (2016) The role of hydrogen and other interstitials in the mechanical behavior of metals. *Metallography, Microstructure, and Analysis* 5(6):557-569.
127. Birnbaum HK & Sofronis P (1994) Hydrogen-enhanced localized plasticity—a mechanism for hydrogen-related fracture. *Materials Science and Engineering: A* 176(1-2):191-202.
128. Lu G, Zhang Q, Kioussis N, & Kaxiras E (2001) Hydrogen-enhanced local plasticity in aluminum: an ab initio study. *Physical review letters* 87(9):095501.
129. Robertson I (2001) The effect of hydrogen on dislocation dynamics. *Engineering Fracture Mechanics* 68(6):671-692.
130. Beachem C (1972) A new model for hydrogen-assisted cracking (hydrogen "embrittlement"). *Metallurgical transactions* 3(2):441-455.
131. Toda H, *et al.* (2009) Growth behavior of hydrogen micropores in aluminum alloys during high-temperature exposure. *Acta Materialia* 57(7):2277-2290.
132. Li M, *et al.* (2017) Effect of hydrogen on the integrity of aluminium–oxide interface at elevated temperatures. *Nature Communications* 8:14564.
133. Xie D-G, *et al.* (2015) In situ study of the initiation of hydrogen bubbles at the aluminium metal/oxide interface. *Nature materials* 14(9):899-903.
134. Lu G & Kaxiras E (2005) Hydrogen embrittlement of aluminum: the crucial role of vacancies. *Physical review letters* 94(15):155501.
135. Nagumo M (2004) Hydrogen related failure of steels–a new aspect. *Materials Science and Technology* 20(8):940-950.
136. Takai K, Shoda H, Suzuki H, & Nagumo M (2008) Lattice defects dominating hydrogen-related failure of metals. *Acta Materialia* 56(18):5158-5167.
137. Bhatia M, Groh S, & Solanki K (2014) Atomic-scale investigation of point defects and hydrogen-solute atmospheres on the edge dislocation mobility in alpha iron. *Journal of Applied Physics* 116(6):064302.
138. Cottrell A & Jaswon M (1949) Distribution of solute atoms round a slow dislocation. *Proceedings of the Royal Society of London A: Mathematical, Physical and Engineering Sciences*, (The Royal Society), pp 104-114.
139. Sills R & Cai W (2016) Solute drag on perfect and extended dislocations. *Philosophical Magazine* 96(10):895-921.
140. Song J & Curtin W (2014) Mechanisms of hydrogen-enhanced localized plasticity: an atomistic study using α-Fe as a model system. *Acta Materialia* 68:61-69.
141. Xie D, *et al.* (2016) Hydrogenated vacancies lock dislocations in aluminium. *Nature Communications* 7.

142. Chen LY, He M-r, Shin J, Richter G, & Gianola DS (2015) Measuring surface dislocation nucleation in defect-scarce nanostructures. *Nat Mater* 14(7):707-713.
143. Deng C & Sansoz F (2009) Near-ideal strength in gold nanowires achieved through microstructural design. *Acs Nano* 3(10):3001-3008.
144. Greer JR & Nix WD (2006) Nanoscale gold pillars strengthened through dislocation starvation. *Physical Review B* 73(24):245410.
145. Jennings AT, Li J, & Greer JR (2011) Emergence of strain-rate sensitivity in Cu nanopillars: Transition from dislocation multiplication to dislocation nucleation. *Acta Materialia* 59(14):5627-5637.
146. Li J, Van Vliet KJ, Zhu T, Yip S, & Suresh S (2002) Atomistic mechanisms governing elastic limit and incipient plasticity in crystals. *Nature* 418(6895):307-310.
147. Barnoush A & Vehoff H (2010) Recent developments in the study of hydrogen embrittlement: Hydrogen effect on dislocation nucleation. *Acta Materialia* 58(16):5274-5285.
148. Wen M & Li Z (2012) Thermally activated process of homogeneous dislocation nucleation and hydrogen effects: An atomistic study. *Computational Materials Science* 54:28-31.
149. Zhou X, Ouyang B, Curtin W, & Song J (2016) Atomistic investigation of the influence of hydrogen on dislocation nucleation during nanoindentation in Ni and Pd. *Acta Materialia* 116:364-369.
150. Salehinia I, Lawrence S, & Bahr D (2013) The effect of crystal orientation on the stochastic behavior of dislocation nucleation and multiplication during nanoindentation. *Acta Materialia* 61(5):1421-1431.
151. Wagih M, Tang Y, Hatem T, & El-Awady JA (2015) Discerning enhanced dislocation plasticity in hydrogen-charged α-iron nano-crystals. *Materials Research Letters* 3(4):184-189.
152. Leyson G, Grabowski B, & Neugebauer J (2016) Multiscale modeling of hydrogen enhanced homogeneous dislocation nucleation. *Acta Materialia* 107:144-151.
153. Song J & Curtin W (2011) A nanoscale mechanism of hydrogen embrittlement in metals. *Acta Materialia* 59(4):1557-1569.
154. Song J & Curtin W (2013) Atomic mechanism and prediction of hydrogen embrittlement in iron. *Nat Mater* 12(2):145-151.
155. Amin-Ahmadi B*, et al.* (2016) Dislocation/hydrogen interaction mechanisms in hydrided nanocrystalline palladium films. *Acta Materialia* 111:253-261.
156. Carpena-Núñez J, Yang D, Kim J-W, Park C, & Fonseca LF (2012) Mechanical characterization of pristine and hydrogen-exposed palladium nanowires by in situ TEM. *Nanotechnology* 24(3):035701.
157. Kheradmand N, Dake J, Barnoush A, & Vehoff H (2012) Novel methods for micromechanical examination of hydrogen and grain boundary effects on dislocations. *Philosophical Magazine* 92(25-27):3216-3230.
158. Filleter T*, et al.* (2012) Nucleation-controlled distributed plasticity in penta-twinned silver nanowires. *Small* 8(19):2986-2993.

159. Brochard S, Hirel P, Pizzagalli L, & Godet J (2010) Elastic limit for surface step dislocation nucleation in face-centered cubic metals: temperature and step height dependence. *Acta Materialia* 58(12):4182-4190.
160. Li J (2015) Dislocation nucleation: Diffusive origins. *Nat Mater* 14(7):656-657.
161. Salah SBH, Gerard C, & Pizzagalli L (2017) Influence of surface atomic structure on the mechanical response of aluminum nanospheres under compression. *Computational Materials Science* 129:273-278.
162. Lee S*, et al.* (2016) FIB-induced dislocations in Al submicron pillars: Annihilation by thermal annealing and effects on deformation behavior. *Acta Materialia* 110:283-294.
163. Pukšič N, Jenko M, Godec M, & McGuiness PJ (2017) A comparison of the uniaxial deformation of copper and nickel (1 1 19) surfaces: a molecular dynamics study. *Sci Rep-Uk* 7.
164. Henkelman G, Uberuaga BP, & Jónsson H (2000) A climbing image nudged elastic band method for finding saddle points and minimum energy paths. *The Journal of chemical physics* 113(22):9901-9904.
165. Wei Y*, et al.* (2014) Evading the strength–ductility trade-off dilemma in steel through gradient hierarchical nanotwins. *Nature communications* 5.
166. Lu K (2014) Making strong nanomaterials ductile with gradients. *Science* 345(6203):1455-1456.
167. Chen LY, He M-r, Shin J, Richter G, & Gianola DS (2015) Measuring surface dislocation nucleation in defect-scarce nanostructures. *Nat Mater*.